UPSCALING METHODS FOR MULTI-PHASE FLOW AND TRANSPORT IN HETEROGENEOUS POROUS MEDIA

A Dissertation

by

YAN LI

Submitted to the Office of Graduate Studies of
Texas A&M University
in partial fulfillment of the requirements for the degree of

DOCTOR OF PHILOSOPHY

December 2009

Major Subject: Mathematics

UPSCALING METHODS FOR MULTI-PHASE FLOW AND TRANSPORT IN HETEROGENEOUS POROUS MEDIA

A Dissertation

by

YAN LI

Submitted to the Office of Graduate Studies of
Texas A&M University
in partial fulfillment of the requirements for the degree of

DOCTOR OF PHILOSOPHY

Approved by:

Chair of Committee,	Yalchin Efendiev
Committee Members,	Akhil Datta-Gupta
	Jay Walton
	Hongbin Zhan
Head of Department,	Al Boggess

December 2009

Major Subject: Mathematics

ABSTRACT

Upscaling Methods for Multi-Phase Flow and Transport
in Heterogeneous Porous Media. (December 2009)
Yan Li, B.S., Shandong University, China;
M.S., Shandong University, China
Chair of Advisory Committee: Dr. Yalchin Efendiev

In this dissertation we discuss some upscaling methods for flow and transport in heterogeneous reservoirs. We studied realization-based multi-phase flow and transport upscaling and ensemble-level flow upscaling. Multi-phase upscaling is more accurate than single-phase upscaling and is often required for high level of coarsening. In multi-phase upscaling, the upscaled transport parameters are time-dependent functions and are challenging to compute. Due to the hyperbolic feature of the saturation equation, the nonlocal effects evolve in both space and time. Standard local two-phase upscaling gives significantly biased results with reference to fine-scale solutions. In this work, we proposed two types of multi-phase upscaling methods, TOF (time-of-flight)-based two-phase upscaling and local-global two-phase upscaling. These two methods incorporate global flow information into local two-phase upscaling calculations. A linear function of time and time-of-flight and a global coarse-scale two-phase solution (time-dependent) are used respectively in these two approaches. The local boundary condition therefore captures the global flow effects both spatially and temporally. These two methods are applied to permeability distributions with various correlation lengths. Numerical results show that they consistently improve existing two-phase upscaling methods and provide accurate coarse-scale solutions for both flow and transport.

We also studied ensemble level flow upscaling. Ensemble level upscaling is up-

scaling for multiple geological realizations and often required for uncertainty quantification. Solving the flow problem for all the realizations is time-consuming. In recent years, some stochastic procedures are combined with upscaling methods to efficiently compute the upscaled coefficients for a large set of realization. We proposed a fast perturbation approach in the ensemble level upscaling. By Karhunen-Loève expansion (KLE), we proposed a correction scheme to fast compute the upscaled permeability for each realization. Then the sparse grid collocation and adaptive clustering are coupled with the correction scheme. When we solve the local problem, the solution can be represented by a product of Green's function and source term. Using collocation and clusering technique, one can avoid the computation of Green's function for all the realizations. We compute Green's function at the interpolation nodes, then for any realization, the Green's function can be obtained by interpolation. The above techniques allow us to compute the upscaled permeability rapidly for all realizations in stochastic space.

To Tao, Mom and Dad

ACKNOWLEDGMENTS

First and foremost, I wish to express my sincere thanks to my advisor, Dr. Yalchin Efendiev for all his guidance and consistent support throughout my graduate career. His many insights and ideas have been invaluable in my preparation to begin my career as a mathematician. I wish to thank Dr. Akhil Datta-Gupta, Dr. Jay Walton and Dr. Hongbin Zhan for serving on my committee and providing many insightful comments and questions.

I would like to thank Dr. Yuguang Chen, for her helpful discussions and insightful suggestions on local-global two-phase upscaling. Thanks for her thoughtful guidance and helps during my internship at Chevron and consistent encouragement since then. I would like to thank Dr. Xiao-Hui Wu, Dr. Yahan Yang, and Dr. Sartaj Ghai for their help, guidance, and discussions during my internship at ExxonMobil.

I also would like to thank Dr. Ciprian Foias for his insightful suggestions and guidance on the dynamic analysis of flow and transport problem. I wish to thank Dr. Louis Durlofsky for his suggestions on ensemble-level upscaling. I am very grateful to Dr. Eric Chung for his kind help and valuable discussions in developing discontinuous Galerkin methods for the transport equation. I am also grateful to Dr. Paul Dostert for helping me with collocation techniques and ensemble-level upscaling. I also would like to thank Dr. Lijian Jiang for the valuable discussions and his help in homogenization analysis of time-dependent problems.

I also wish to express my gratitude to the professors and staff of the Department of Mathematics at Texas A&M. In addition, I wish to thank the entire numerical analysis group for helping me prepare to begin my research and write my dissertation. I express my thanks to Dr. Paulo Lima-Philho, for his help and guidance on how to teach mathematics. I want to thank Ms. Monique Stewart for her incredible patience

and knowledge with the university administration. I also thank the students in the mathematics department, specifically Dukjin Nam, Seungil Kim, Linh Nguyen, Lidia Smith, Yulia Hristova, Jia Wei and Mei Yang. Their great help both inside and outside my academic life and their friendship are very much appreciated.

Lastly, but most importantly, I would like to thank my husband, Tao and my family for for their unconditional support and love throughout my graduate career.

TABLE OF CONTENTS

Page

ABSTRACT iii

DEDICATION v

ACKNOWLEDGMENTS vi

TABLE OF CONTENTS viii

LIST OF TABLES xi

LIST OF FIGURES xiii

CHAPTER

I INTRODUCTION 1

II UPSCALING IN HETEROGENEOUS POROUS MEDIA 7

2.1. Governing Equations 8
2.1.1. Fine-scale equations 8
2.1.2. Coarse-scale models 9
2.2. Upscaling for Flow and Transport 11
2.2.1. Single-phase upscaling 11
2.2.2. Pseudo-relative permeabilities for multiphase upscaling 13

III TWO-PHASE UPSCALING FOR FLOW AND TRANSPORT . 16

3.1. Global Flow Dependence of Transport Functions 16
3.1.1. Local v.s. global two-phase upscaling 16
3.1.2. Performance of existing two-phase upscaling techniques 19
3.2. TOF-Based Two-Phase Upscaling 22
3.2.1. Asymptotic analysis 23
3.2.2. Accurate saturation boundary condition 26

CHAPTER Page

3.2.3. Algorithm 30
3.2.4. Numerical result 31
3.2.4.1. Results for different correlation lengths . . . 32
3.2.4.2. Results for high mobility ratio 36
3.2.4.3. Results for low mobility ratio 39
3.2.4.4. Results with different pressure boundary conditions 40
3.2.5. Multiscale discontinuous galerkin method for saturation equation 43
3.2.6. Concluding remarks 46
3.3. Local-Global Two-Phase Upscaling 48
3.3.1. Interpolation of coarse-scale solutions 49
3.3.2. Update of local boundary conditions 51
3.3.3. Algorithm of local-global two-phase upscaling . . . 54
3.3.4. Numerical result 55
3.3.4.1. Results for different correlation lengths . . . 56
3.3.4.2. Results for high mobility ratio 57
3.3.4.3. Results for low mobility ratio 62
3.3.4.4. Results for changing flow conditions 62
3.3.4.5. Results for multiple realizations 64
3.3.5. Concluding remarks 67
3.4. Conclusion 69

IV UPSCALING METHOD FOR TIME DEPENDENT PARABOLIC EQUATIONS 73

4.1. Time-Space Upscaling Procedure 74

V ENSEMBLE LEVEL FLOW UPSCALING 79

5.1. Stochastic Subsurface Properties 79
5.2. A Perturbation Approach 84
5.2.1. Truncated permeability 84
5.2.2. Correction scheme 86
5.2.3. Error analysis 88
5.3. Fast Computation of $\tilde{k}^*$ on Hyperplane 91
5.3.1. Green's function 92
5.3.2. Fast computation via hyperplane projection . . . 92
5.4. Collocation Technique in Stochastic Space 95
5.4.1. Collocation technique in lower dimensional space . 96

CHAPTER Page

5.4.1.1. General interpolation in $\mathbb{V}$ 97
5.4.1.2. Sparse grid interpolation in $\mathbb{V}$ 99
5.4.2. Sparse grid interpolation in $\mathbb{R}^N$ 100
5.5. Adaptive Clustering 102
5.5.1. Region partition in lower dimensional space 102
5.5.2. Adaptive clustering with error indicator 105
5.5.3. Numerical results in lower dimensional space . . . 108
5.6. Concluding Remarks 109

VI SUMMARY 111

REFERENCES 113

APPENDIX A 118

VITA 120

LIST OF TABLES

TABLE Page

5.1 Error of $\frac{\|k^*-k_0^*\|}{\|k^*\|}$ base on 100 realizations of log-exponential permeability fields, with correlation lengths $l_x = 0.1$, $l_y = 0.1$ and variance $\sigma = 2.0$. 85

5.2 On a hyperplane, we compare the errors of $\frac{\|k^*-k_0^*\|}{\|k^*\|}$ and $\frac{\|k^*-\tilde{k}^*\|}{\|k^*\|}$ for an exponential permeability field, with the correlation lengths $l_x = 0.3$, $l_y = 0.06$ and the variance $\sigma = 2.0$. 94

5.3 On one hyperplane, we compare the error of $\frac{\|k^*-k_0^*\|}{\|k^*\|}$ and $\frac{\|k^*-\tilde{k}^*\|}{\|k^*\|}$ for an exponential permeability field, with correlation lengths $l_x = 0.4$, $l_y = 0.05$ and the variance $\sigma = 2.0$. 94

5.4 Error of $\frac{\|k_0^*-k^*\|}{\|k^*\|}$ (truncated upscaled permeability), $\frac{\|\tilde{k}^*-k^*\|}{\|k^*\|}(PE)$ (corrected upscaled permeability) and $\frac{\|\mathcal{I}^m(\tilde{k}^*)-k^*\|}{\|k^*\|}$ (interpolated corrected upscaled permeability using linear interpolation) for a log-normal permeability field with correlation lengths $l_x = 0.3$, $l_y = 0.5$ and covariance $\sigma = 2.0$. 99

5.5 Error of $\frac{\|k_0^*-k^*\|}{\|k^*\|}$ (truncated upscaled permeability), $\frac{\|\tilde{k}^*-k^*\|}{\|k^*\|}(PE)$ (corrected upscaled permeability) and $\frac{\|\mathcal{I}^m(\tilde{k}^*)-k^*\|}{\|k^*\|}$ (interpolated corrected upscaled permeability using Smolyak Algorithm in $\mathbb{V}$) for a log-normal permeability field with correlation lengths $l_x = 0.3$, $l_y = 0.5$ and the variance $\sigma = 2.0$. 100

5.6 Error of $\frac{\|\tilde{k}^*-k^*\|}{\|k^*\|}(PE)$ (corrected upscaled permeability), $\frac{\|I^m(\tilde{k}^*)-k^*\|}{\|k^*\|}$ (interpolated corrected upscaled permeability using Smolyak Algorithm in $\mathbb{V}$), and $\frac{\|I^N(\tilde{k}^*)-k^*\|}{\|k^*\|}$ (interpolated corrected upscaled permeability using Smolyak Algorithm in $\mathbb{R}^N$) for a log-normal permeability field with $l_x = 0.1$, $l_y = 0.1$ and $\sigma = 2.0$. 102

TABLE Page

5.7 Error of $\frac{\|I^m(\tilde{k}^*)-k^*\|}{\|k^*\|}$ (interpolated corrected upscaled permeability using Smolyak Algorithm in $\mathbb{V}$), and $\frac{\|I^N(\tilde{k}^*)-k^*\|}{\|k^*\|}$ (interpolated corrected upscaled permeability using Smolyak Algorithm in $\mathbb{R}^N$) for a log-exponential permeability field with $l_x = 0.3$, $l_y = 0.5$ and $\sigma = 2.0$. 103

LIST OF FIGURES

FIGURE		Page
2.1	Upscaling work flow.	7
2.2	Schematic showing a local single-phase upscaling. Local problem (2.16) and (2.17) is solved to compute k_x^*, the unit vector used is $e = e^1 = (1, 0)$.	12
2.3	Schematic showing a local multiphase upscaling of transport parameters λ^* and f^*, a constant pressure-no flow boundary condition is applied.	13
3.1	A periodic permeability field generated by a template.	17
3.2	Upscaled total mobility function λ_x^* from local two-phase upscaling with standard local boundary conditions for one row of the coarse-scale blocks from the periodic permeability field.	18
3.3	Upscaled total mobility function λ_x^* from global two-phase upscaling with standard local boundary conditions for one row of the coarse-scale blocks from the periodic permeability field.	19
3.4	Permeability distributions of dimensions 100×100 with different correlation lengths, shown in log scale. For all the permeability fields, the variance (σ^2) of $\log k$ is 4.0.	20
3.5	Flow results of EFBC local two-phase upscaling and global two-phase upscaling for a log normal permeability field ($l_x = 0.4$, $l_y = 0.01$, and $\sigma = 2.0$).	21
3.6	Schematic showing TOF-based two-phase upscaling. The local boundary conditions of local fine-scale flow are determined from global fine-scale time-of-flight.	26

FIGURE Page

3.7 The saturation on two different coarse blocks. It shows that the overestimation of saturation in local region. The red line is standard two-phase upscaling with $S_{\text{inlet}} = 1$, the blue solid and dot-dash lines are the real saturation from global two-phase flow, both the distribution and mean changes with time. 27

3.8 The distribution of c from upstream to downstream in the periodic permeability field. The x-axis denotes the number of blocks indexing from upstream to downstream as 1 to 10. 28

3.9 The real saturation and simulated saturation on the local domain inlet edge. 29

3.10 Flow results of TOF-based two-phase upscaling (with EFBCs) for a log normal permeability field ($l_x = 0.4$, $l_y = 0.01$, and $\sigma = 2.0$), with $a_1 = 0.1$. 34

3.11 Flow results of TOF-based two-phase upscaling (with EFBCs) for a log normal permeability field ($l_x = 0.2$, $l_y = 0.02$, and $\sigma = 2.0$), with $a_1 = 0.1$. 34

3.12 Flow results of TOF-based two-phase upscaling (with EFBCs) for a log normal permeability field ($l_x = 0.25$, $l_y = 0.01$, and $\sigma = 2.0$), with $a_1 = 0.1$. 35

3.13 Flow results of TOF-based two-phase upscaling (with EFBCs) for a log normal permeability field ($l_x = 0.5$, $l_y = 0.1$, and $\sigma = 2.0$), with $a_1 = 0.5$. 35

3.14 Flow results of TOF-based two-phase upscaling (with EFBCs) for a log normal permeability field ($l_x = 0.2$, $l_y = 0.02$, and $\sigma = 2.0$), $M = 50$ and $a_1 = 0.1$. 37

3.15 Flow results of TOF-based two-phase upscaling (with EFBCs) for a log normal permeability field ($l_x = 0.25$, $l_y = 0.01$, and $\sigma = 2.0$), $M = 50$ and $a_1 = 0.1$. 38

3.16 Flow results of TOF-based two-phase upscaling (with EFBCs) for a log normal permeability field ($l_x = 0.4$, $l_y = 0.01$, and $\sigma = 2.0$), $M = 100$ and $a_1 = 0.1$. 38

FIGURE Page

3.17 Flow results of TOF-based two-phase upscaling (with EFBCs) for a log normal permeability field ($l_x = 0.4$, $l_y = 0.01$, and $\sigma = 2.0$), $M = 0.1$ and $a_1 = 0.1$. 39

3.18 Flow results of TOF-based two-phase upscaling (with Standard) for a log normal permeability field ($l_x = 0.4$, $l_y = 0.01$, and $\sigma = 2.0$), with $a_1 = 0.1$. 41

3.19 Flow results of TOF-based two-phase upscaling (with Global) for a log normal permeability field ($l_x = 0.4$, $l_y = 0.01$, and $\sigma = 2.0$), with $a_1 = 0.1$. 41

3.20 Flow results of TOF-based two-phase upscaling (with Standard) for a log normal permeability field ($l_x = 0.5$, $l_y = 0.1$, and $\sigma = 2.0$), with $a_1 = 0.5$. 42

3.21 Flow results of TOF-based two-phase upscaling (with Global) for a log normal permeability field ($l_x = 0.5$, $l_y = 0.1$, and $\sigma = 2.0$), with $a_1 = 0.5$. 42

3.22 A layered permeability field. 47

3.23 The saturation distribution: the left figure shows the fine-scale saturation; the right figure shows the coarse-scale saturation. 47

3.24 Schematic showing local-global two-phase upscaling. The local boundary conditions of local fine-scale flow are determined from global coarse-scale solutions. Both the global coarse solutions and local boundary conditions are time-dependent. 49

3.25 Schematic showing the update of local boundary conditions. 52

3.26 Flow results of local-global two-phase upscaling for a log normal permeability field ($l_x = 0.4$, $l_y = 0.01$, and $\sigma = 2.0$). 58

3.27 Flow results of local-global two-phase upscaling for a log normal permeability field ($l_x = 0.5$, $l_y = 0.1$, and $\sigma = 2.0$). 58

3.28 Flow results of local-global two-phase upscaling for a log normal permeability field ($l_x = 0.2$, $l_y = 0.02$, and $\sigma = 2.0$). 59

FIGURE Page

3.29 Flow results of local-global two-phase upscaling for a log normal permeability field ($l_x = 0.25$, $l_y = 0.01$, and $\sigma = 2.0$). 59

3.30 Flow results of local-global two-phase upscaling for a log normal permeability field ($l_x = 0.25$, $l_y = 0.01$, and $\sigma = 2.0$), and $M = 50$. . . 61

3.31 Flow results of local-global two-phase upscaling for a log normal permeability field ($l_x = 0.4$, $l_y = 0.01$, and $\sigma = 2.0$), and $M = 100$. . . 61

3.32 Flow results of local-global two-phase upscaling for a log normal permeability field ($l_x = 0.4$, $l_y = 0.01$, and $\sigma = 2.0$), $M = 0.1$. 63

3.33 Schematically showing different flow conditions. Flow condition is constant pressure and no flow condition from PVI=0.0 to PVI = 0.6. For PVI$\geq$ 0.6, flow condition is changed to corner-to-corner flow. 64

3.34 Flow results of local-global two-phase upscaling with a changed flow condition at PVI=0.6, as (a) in Fig. 3.33. Permeability is a log normal permeability field $l_x = 0.4$, $l_y = 0.01$, and $\sigma = 2.0$, and $M = 5$. 65

3.35 Flow results of local-global two-phase upscaling with a changed flow condition at PVI=0.6, as (b) in Fig. 3.33. Permeability is a log normal permeability field $l_x = 0.4$, $l_y = 0.01$, and $\sigma = 2.0$, and $M = 5$. 65

3.36 Oil fractional flow for 100 realizations for a log normal permeability field ($l_x = 0.4$, $l_y = 0.01$, and $\sigma = 2.0$) and $M = 5$. Black curves represent P50 (solid curve) and P10-P90 interval (dashed curve). 71

3.37 Comparison of P50 (thick curves) and P10-P90 interval (thin curves) for oil cut between fine-scale (solid curves) and coarse-scale (dot-dash curves) models a log normal permeability field ($l_x = 0.4$, $l_y = 0.01$, and $\sigma = 2.0$) and $M = 5$. 72

5.1 An illustration of eigenvalues Distribution. 82

5.2 Schematic showing the eigenvectors of a log-normal permeability field, with $l_x = 0.1$, $l_y = 0.1$, and $\sigma = 2.0$. 83

5.3 An illustration of amplitudes distribution. 83

FIGURE Page

5.4 Errors of $\frac{\|k^*-k_0^*\|}{\|k^*\|}$ and $\frac{\|k^*-\tilde{k}^*\|}{\|k^*\|}$ based on 100 realizations of log-normal permeability fields, with correlation lengths $l_x = 0.1$, $l_y = 0.1$ and the variance $\sigma = 2.0$. 87

5.5 Errors of $\frac{\|k^*-k_0^*\|}{\|k^*\|}$ and $\frac{\|k^*-\tilde{k}^*\|}{\|k^*\|}$ based on 100 realizations of log-exponential permeability fields, with the correlation lengths $l_x = 0.1$, $l_y = 0.1$ and the variance $\sigma = 2.0$. 88

5.6 Illustration of a hyperplane $\mathbf{H}_{\theta^0}$ in $\mathbb{R}^N$. 93

5.7 An illustration of the projection from $\mathbb{R}^N$ onto $\mathbb{V}$. 97

5.8 Error of corrected upscaled permeability using linear interpolation for a normal permeability field with the correlation lengths $l_x = 0.3$, $l_y = 0.5$ and the variance $\sigma = 2.0$. 98

5.9 Illustration of the first level Smolyak nodes in $\mathbb{R}^N$. 101

5.10 Schematic showing the clustering for random realizations, the center of each cluster is the representative point. 104

5.11 Schematic illustration of the distribution of error $\frac{\|k^*-\tilde{k}^*\|}{\|k^*\|}$ on $\Omega = [-20, 20]^2$ and 16 clusters grouped by this error. 104

5.12 Schematic showing the clusters and the representative points θ_0. In each cluster, the center point is chosen as the representative point. 105

5.13 Distribution of logarithm of the true error, $Log(Er)$ and logarithm of the error indicator, $Log(EE)$ for a log-exponential permeability field with $l_x = 0.1$, $l_y = 0.1$, $\sigma = 2.0$. 106

5.14 Cross plot of natural logarithm of the true error, $Log(Er)$ and natural logarithm of the error indicator, $Log(EE)$ for a log-exponential permeability field with $l_x = 0.1$, $l_y = 0.1$, $\sigma = 2.0$. 107

5.15 400 realizations and 20 representative points for a log-exponential permeability field with $l_x = 0.1$, $l_y = 0.1$, $\sigma = 2.0$. 108

5.16 Errors of $\frac{\tilde{k}^*-k^*}{k^*}$ based on 100 realizations for a log-exponential permeability field with $l_x = 0.1$, $l_y = 0.1$, $\sigma = 2.0$. 109

CHAPTER I

INTRODUCTION

Subsurface formations are characterized by strong heterogeneities occurring on multiple length scales. High-resolution formation descriptions are often generated through geostatistical simulation by integrating data from different sources and at various scales. Due to the very high resolution involved, direct numerical simulation of subsurface flow is usually not feasible. Therefore upscaling procedures are often applied to coarsen the highly detailed models to scales that are suitable for flow simulation. Flow and transport are the two main mechanisms in subsurface flow. In this dissertation, we will discuss some upscaling methods for flow and transport problem in porous media.

The main idea of upscaling is to generate coarse-scale equations, which may not be same as fine-scale equations. The coarse-scale parameters are computed by solving local fine-scale problems. Based on upscaled parameters, upscaling in porous media can be classified as upscaling of single-phase flow parameters and upscaling of multiphase transport parameters. The single-phase flow upscaling considers only the upscaling of absolute permeability k, and represents the most commonly applied upscaling technique in practice (see reviews, e.g., [32, 18, 19], for a variety of methods). The upscaling of multiphase transport parameters involves, in addition, rock-fluid properties, such as phase relative permeabilities k_{raj}. These upscaled parameters are time-dependent functions (through phase saturations), and are more challenging to compute. This type of upscaling is intended to capture the transport of injected fluid

---

This dissertation follows the style of the Multiscale Modeling and Simulation.

and its mobility effects on flow, and is especially required in a high level of coarsening. Reviews and recent studies (e.g., [1, 9, 5]) presented different methods and discussed general challenges in multiphase upscaling.

With any upscaling method, a well-known issue lies in that its accuracy can be significantly affected by local boundary conditions imposed to compute the upscaled quantities. In recent years, significant progress has been made for the upscaling of single-phase flow parameters. Based on the flow problems solved in the upscaling calculations, there exist a series of methods, ranging from local, quasi-global, to global approaches. In the upscaling of two-phase transport functions, the issue of local boundary conditions becomes more severe because of the need of boundary conditions for both pressure and saturation equations. Due to the hyperbolic feature of the saturation equation, the nonlocal effects evolve in space and time. Standard local two-phase upscaling gives significantly biased results with reference to fine-scale solutions. Although there exist global two-phase upscaling methods, it is important to note that unlike global single-phase upscaling, global two-phase upscaling may not be feasible in practice.

We developed two type of two-phase upscaling approaches using global flow information in local boundary conditions. One is TOF-based two-phase upscaling, where we use a linear function of time t and time-of-flight τ accounting for temporal and spatial trend in saturation. The other approach is local-global two-phase upscaling. The global coarse-scale two-phase solution is directly imposed onto local boundary condition for both pressure and saturation. Since global coarse-scale solution and local fine-scale simulation has different time scale, we use the average of local saturation as a criteria to update boundary conditions. This approach entails the exchange of global coarse and local fine-scale flow information in space and time. Both TOF-based and local-global two-phase upscaling significantly improve over existing method and

provide accurate predictions in close agreement with the fine-scale reference solution.

In this dissertation, we also study ensemble level upscaling. As we know, the media properties often contain uncertainties. These uncertainties are usually parameterized and one has to deal with a large set of permeability fields (realizations). The upscaling for multiple realizations is the ensemble level upscaling. The ensemble level upscaling approach aims to achieve agreement between the fine and coarse-scale flow models at the ensemble level, rather than realization by realization agreement. For this purpose, flow-based upscaling calculations are combined with some statistical procedure to efficiently compute the upscaled parameters. An ensemble level upscaling, proposed by Y. Chen and L. Durlofsky, computes upscaled coefficients via some sampled realizations [7]. A collocation method uses the upscaled coefficients on a sparse grid to interpolate the upscaled coefficients for a given realization [13].

Based on Karhunen-Loève expansion (KLE), we proposed a correction scheme to compute the upscaled absolute permeabilities. In a high dimensional stochastic space $\mathbb{R}^N$, we solve the local problem in a lower dimensional space $\mathbb{R}^m$ of $\mathbb{R}^N$, where $m \leq N$. Then using Green's function and collocation technique, we are able to compute the upscaled permeabilities for a random realization in $\mathbb{R}^N$. Especially, the Smolyak sparse grid nodes are used in collocation. Due to the special distribution of $1st$ level Smolyak nodes, we only solve $2m + 1$ of $2N + 1$ local problems. The other $2N - 2m$ nodes are on a hyper-plane, where we can use the correction scheme to rapidly compute upscaled permeabilites. We also proposed an adaptive clustering technique. A large set of random variables can be divided into a group of clusters and in each cluster we only need solve local problem for a representative realization. Thus, the number of variables are greatly reduced.

The dissertation proceeds as follows. A literature review on the upscaling of flow and transport is presented in Chapter II. It includes single-phase upscaling, multi-

phase upscaling and local boundary issue in upscaling method. We use the global fine-scale solution at initial time in the local upscalign computations. The incorporation of global information in local problem improves the accuracy of upscaled parameters.

Chapter III presents TOF-based and local-global two-phase upscaling methods. The global flow dependency of transport functions is first discussed using a simple periodic permeability. Then, we present TOF-based two-phase upscaling, which uses single-phase time-of-flight τ to incorporate the large-scale heterogeneties in local boundary condition. A piecewise linear approximation, $At + B\tau + C$, is used as saturation boundary condition in local fine-scale simulation. Here, τ is a global fine-scale time-of-flight, t is the time in the local flow simulation. A represents a temporal change of local boundary condition, B and C represent global spatial trend and local variation. Due to the unknown time-dependency of global solution, A needs to be pre-determined. To get temporal information, we proposed to use the global coarse-scale two-phase solution in local boundary condition. This is the local-global two-phase upscaling. In this approach, the global coarse-scale solutions (both flux and saturation) are interpolated on the local fine-scale boundaries. These flux and saturation boundary conditions are time-dependent and they are updated when the local saturation equals to coarse-scale saturation. This approach provides a mean to systematically incorporate global flow effects for both pressure and saturation in local two-phase upscaling calculations. We also generalize the proposed approaches and suggest the use of discontinuous Galerkin method where the basis functions depend on time-of-flight functions. Some preliminary numerical results are presented.

In Chapter IV, we give a homogenization analysis for a time-dependent parabolic problem. A simplified analysis is presented for single-phase upscaling where the permeability is a time-dependent function that has both spatial and temporal variations. In particular, we choose time scales such that the local flow problem in homogeniza-

tion is time-dependent, i.e., time scales are important in upscaling. Our aim is to mimic a scenario when the mobility changes in time for pressure equation or velocity changes in time for the saturation is important. We derive error estimates for homogenized coefficients. This error represent the difference between true upscaled permeability for time-dependent flow problem and the approximate upscaled permeability computed based on local flow solutions. The local flow problems are formulated both in space and time. Our analysis reveals the resonance errors and shows that there is a resonance error both with respect to space and time discretization.

Chapter V is devoted to ensemble level flow upscaling. In this chapter, we propose a fast correction scheme for single-phase upscaling. In the correction scheme, the solution of local flow problem is represented by a product of Green's function and a perturbation term, which allows us to get the local solution rapidly on hyperplanes. The perturbation term can be rapidly computed, but one has to solve a local problem to get Green's function. To avoid solving local flow problem for all realizations, we use collocation and adaptive clustering techniques. The basic idea of the collocation method is to choose a sparse grid nodes (e.g. Smolyak Nodes [28, 2]) and compute Green's function on these grid nodes. Then for a random realization, the Green's function is calculated by interpolation of Green's function at grid nodes. The idea of adaptive clustering is to group all the realizations into a number of clusters, then solve local flow problem on a reduced set. In each cluster, we choose only one representative realization and compute Green's function at this point. For other realizations in this cluster, we use Green's function at the representative point and the correction scheme to get the approximated upscaled permeabilities. The collocation and clustering techniques coupled with correction scheme allow us to compute upscaled flow parameters fast in the stochastic space.

At last, we summarize our work in Chapter VI and discuss the possible future

work.

CHAPTER II

UPSCALING IN HETEROGENEOUS POROUS MEDIA

In this chapter, we introduce the notations and governing equations in the upscaling of flow and transport problem. The purpose of upscaling is to develop appropriate coarse-scale models with coarse-scale coefficients determined via upscaling procedures. By the upscaled coarse-scale parameters, upscaling can be classified as upscaling of single-phase flow parameters and upscaling of multiphase transport parameters. We will discuss these two types of upscaling respectively.

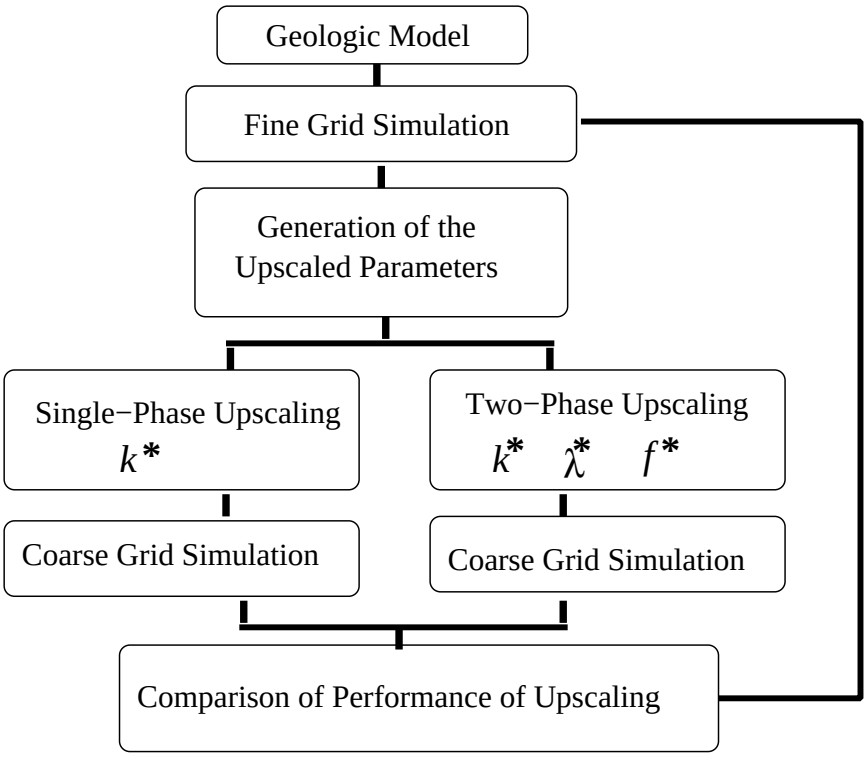

Fig. 2.1. Upscaling work flow.

2.1. Governing Equations

2.1.1. Fine-scale equations

We consider two-phase flow and transport equations on the fine scale, neglecting the effects of gravity, compressibility, capillary pressure and dispersion. Porosity ϕ, defined as the volume fraction of the void space, will be taken to be constant. The two phases will be referred to as water and oil and designated by the subscripts w and o, respectively. We can then write Darcy's law, with all quantities dimensionless, for each phase j $(j = w, o)$ as follows:

$$v_j = -\lambda_j(S)k(x) \cdot \nabla p, \tag{2.1}$$

where v_j is phase velocity, k is the absolute permeability tensor, which is symmetric and uniformly positive definite. S is water saturation (volume fraction), p is pressure, λ_j is phase mobility,

$$\lambda_j = k_{rj}(S)/\mu_j \tag{2.2}$$

where k_{rj} and μ_j are the relative permeability and viscosity of phase j respectively. For simplicity, we will study two-dimensional case.

Combining Darcy's law with conservation of mass, $div(v_w + v_o)$=0, allows us to write the flow equation in the following form

$$div(\lambda(S)k(x) \cdot \nabla p) = q_t, \tag{2.3}$$

where the total mobility $\lambda(S)$ is given by

$$\lambda(S) = \lambda_w(S) + \lambda_o(S), \tag{2.4}$$

and q_t is a source term representing wells/sources. The term $q_t = q_w + q_o$ represents

the total volumetric source term. The saturation dynamics affects the flow equations. One can derive the equation describing the dynamics of the saturation

$$\phi\frac{\partial S}{\partial t} + div(vf(S)) = -q_w, \tag{2.5}$$

where $f(S)$ is the fractional flow of water, given by

$$f = \lambda_w/(\lambda_w + \lambda_o). \tag{2.6}$$

The signs of the source terms which appear in (2.3) and (2.5) can be inter-changed. The total velocity v is given by

$$v = v_w + v_o = -\lambda(S)k(x)\cdot\nabla p. \tag{2.7}$$

(2.3) and (2.5) are the system of flow and transport equations in reservoir and they are also referred as pressure and saturation equations.

2.1.2. Coarse-scale models

The above equations (2.3) and (2.5) describe the two-phase flow model on a fully resolved or fine scale. Exact coarse-scale equations can be obtained through volume averaging of the fine-scale equations, which gives

$$div\overline{[\lambda(S)k\cdot\nabla p]} = 0, \tag{2.8}$$

$$\overline{\phi}\frac{\partial\overline{S}}{\partial t} + div\overline{[vf(S)]} = 0, \tag{2.9}$$

where the overline represents volume averaging. Eqs. (2.8) and (2.9) are obtained by applying $\overline{div(\quad)} = div\overline{(\quad)}$, which is satisfied when the average is over orthogonal (e.g., rectangular) grid blocks, and by assuming the porosity ϕ is a constant. The averaging of nonlinear terms in the above equations yields additional terms (higher order moments) in the coarse-scale equations. Different treatments of the nonlinear

terms $\overline{\lambda k \cdot \nabla p}$ and $\overline{vf}$ lead to different upscaling procedures [15].

In practice, the coarse-scale models are often taken to be the same form as the fine-scale model (Eqs. (2.3) and (2.5)), but with the fine-scale parameters being replaced by coarse-scale quantities

$$div[\lambda^*(S^c)k^* \cdot \nabla p^c] = 0, \tag{2.10}$$

$$\phi^* \frac{\partial S^c}{\partial t} + div[v^c f^*(S^c)] = 0, \tag{2.11}$$

where the superscript $*$ designates upscaled (coarse-scale) quantities and the superscript c represents coarse-scale (volume-averaged) variables. The upscaled quantities are computed through appropriate numerical procedures such that the coarse-scale variables to be solved in Eqs. (2.10) and (2.11) are as close as possible to the fine-scale solution.

The upscaled quantities can be categorized into the upscaled single-phase flow parameters and the upscaled multiphase flow functions. When the coarse-scale model involves only the upscaled single-phase parameters k^*, the model is referred to as *primitive coarse-scale model*, described as follows.

$$div[\lambda(S^c)k^* \cdot \nabla p^c] = 0, \tag{2.12}$$

$$\phi^* \frac{\partial S^c}{\partial t} + div[v^c f(S^c)] = 0. \tag{2.13}$$

We can see the fine-scale relative permeability functions, $\lambda(\cdot)$ and $f(\cdot)$, are retained in the primitive coarse-scale model. The primitive model does not account for the transport effects in the upscaled model. It may be applicable for cases in which the subgrid permeability heterogeneity is small, such as the cases with moderate coarsening level or non-uniform grids to minimize the heterogeneity within coarse blocks.

In more general cases, especially with large upscaling ratios, the upscaled two-phase functions $\lambda^*(S^c)$ and $f^*(S^c)$ in Eqs. (2.10) and (2.11) need to be additionally considered. The representation of $\lambda^*(S^c)$ and $f^*(S^c)$ in the coarse model is equivalent to the use of upscaled relative permeability functions $k^*_{rj}(S^c)$ (referred to (2.2), (2.4), and (2.6)). This type of upscaling is multiphase upscaling. As it will be described in the next section, multiphase upscaled transport parameters are more challenging to compute than the single-phase flow parameters.

It should be kept in mind that Eqs. (2.10) and (2.11) only represent one form of the coarse-scale model. There exist other models to represent the subgrid effects due to the nonlinear terms. Efendiev and Durlofsky (2003) [15] presented a generalized convection-diffusion model, which introduced a diffusive term to model the subgrid effects in Eq. (2.9), in addition to the convective correction as shown in Eq. (2.11). We point out that both the diffusive and convective terms in [15] need to be numerically determined, analogous to the computation of $\lambda^*(S^c)$ and $f^*(S^c)$ here. Therefore, the issue of global flow dependency of the upscaled terms also exists in the generalized convection-diffusion model.

2.2. Upscaling for Flow and Transport

The accuracy of the coarse-scale model and the efficiency of the upscaling procedures depend to a large extent on how the upscaled two-phase functions are computed. In this section, we briefly review the existing upscaling techniques.

2.2.1. Single-phase upscaling

If $k_{rw} = S$, $k_{ro} = 1 - S$ and $\mu_w = \mu_o$, then the flow equation reduces to

$$div(k(x) \cdot \nabla p) = q_t \quad \text{in } \Omega. \tag{2.14}$$

In single-phase upscaling, only pressure equation is involved. The coarse-scale equation has the same form as the fine-scale equation except that the coefficients are replaced by effective, homogenized coefficients as follows

$$div(k^*(x) \cdot \nabla p^c) = q_t \quad \text{in } \Omega.. \tag{2.15}$$

The effective coefficients in upscaling methods are computed using the solution of the local problem in a representative volume V_{i^c,j^c}, Figure 2.2. For simplicity, we neglect

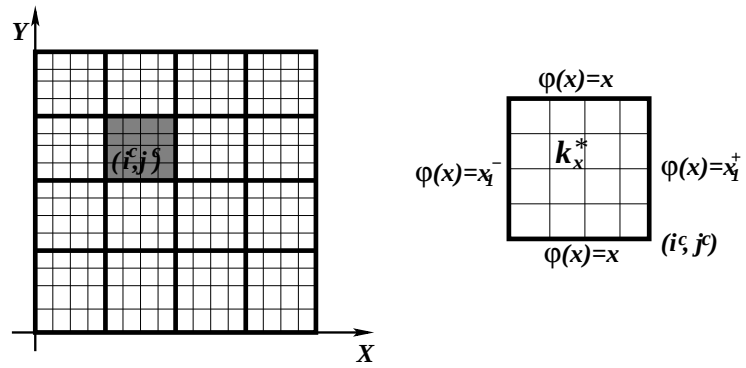

(a) Representative volume (ic, jc) (b) Local calculation for upscaled coeffcient

Fig. 2.2. Schematic showing a local single-phase upscaling. Local problem (2.16) and (2.17) is solved to compute k_x^*, the unit vector used is $e = e^1 = (1, 0)$.

subscript $_{i^c,j^c}$ in the following discussion. On V, the local problem is defined as

$$div(k(x) \cdot \nabla \phi_e(x)) = 0 \quad \text{in } V, \tag{2.16}$$

$$\phi_e(x) = x \cdot e \quad \text{on } \partial V, \tag{2.17}$$

where e is a unit vector, $x = (x_1, x_2) \in \mathbb{R}^2$.

It is sufficient to solve (2.16) and (2.17) for d linearly independent vectors e^1, ..., e^d in $\mathbb{R}^d$ because $\phi_e = \sum_i \beta_i \phi_{e^i}$ if $e = \sum_i \beta_i e^i$. Here V denotes a coarse grid block, though one can use a smaller region. The effective coefficients are computed in each

V as

$$k^*(x) \cdot e = \frac{1}{|V|} \int_V k(x) \cdot \nabla \phi_e dx. \tag{2.18}$$

We note that k^* (which is not the same as the homogenized coefficients) is a symmetric and positive definite provided k is symmetric and positive definite. For (2.16), one can use various boundary conditions, including periodic boundary conditions as well as oversampling methods. We refer to [14, 35] for the discussion on the use of various boundary conditions.

2.2.2. Pseudo-relative permeabilities for multiphase upscaling

For two-phase upscaling, the upscaled two-phase functions λ^* and f^* are computed to preserve the averaged fine-scale total flow rate and fractional flow. The total flow rate

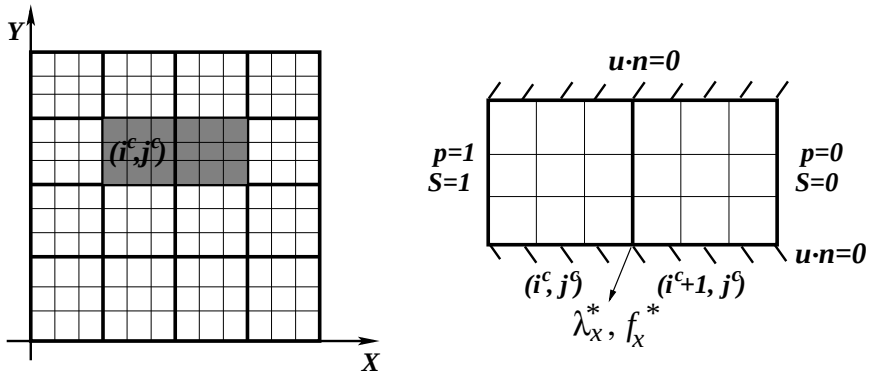

Fig. 2.3. Schematic showing a local multiphase upscaling of transport parameters λ^* and f^*, a constant pressure-no flow boundary condition is applied.

is preserved via the upscaled total mobility function $\lambda^*(S^c)$. By comparing Eq. (2.10) and Eq. (2.8), $\lambda^*(S^c)$ needs to satisfy

$$\lambda^*(S^c)k^* \cdot \nabla p^c = \overline{\lambda k \cdot \nabla p} = -\overline{v}, \tag{2.19}$$

where $\overline{v}$ designates the averaged fine-scale total velocity. The x component in the above equation gives $\lambda_x^*(S^c)k_x^*\Delta p^c/\Delta x^c = \overline{v}_x$, where Δp^c represents a pressure difference (of opposite sign to ∇p^c). Therefore $\lambda_x^*(S^c)$ can be computed as

$$\lambda_x^*(S^c) = \frac{\overline{v}_x}{k_x^*\Delta p^c/\Delta x^c} = \frac{\overline{v}_x \Delta y^c h}{(k_x^*\Delta p^c/\Delta x^c)\,\Delta y^c h} = \frac{\overline{q}_x}{T_x^*\Delta p^c}, \tag{2.20}$$

where Δx^c and Δy^c designate the dimensions of a coarse grid block, h is the model thickness, $\overline{q}_x$ is the total flux in the x direction, and k_x^* and T_x^* are coarse-scale permeability and transmissibility in the x direction.

In a discrete form, λ_x^* defined at the interface of two adjacent coarse blocks (e.g., i and $i+1$ as shown in Fig. 2.3 is computed via

$$(\lambda_x^*(S^c))_{i+1/2} = \frac{\langle q_x\rangle_{i+1/2}}{\left(\hat{T}_x^*\right)_{i+1/2}(\langle p\rangle_i - \langle p\rangle_{i+1})}, \tag{2.21}$$

where $\langle q_x\rangle$ designates the integrated total fine-scale flux through the interface and $\langle p\rangle$ is the volume average of the fine-scale pressure over the coarse block. In the above equation, $\hat{T}_x^*$ represents an upscaled single-phase transmissibility, computed at the same time with the calculation of λ_x^*. Note that it is different than T_x^*, the upscaled transmissibility obtained from single-phase flow upscaling, and applied later in global coarse-scale simulations. The quantity $\hat{T}_x^*$ is computed from the initial time of the local two-phase flow simulation, when the system is still single-phase. In general, the value of $\hat{T}_x^*$ will be different than T_x^* used in the coarse-scale simulation, which may be computed using different (local, quasi global or global) single-phase upscaling approaches. The separate determination of λ_x^* and T_x^* decouples the single and two-phase upscaling computations, and allows us to focus on the issues specific to two-phase upscaling. For more detailed discussion, refer to [5].

For the coarse-scale transport equation Eq. (2.11), the upscaled fractional flow

function $f^*(S^c)$ is computed to preserve the averaged fractional flow $\overline{vf}$ in the volume averaged saturation equation (Eq. 2.9), which gives

$$v^c f^*(S^c) = \overline{vf}. \tag{2.22}$$

The directional fractional flow function in the x direction can be determined via

$$f_x^*(S^c) = \frac{\overline{v_x f}}{\overline{v}_x}. \tag{2.23}$$

And $f_x^*(S^c)$, defined at the interface of two coarse blocks, is computed as

$$(f_x^*(S^c))_{i+1/2} = \frac{\langle v_x f \rangle_{i+1/2}}{\langle v_x \rangle_{i+1/2}} = \frac{\langle q_{xw} \rangle_{i+1/2}}{\langle q_x \rangle_{i+1/2}}, \tag{2.24}$$

where $\langle q_{xw} \rangle$ and $\langle q_x \rangle$ represent the integrated fine-scale water and total flux through the coarse-block interface. Analogously, the quantities λ_y^* and f_y^* can be computed with the local flow imposed in the y direction.

Note that both λ^* and f^* are dynamic quantities, and are represented as functions of coarse-scale saturation S^c. In this work, the quantity S^c associated with λ^* and f^* is computed as the average saturation over the fine-scale cells along the block interface. This is to be consistent with the numerical scheme applied here, a second-order Total-Variation-Diminishing (TVD) scheme.

CHAPTER III

TWO-PHASE UPSCALING FOR FLOW AND TRANSPORT*

In this chapter, we study two-phase upscaling method for flow and transport. We propose the TOF-based two-phase upscaling and local-global two-phase upscaling. In these two approaches, the global flow information is incorporated into local boundary conditions for the calculation of the upscaled flow and transport functions.

3.1. Global Flow Dependence of Transport Functions

3.1.1. Local v.s. global two-phase upscaling

First, we study the dependence of the upscaled transport functions λ^* and f^* on the global information of saturation by an example. This example involves a periodic permeability field, which is generated by replicating a 10×10 permeability template (as displayed in Fig. 3.1 top). The template is extracted from a log normal permeability distribution of dimensions 100×100, and with dimensionless correlation lengths $l_x = 0.4$ and $l_y = 0.01$. The resultant 100×100 periodic permeability field is shown in Fig. 3.1 bottom, with the same 10×10 permeability pattern repeated in the domain.

We consider two-phase flow with fine-scale relative permeabilities $k_{rw} = S^2$ and $k_{ro} = (1 - S)^2$, and the endpoint water-oil mobility ratio $M = 5$. The fine-scale periodic permeability field is uniformly coarsened to 10×10. Therefore the fine-scale permeability heterogeneity within each coarse block (of dimensions 10×10) remains the same. We apply both the local and global two-phase upscaling methods

* Part of this chapter is reprinted with permission from Y. Li, Y. Efendiev, R. E. Ewing, G. Qin, and X. H. Wu, *An accurate multiphase upscaling for flow and transport in heterogeneous porous media*, in Proceedings of the 15th Middle East Oil&Gas Show and Conference, Bahrain, 2007, paper SPE105377-PP, Copyright 2007, SPE.

to compute the upscaled two-phase functions.

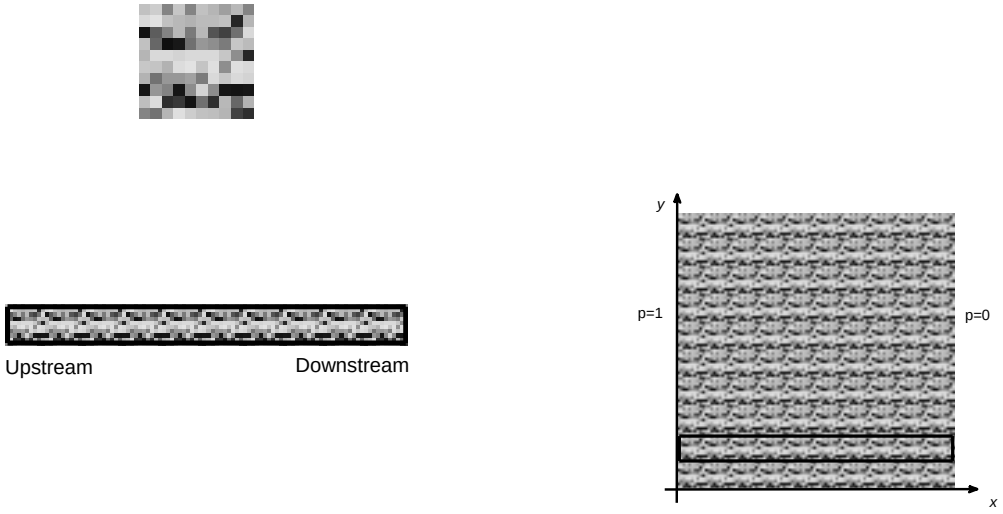

Fig. 3.1. A periodic permeability field generated by a template.

Shown in Fig. 3.2 are the results of λ^* (in the x direction) using local two-phase upscaling with standard boundary conditions. It displays λ_x^* for one row of the coarse blocks (as shown in Fig. 3.2c). Each subplot here represents one coarse-block interface from the upstream (indexed by $(2,1)$) to downstream (indexed by $(2,10)$), where the first index indicates the row number. In Fig. 3.2, the dotted curve designates the input fine-scale mobility function λ, while the dot-dash curve the upscaled function λ_x^*. Due to the same permeability heterogeneity within each coarse block and the same set of local boundary conditions imposed to each local region (to compute λ_x^*), the resultant λ_x^* are the same for all the coarse-block interfaces from the upstream to downstream.

Similarly, the results of λ_x^* for one row of the coarse blocks using the global two-phase upscaling approach is shown in Fig. 3.3. Note that λ_x^* is computed from a generic global flow in the x direction. Again, the input fine-scale λ is represented

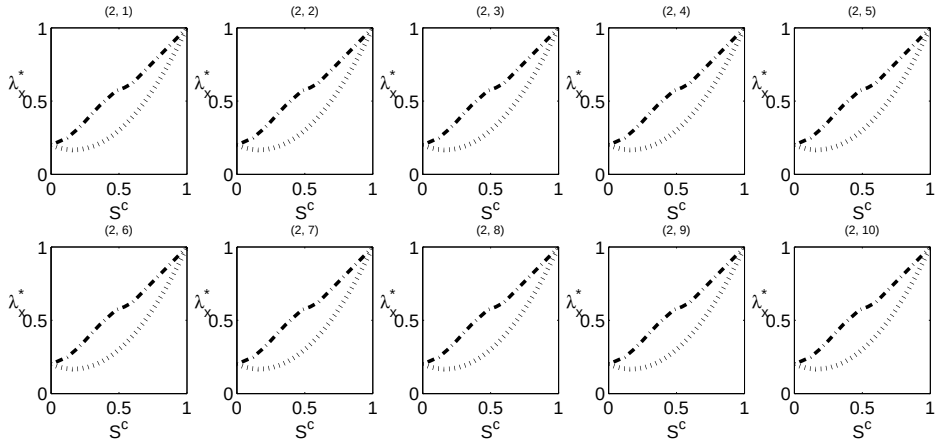

Fig. 3.2. Upscaled total mobility function λ_x^* from local two-phase upscaling with standard local boundary conditions for one row of the coarse-scale blocks from the periodic permeability field.

by the dotted curve, while the upscaled λ_x^* by the dot-dash curve. We note that λ_x^* displays a clear trend from the upstream to downstream interfaces (indexed from $(2,1)$ to $(2,10)$), different from the results shown in Fig. 3.2. In the upstream, λ_x^* shows the largest deviation from the input fine-scale λ, then the deviation gradually decreases from the upstream to downstream. Recall that the underlying fine-scale permeabilities within each coarse block are the same. Therefore the trend in the resultant λ_x^* is driven by a global flow dependency. Given the fact that for the periodic permeability field, the pressure differences and fluxes remain constant for each coarse block, the global flow dependency in fact lies in the saturation. We note that this effect (the global dependency of saturation) is evident, but it is not considered at all in the local upscaling methods.

The use of EFBC local upscaling gives results similar to those shown in Fig. 3.2 (from standard local upscaling). Due to the attenuated fluxes specified in EFBCs, the λ_x^* from EFBCs will be lower than those shown in Fig. 3.2; however λ_x^* remains

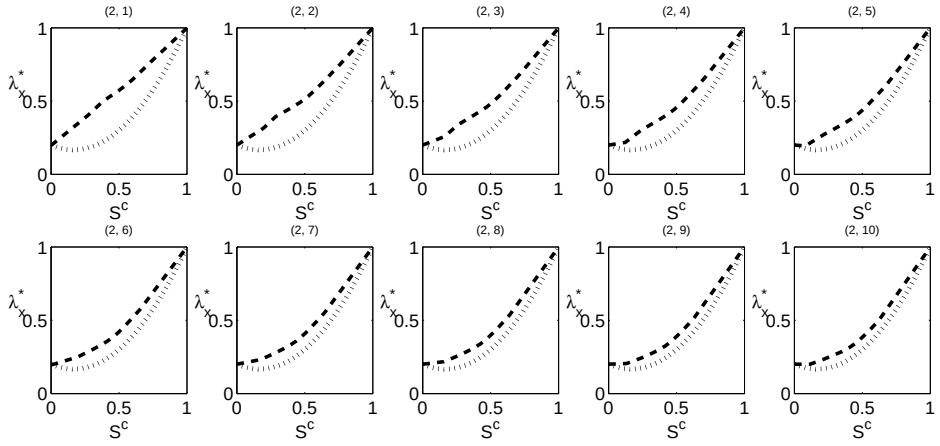

Fig. 3.3. Upscaled total mobility function λ_x^* from global two-phase upscaling with standard local boundary conditions for one row of the coarse-scale blocks from the periodic permeability field.

the same from the upstream to the downstream. This is because EFBCs do not modify the saturation boundary conditions, i.e., it uses the same local saturation boundary conditions as standard local upscaling. Therefore, the EFBCs local two-phase upscaling cannot capture the global trend of λ_x^* revealed in global upscaling (as shown in Fig. 3.3) either.

3.1.2. Performance of existing two-phase upscaling techniques

The discrepancy in the upscaled two-phase functions from the local and global methods will result in different coarse-scale flow predictions. Now we compare different coarse-scale results with reference to fine-scale solutions.

A more realistic permeability field is applied here. It involves a log normal permeability distribution, generated using sequential Gaussian simulation [11]. The permeability field, shown in Fig. 3.4a, is characterized by dimensionless correlation length $l_x = 0.4$ and $l_y = 0.01$ and with $\sigma = 2$, where σ^2 is the variance of $\log k$.

We also consider other permeability distributions with various correlation lengths, as shown in Figs. 3.4b-d. Their applications will be presented in Section 3.2 and Section 3.3. For all the permeability fields considered in this dissertation, a spherical variogram model is applied.

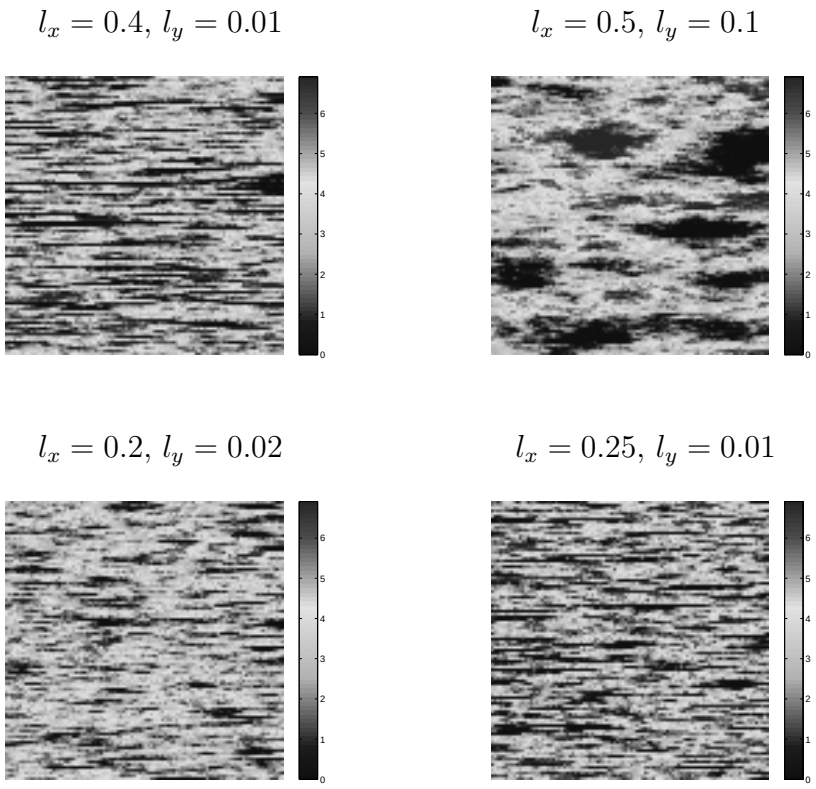

Fig. 3.4. Permeability distributions of dimensions 100×100 with different correlation lengths, shown in log scale. For all the permeability fields, the variance (σ^2) of $\log k$ is 4.0.

The fine-scale model, of dimensions 100×100, is uniformly coarsened to 10×10. We consider a flow problem driven by a pressure difference in the x direction. This is accomplished by setting $p = 1$ over the left edge of the model and $p = 0$ over the right edge. The system is initially saturated with the non-aqueous (oil) phase (i.e., $S = 0$). For the solution on the fine and coarse scales, an implicit pressure, explicit

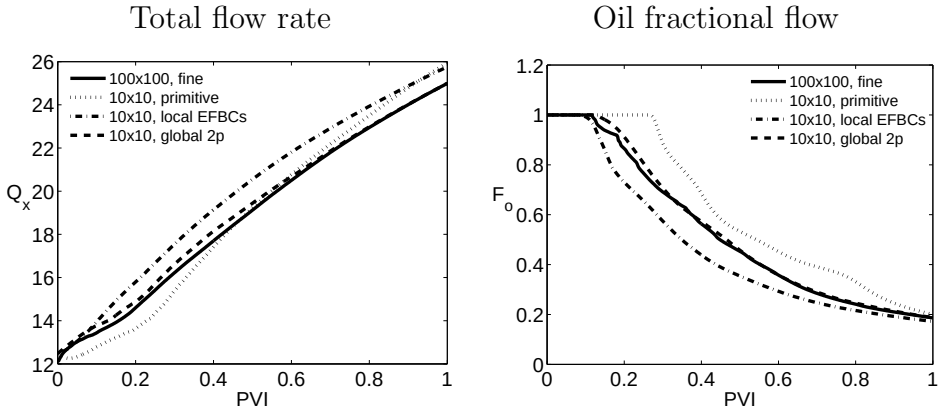

Fig. 3.5. Flow results of EFBC local two-phase upscaling and global two-phase upscaling for a log normal permeability field ($l_x = 0.4$, $l_y = 0.01$, and $\sigma = 2.0$).

saturation (IMPES) procedure is employed, and a second-order TVD scheme is applied to solve the saturation equation. For the upscaled single-phase flow parameters, we employ an accurate global transmissibility upscaling approach, so we can focus on the performance of different two-phase upscaling methods. This applies to this and all the subsequent cases. With the specified pressure boundary conditions, we compare the fine and coarse-scale flow results in terms of total flow rate of fluid and the flowing fraction of oil at the outlet edge of the model. Those are typical quantities that represent the flow and transport predictions of a model.

Fig. 3.5 shows the results for the permeability field with $l_x = 0.4$ and $l_y = 0.01$ (shown in Fig. 3.4a). Here we use a dimensionless time, pore volume injected (PVI), defined as $\frac{1}{V_p}\int_0^t Q(\tau)d\tau$, where V_p is the total pore volume. Compared to the fine-scale solution (represented by the solid curve), the primitive model (the dotted curve) shows evident errors, especially for the transport predictions (Fig. 3.5b). This late breakthrough is very typical for primitive coarse models (without any upscaled two-phase functions), as the fine-scale permeability features are not captured in the coarsened model.

Also shown in Fig. 3.5 are the results using local (EFBC) and global two-phase upscaling. The use of the upscaled two-phase functions is to correct the bias in the primitive model. We see that the EFBC local upscaling still presents errors (the dot-dash curve). Opposite to the primitive model, it shows overestimated total flow rate and a bias towards earlier breakthrough. EFBCs, however, already improved the results using standard local upscaling (not shown here), which in fact gives more severely overestimated flow rate and earlier breakthrough. We point out that for some cases, EFBC local upscaling does provide results that are close to the fine-scale solution, but it fails to capture the fine-scale results for cases with relatively short correlation lengths in one direction (as in the case shown here).

In contrast to the local methods, the global two-phase upscaling displays accurate coarse-scale predictions for both flow and transport results (the dashed curves in Fig. 3.5). This illustrates that the global flow dependency captured in the global two-phase upscaling plays an important role in the accurate predictions of coarse models. With the upscaled two-phase functions appropriately computed, the coarse model can reproduce the fine-scale solution very well. However, as discussed earlier, although global two-phase upscaling provides accurate coarse models, it is not practically feasible due to its high computational cost. Our focus will be on the development of local two-phase upscaling methods, but with the global flow information appropriately accounted for. Next we present a TOF-based two-phase upscaling procedure which effectively incorporates global single-phase flow information, and avoids solving global fine-scale two-phase flow.

3.2. TOF-Based Two-Phase Upscaling

In TOF-Based two-phase upscaling, we focus on the upscaling of transport parameters. For the calculation upscaled flow parameters, we use existing local upscaling method e.g. local, global, EFBCs. For the upscaling of transport parameters, we propose an improved saturation boundary condition using global single phase information, time-of-flight. The motivation is from a recent asymptotic analysis ([16]) , where the authors show that the single-phase flow can have dominant effect on two-phase flow simulations. From this asymptotic analysis, it follows that the saturation is a smooth function of single-phase time of flight and, thus, it can be approximated via a linear function of time of flight. We write saturation as a function of time-of-flight τ and time t, $S(x,t) = S(A\tau(x) + Bt + C)$. This function is used as the saturation inlet boundary conditions in the local flow simulation. Time-of-flight τ is computed on the fine grid at time zero on the whole domain, so it contains the fine-scale global flow information. Through the use of τ the fine-scale global flow information is incorporated and through the use of t the local boundary condition is updated as time. Thus, we simulate the time-dependent saturation boundary condition in the local region. The numerical results show that this accurate saturation boundary condition significantly improves the production prediction.

3.2.1. Asymptotic analysis

In the analysis of the saturation, we introduce the *streamline* function $\psi(x)$ and the *time-of-flight* function $\tau(x)$ associated with the velocity field $v^0(x) = v(x,0) = (v_x^0, v_y^0)$ [12]. The streamline function $\psi(x)$ satisfies $\nabla \times \psi = v^0(x)$, i.e.,

$$\frac{\partial \psi}{\partial x} = -v_y^0, \quad \frac{\partial \psi}{\partial y} = v_x^0. \tag{3.1}$$

The time-of-flight function $\tau(x)$ is defined by the following curvilinear integral along a streamline arc with end points x_0 and x:

$$\tau(x) = \int_{x_0}^{x} \frac{1}{v_l^0} dl \tag{3.2}$$

$$\tau(x)|_{x_0} = 0 \tag{3.3}$$

where, l is the streamline, v_l^0 represents the length of v^0 along the arc, and x_0 means the starting point of the streamline. By (3.2), the time-of-flight τ can be viewed as the travel time of a tracer particle along a streamline ψ. Here, we will always assume that x_0 is on the left boundary of domain $\Omega = [0,1] \times [0,1]$, namely, $x_0 = \{(x,y) \in \Omega | x = 0\}$. Then, it is easy to check that the time-of-flight defined in this way satisfies the relation

$$v^0(x) \cdot \nabla \tau(x) = 1, \tag{3.4}$$

$$\tau((0,y)) = 0, \ \forall y \in [0,1]. \tag{3.5}$$

To achieve high accuracy in the coarse-scale simulations, the boundary conditions for the saturation need to be adapted to the global flow directions. We propose the use of time of flight associated with single-phase flow in imposing the saturation boundary conditions. The motivation stems from an asymptotic analysis presented in [16]. First, we briefly mention some analytical results from [16]. Denote the initial stream function and pressure by $\eta = \psi(x, t = 0)$ and $\zeta = p(x, t = 0)$. Then the equation for the pressure can be written in the (η, ζ) coordinate system as

$$\frac{\partial}{\partial \eta}(|k|^2 \lambda(S) \frac{\partial p}{\partial \eta}) + \frac{\partial}{\partial \zeta}(\lambda(S) \frac{\partial p}{\partial \zeta}) = 0 \tag{3.6}$$

where $k = kI$, I is the identity matrix. For simplicity, $S(x) = 0, x \in \Omega$ at time zero is assumed. We consider a typical boundary condition that gives high flow within

the channel, such that the high flow channel will be mapped into a large slab in the (η, ζ) coordinate system. If the permeability variation within the channel (in the η direction) is weak, the saturation within the channel will depend on ζ. In this case, the leading order pressure $\hat{p}$ will depend only on ζ, and it was shown ([16]) that

$$p(\eta, \zeta, t) = \hat{p}(\zeta, t) + \text{ high order terms}, \tag{3.7}$$

where $\hat{p}(\zeta, t)$ is the dominant pressure. This asymptotic expansion shows that the pressure (which varies in time due to saturation effects) depends strongly on the initial pressure ζ; i.e., the leading order term in the asymptotic expansion is a function of initial pressure and time only. This initial pressure contains global information. From (3.7), it follows that

$$v = C^*(x, t)v^0, \tag{3.8}$$

where v^0 is single-phase flow velocity field, v is two-phase flow velocity field, and C^* is a smooth (coarse-scale) function. Using time of flight function τ, the saturation equation for two-phase transport can be written in terms of τ in the following way:

$$\frac{\partial S}{\partial t} + C^* \frac{\partial S}{\partial \tau} = 0 \tag{3.9}$$

This equation suggests that S is a smooth function of τ and t away from interfaces which can be tracked separately. This is an underlying idea of the proposed approach. Because S is a smooth function in terms of τ and t, we propose to approximate the local boundary conditions for S using a linear function in τ and t. More precisely, S at the inlet boundary can be described by

$$S|_{\text{inlet}} = At + B\tau + C, \tag{3.10}$$

where A, B and C are fine-scale functions. This is a first order approximation. Eq.

(3.9) suggests that one can perform pseudo computations using flow based grids. However, our objective is to set boundary conditions in a general grids using global information from single-phase flow simulations. Next step, we will discuss about the determination of A, B and C.

3.2.2. Accurate saturation boundary condition

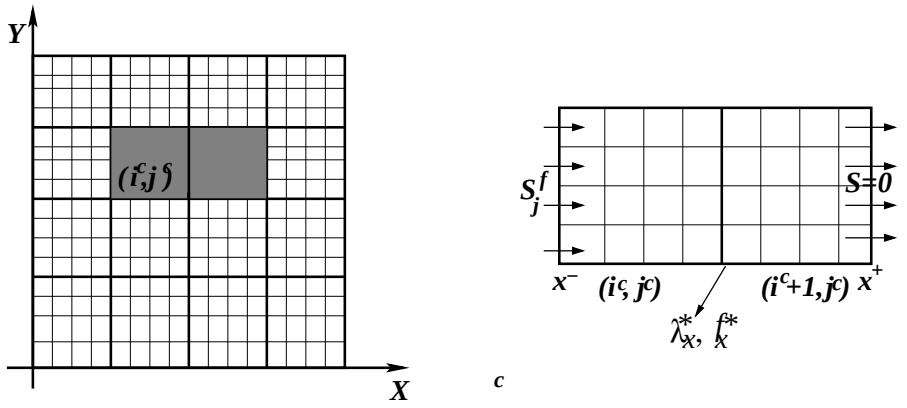

(a) Global fine−scale time−of−flight

(b) Local fine−scale flow for two−phase upscaling

Fig. 3.6. Schematic showing TOF-based two-phase upscaling. The local boundary conditions of local fine-scale flow are determined from global fine-scale time-of-flight.

Assume the whole domain is Ω, shown in Fig. 3.6, which contains total $n_x^c \times n_y^c$ coarse blocks, indexed by (i^c, j^c). In a local fine-scale region, assume that it contains $n_x^f \times n_y^f$ fine-scale cells and is indexed by (i, j). At the inlet boundary (x^-), the saturation boundary condition is chosen as:

$$(S_j^f)_{x^-} = a_1 t + c\frac{\tau_{\max} - \tau_j}{\tau_{\max} - \tau_{\min}}|_{x^-} \quad 1 \le j \le n_y^f. \tag{3.11}$$

Here the superscript f represents the fine-scale quantities, j is the fine-scale index along the local boundary. a_1 designates the temporal change of local boundary con-

dition, it need to be predetermined (we will discuss this later). $\tau_{\max}$ and $\tau_{\min}$ are local maximum and minimum of time of flight on the edge (x^-),

$$\tau_{\max} := \max_{1\le j\le n_y^f} \{\tau_j\}_{x^-}, \quad \tau_{\min} := \min_{1\le j\le n_y^f} \{\tau_j\}_{x^-}. \tag{3.12}$$

$\dfrac{\tau_{\max}-\tau_j}{\tau_{\max}-\tau_{\min}}$ is an approximation of the variation of local fine-scale of saturation. At $\tau_j = \tau_{\max}$, $\dfrac{\tau_{\max}-\tau_j}{\tau_{\max}-\tau_{\min}} = 0$ and at $\tau_j = \tau_{\min}$, it is one. This fine-scale variation is neglected in the standard two-phase upscaling methods. In the existing methods, the inlet saturation is simplified as $S = 1$, which leads an overestimation of the saturation, see Fig. 3.7 . As a consequence, the overestimation introduces an earlier breakthrough in oil cut prediction.

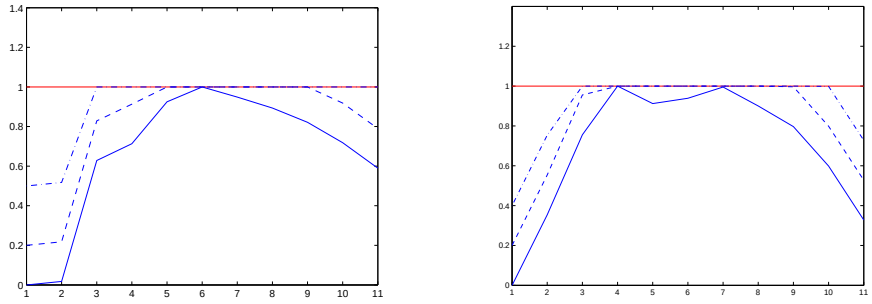

Fig. 3.7. The saturation on two different coarse blocks. It shows that the overestimation of saturation in local region. The red line is standard two-phase upscaling with $S_{\text{inlet}} = 1$, the blue solid and dot-dash lines are the real saturation from global two-phase flow, both the distribution and mean changes with time.

In (3.11), we also introduce a parameter c, which represents the spatial trend of the saturation in the global field. This was not considered in our previous work [26]. At the inlet edge (x^-), c is defined as

$$c|_{x^-} := \frac{\min_{1\le i^c\le n_x^c} \langle\tau\rangle|_{x_{i^c}^-}}{\langle\tau\rangle|_{x^-}}. \tag{3.13}$$

$c = 1$ on the very upstream coarse block ($\min\limits_{1\le i^c\le n_x^c} \langle\tau\rangle|_{x_{i^c}^-} = \langle\tau\rangle|_{x_1^-}$) and c decreases in downstream as in Fig. 3.8.

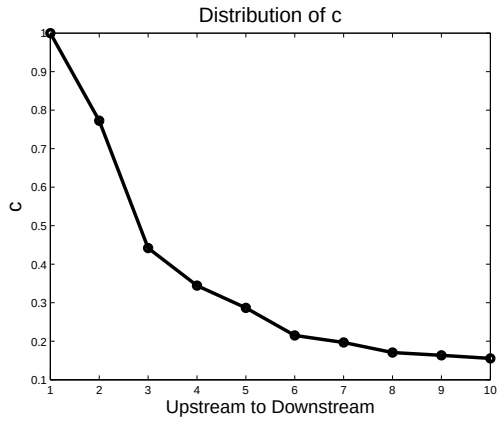

Fig. 3.8. The distribution of c from upstream to downstream in the periodic permeability field. The x-axis denotes the number of blocks indexing from upstream to downstream as 1 to 10.

In (3.11), the function includes three important global information for saturation; the temporal change of saturation is represented by $a_1 t$, the local fine-scale variation is reproduced by $\dfrac{\tau_{\max} - \tau_j}{\tau_{\max} - \tau_{\min}}$, and the global spatial trend is designated by c. Hence, (3.11) constructs an accurate saturation inlet boundary condition for local flow simulation.

At the out edge (x^+), the saturation boundary condition is set as zero,

$$(S_j^f)_{x^+} = 0 \quad 1 \le j \le n_y^f. \tag{3.14}$$

Now we compare the inlet boundary conditions for S_{real}^f from the global two-phase simulation and S^f calculated by (3.11) on one layer of coarse blocks. The permeability field is the periodic permeability field, referred in Fig. 3.1. From upstream to downstream, coarse blocks are indexed as $(1,1), ..., (1,10)$, we plot saturation on the inlet boundaries at different PVIs. At $PVI = 0$, the S_{real}^f is 1 on the first coarse block

and 0 at other blocks. We plot S^f for $PVI = 0.5$ and $PVI = 0.5$, as in Figs. 3.9. In the two figures the solid lines are the fine-scale saturation on local boundaries, the dot lines are simulated boundary condition.

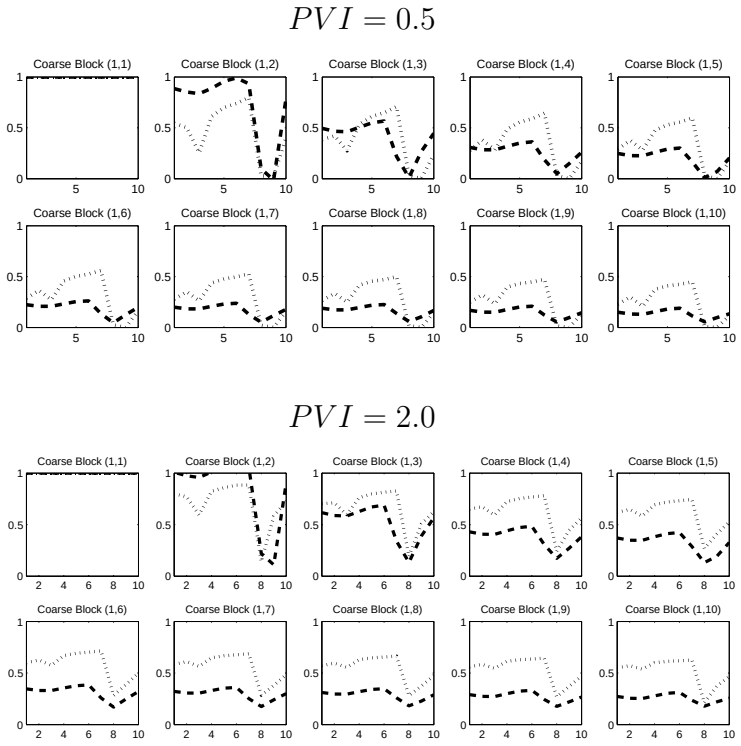

Fig. 3.9. The real saturation and simulated saturation on the local domain inlet edge.

The term $a_1 t$ increases as time and $S|x^-$ finally reaches 1 at the inlet. If a_1 is small, then the local saturation reaches steady state before any large changes occur at the inlet. For very large values of a_1, the inlet boundary conditions reaches 1 quickly and the results are similar to standard pseudo relative permeability computations. In our simulations, we find that the results of the proposed approach depend on the values of a_1 and test various values of a_1. For shorter correlation lengths in y direction, e.g. $l_y = 0.02$ and $l_y = 0.01$, a_1 is chosen as $a_1 = 0.1$. For longer correlation lengths in y direction, e.g. $l_y = 0.1$, a_1 is chosen as $a_1 = 0.5$. Because the flow is transported

in x direction, correlation length l_y affects fluid's transportation. For larger l_y, the fluid transports faster, then we choose larger a_1. The numerical results showed us these choices of a_1 give an accurate prediction. But we want to point out that since a_1 is a coefficient for temporal trend, it cannot be determined only by single-phase flow information. In (3.11), we have single-phase information time of flight τ, which only involves flow information at time zero. So it's hard to determine a_1 in TOF-based two-phase upscaling. We are currently considering various options where one can quantify a_1. One solution is to use global coarse-scale two-phase solution, which contains the temporal information of saturation. We call this method local-global two-phase upscaling and we will discuss it in detail in Section 3.3.

In TOF-based two-phase upscaling, the global single-phase simulations are performed, we use them for the computations of upscaled permeability and the computations of the local problems. We would like to note that our approach is a modification of existing pseudo relative permeability approach, and thus also applicable to other similar approaches, e.g., local-global single-phase upscaling method [4], generalized convection-diffusion approach [15], and effective flux boundary condition approach [33, 34]. One can use single-phase flow based information in imposing saturation boundary conditions in these approaches.

3.2.3. Algorithm

The TOF-based two-phase upscaling is a modification of existing two-phase upscaling method with an accurate saturation boundary condition imposed in local flow simulation. The algorithm can be summarized as follows.

Algorithm 3.2.1. *TOF-based two-phase upscaling for flow and transport.*

- *Solve global fine-scale single-phase flow at time zero with generic boundary con-*

ditions (i.e., flow in the x and y direction) to obtain fine-scale τ_x and τ_y and upscaled absolute permeability k^*.

- *On each coarse block, calculate τ_{max}, τ_{min} and coefficients c for τ_x and τ_y respectively. And construct fine-scale local boundary conditions for saturation as defined in* (3.14).
- *Solve local two-phase problem subject to the local boundary saturation conditions defined in Step 2, and local pressure boundary conditions defined by an existing local upscaling method.*
- *Compute the upscaled two-phase functions λ^* and f^* and output the saturation and the upscaled functions.*

In the above algorithm 3.2.1, we want to emphasize that the TOF-based two-phase upscaling doesn't require extra computation compared with other local two-phase upscaling method. Since the improved saturation boundary condition is constructed from time of flight, which can be calculated from global single-phase flow. A standard approach is applied to compute the time of flight [29]. Only *Step 2* are not considered in existing local upscaling methods, but it's pretty fast.

3.2.4. Numerical result

We now present the numerical results of the TOF-based two-phase upscaling for different cases. As in the last section 3.2.2, TOF-based two-phase upscaling focus on the construction of an accurate saturation inlet boundary condition in local computation of upscaled transport functions. It can be adaptable with different local upscaling method, e.g. standard local upscaling method [9], EFBC (effective flux boundary conditions approach) [33, 34], and global single-phase upscaling method [4]. In particular, we will show numerical results of TOF-based two-phase upscaling combined

with EFBC for various permeability fields.

3.2.4.1. Results for different correlation lengths

In this section, we show the numerical results of permeability distributions with different correlation lengths as described in Section 3.1.2. The first case involves a log-normal permeability distribution with dimensionless correlation lengths $l_x = 0.4$ and $l_y = 0.01$, and $\sigma_{\log k} = 2$. The permeability field (displayed in Fig. 3.4a) was considered earlier to demonstrate the performance of existing two-phase upscaling methods (shown in Fig. 3.5). For this case, the results of the TOF-based two-phase upscaling is presented in Fig. 3.10, along with those of the primitive model and the local EFBCs method. As discussed earlier, the primitive model typically gives underestimated total flow rate and late breakthrough in the oil fractional flow; and EFBCs upscaling shows an overestimation of total flow rate and a biased oil fractional flow toward early breakthrough. In contrast to these, the TOF-based two-phase upscaling (the dashed curves in Fig. 3.10) captures the fine-scale solutions very well for both the total flow rate and oil fractional flow predictions. It shows comparable accuracy to the global two-phase upscaling (as shown in Fig. 3.5), but with significant computational savings, as the TOF two-phase upscaling avoids solving any global fine-scale two-phase flow. This example demonstrates the efficacy of the proposed TOF-based two-phase upscaling approach.

Next we consider different permeability fields, shown in Figs. 3.11 and 3.12. The corresponding permeability fields are displayed in Fig. 3.4c and 3.4d respectively. These two permeability fields are again characterized by very short correlation lengths in the vertical direction ($l_y = 0.02$ and $l_y = 0.01$, respectively), and the horizontal correlation lengths are also shorter than the previous two examples ($l_x = 0.2$ and $l_x = 0.25$, respectively). In the previous study ([5]), it is showed that EFBC local

two-phase upscaling lost accuracy for these two cases (and for cases with shorter correlation lengths in one direction in general, e.g., see Figs. 12 and 14 in [5]). Here the results of TOF two-phase upscaling as well as the EFBC local method are shown in Figs. 3.11 and 3.12. Similar to the case with $l_x = 0.4, l_y = 0.01$ (shown in Fig. 3.10), the EFBC local method (dot-dash curve) gives overestimated flow rate and biased oil fractional flow predictions towards an early breakthrough. These biases are essentially corrected by using the TOF two-phase upscaling (dashed curves in Figs. 3.11 and 3.12), which provides a coarse model that is very close to the fine-scale solution.

We also consider the permeability field characterized by relatively long correlation length. The permeability distribution with $l_x = 0.5$ and $l_y = 0.1$ is shown in Fig. 3.4b. It has a more blocky appearance than that shown in Fig. 3.4a, since here the vertical correlation length is 10 times of the previous case. We again compare the three different coarse-scale models with the fine-scale reference solution, and the results are shown in Fig. 3.13. For this case, the EFBC local upscaling (the dot-dash curve) provides a solution close to the fine-scale results (the solid curve). For cases within this parameter range (with relatively long correlation lengths in the vertical direction), similar results were observed in our previous studies (e.g., [7]). In Fig. 3.13, we see that even EFBCs give reasonable predictions, the TOF two-phase upscaling further improves the results, showing very accurate predictions (the dashed curves). As pointed out earlier, EFBCs approximately account for some global flow effects in the pressure equation, and do provide significant improvement over standard boundary conditions for appropriate parameter ranges, though not for all the cases. The TOF-based two-phase upscaling incorporates the global dependency of saturation. Therefore it can capture the fine-scale solutions for general cases in different parameter ranges.

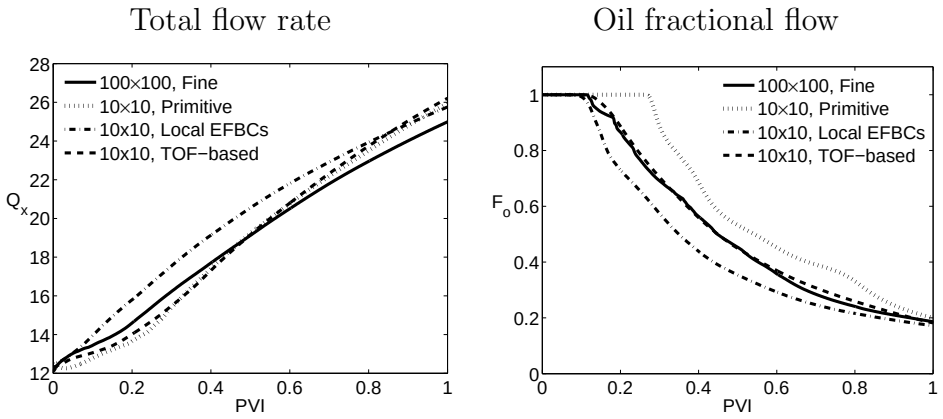

Fig. 3.10. Flow results of TOF-based two-phase upscaling (with EFBCs) for a log normal permeability field ($l_x = 0.4$, $l_y = 0.01$, and $\sigma = 2.0$), with $a_1 = 0.1$.

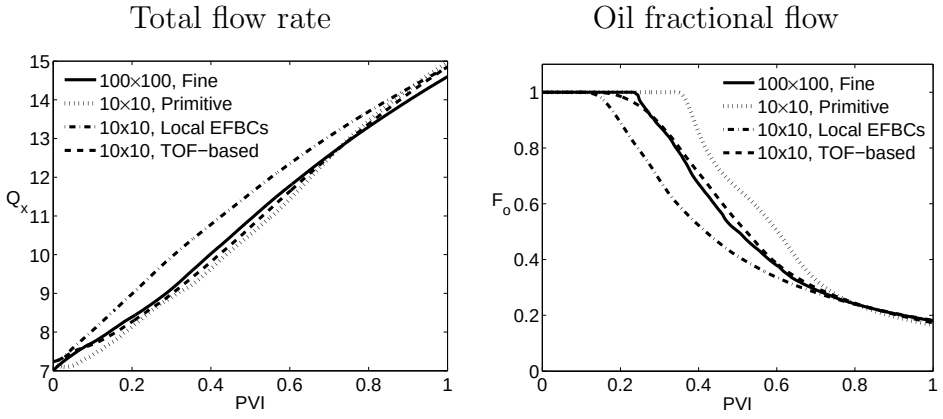

Fig. 3.11. Flow results of TOF-based two-phase upscaling (with EFBCs) for a log normal permeability field ($l_x = 0.2$, $l_y = 0.02$, and $\sigma = 2.0$), with $a_1 = 0.1$.

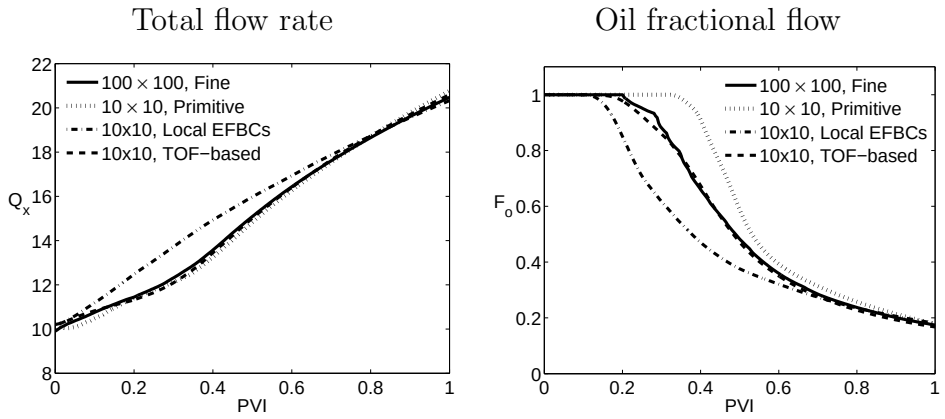

Fig. 3.12. Flow results of TOF-based two-phase upscaling (with EFBCs) for a log normal permeability field ($l_x = 0.25$, $l_y = 0.01$, and $\sigma = 2.0$), with $a_1 = 0.1$.

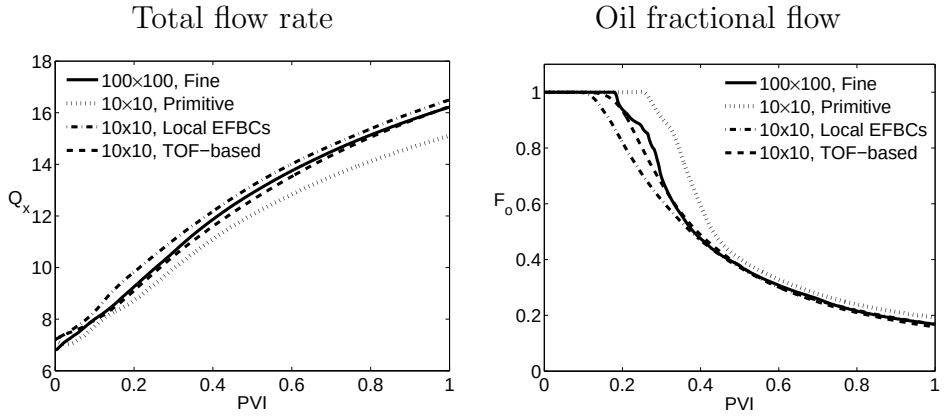

Fig. 3.13. Flow results of TOF-based two-phase upscaling (with EFBCs) for a log normal permeability field ($l_x = 0.5$, $l_y = 0.1$, and $\sigma = 2.0$), with $a_1 = 0.5$.

3.2.4.2. Results for high mobility ratio

In the last section, we considered a moderate fluid-mobility ratio ($M = 5$), which is typical in oil-water flow. The TOF two-phase upscaling approach was also applied to cases with high mobility ratios (e.g., $M = 50$ and $M = 100$), as may be encountered in gas injections for hydrocarbon recoveries from petroleum reservoirs.

We note that for the previous cases ($M = 5$), the errors associated with the primitive model mainly exist in the oil fractional flow predictions. The errors in the total flow rate are relatively small (e.g., Figs. 3.13 and 3.11). This is due to the fact that for all the cases in this work, we apply the most accurate single-phase (global transmissibility) upscaling method. And for cases with moderate mobility ratios, the accuracy of the upscaled single-phase flow parameters has a dominant impact on the accuracy of the two-phase flow results.

However, for cases with high-mobility ratios, the upscaled two-phase functions also affect considerably the results of total flow rate. In Fig. 3.15, we present the results for $M = 50$ (for the permeability field with $l_x = 0.25$, $l_y = 0.01$, shown in Fig. 3.4d). And in Fig. 3.16, the results for $M = 100$ (for $l_x = 0.4$ and $l_y = 0.01$, as shown in Fig. 3.4a) are displayed. For both cases (Figs. 3.15a and 3.16a), the accuracy of the total flow rate at PVI=0 (when the system is still of single-phase flow) is determined by the upscaled single-phase flow parameters. Then the upscaled two-phase functions act to account for the multiphase flow effects. We see that the primitive coarse model (the dotted curves in Figs. 3.15a and 3.16a) shows evident errors during the course of simulation (except for PVI=0). The TOF two-phase upscaling (the dashed curves) consistently corrects the errors as the simulation time evolves, and shows very close predictions to the fine-scale model. It again improves the results of local EFBC two-phase upscaling (the dot-dash curves in Figs. 3.15a and

3.16a), which overestimates the total flow rate, as shown in the previous cases.

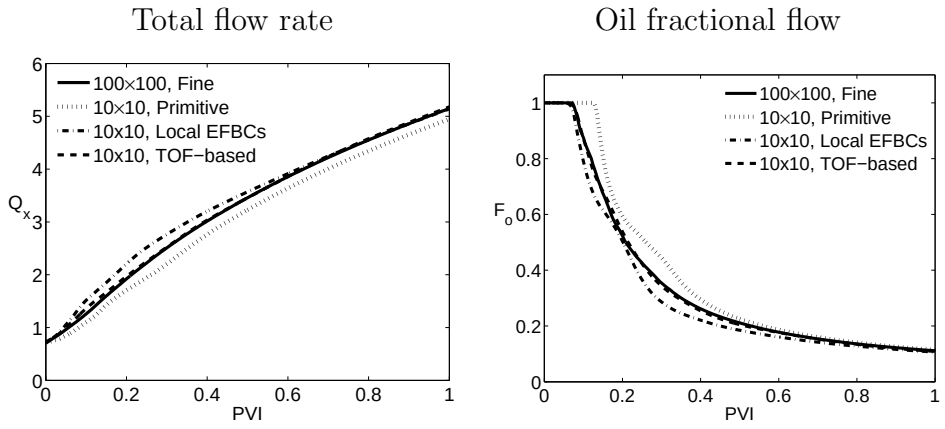

Fig. 3.14. Flow results of TOF-based two-phase upscaling (with EFBCs) for a log normal permeability field ($l_x = 0.2$, $l_y = 0.02$, and $\sigma = 2.0$), $M = 50$ and $a_1 = 0.1$.

Shown in Figs. 3.15b and 3.31b are the results for oil fractional flow for the cases with $M = 50$ and $M = 100$. Compared to the previous cases, the injected fluid (water) breaks through very fast (as illustrated in the fine-scale solutions) due to the very high-mobility ratios. The primitive coarse model again shows biased predictions towards late breakthrough, though the errors are not as large as the previous cases. Both EFBC local two-phase upscaling and the local-global two-phase upscaling correct the errors in the primitive model, especially capture the breakthrough time. We see that for these cases ($M = 50$ and $M = 100$), the errors associated with EFBC local upscaling are much smaller than the cases with $M = 5$. The TOF-based two-phase upscaling again outperforms the EFBC, consistently showing improvements over local methods.

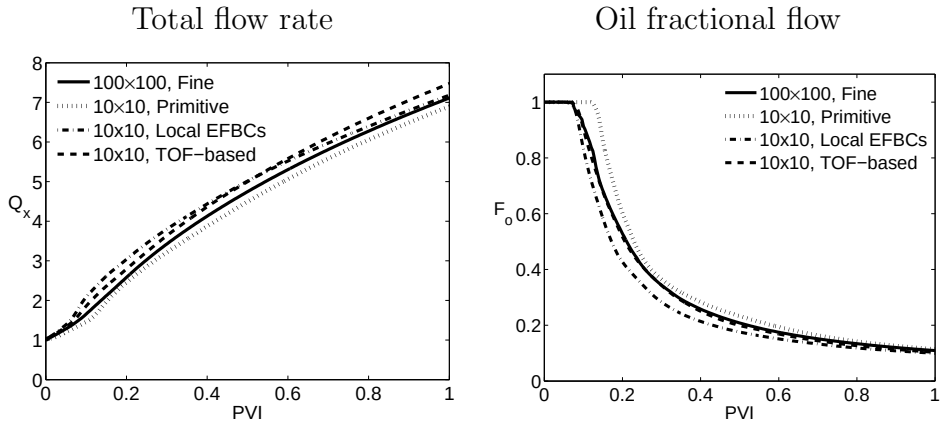

Fig. 3.15. Flow results of TOF-based two-phase upscaling (with EFBCs) for a log normal permeability field ($l_x = 0.25$, $l_y = 0.01$, and $\sigma = 2.0$), $M = 50$ and $a_1 = 0.1$.

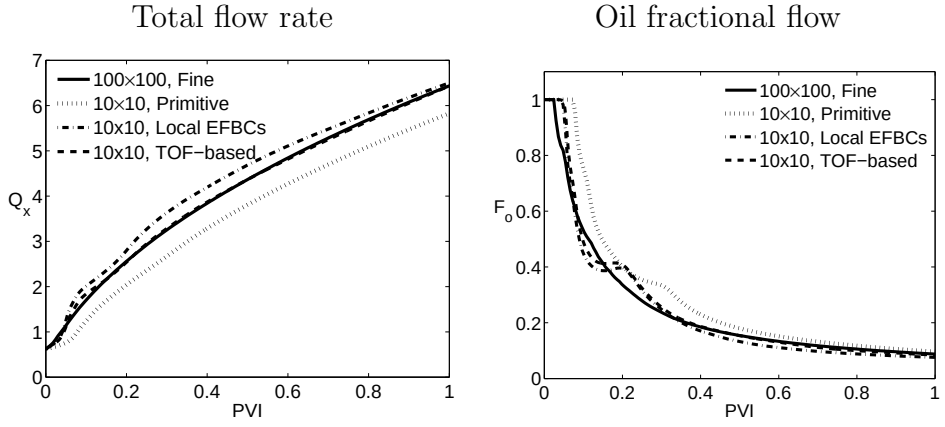

Fig. 3.16. Flow results of TOF-based two-phase upscaling (with EFBCs) for a log normal permeability field ($l_x = 0.4$, $l_y = 0.01$, and $\sigma = 2.0$), $M = 100$ and $a_1 = 0.1$.

3.2.4.3. Results for low mobility ratio

In this section, we will show some results with the mobility ratio less than 1. The mobility ratio indicates the displacement efficiency of the process. A ratio of less than 1 is favorable with an effective displacement, which happens in using biopolymers for oil recovery.

For cases with low mobility ratios, we also observe that the upscaled two-phase functions affects the results of total flow rate and oil cut. In Figure 3.17, we present the result for $M = 0.1$. As in Figure 3.17, the local EFBC two-phase upscaling (the dot-dash curve in Figure 3.17a) shows evident errors during the course of simulation. The TOF two-phase upscaling (the dashed curves) consistently corrects the errors as the simulation time evolves, and shows very close predictions to the fine-scale model. It again improves the results of the primitive coarse model (the dotted curve in Figure 3.17a).

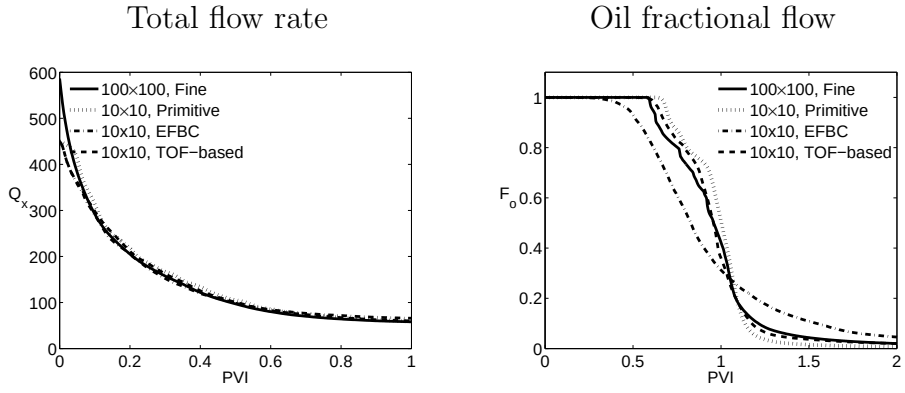

Fig. 3.17. Flow results of TOF-based two-phase upscaling (with EFBCs) for a log normal permeability field ($l_x = 0.4$, $l_y = 0.01$, and $\sigma = 2.0$), $M = 0.1$ and $a_1 = 0.1$.

3.2.4.4. Results with different pressure boundary conditions

In the above results, we show TOF combined with EFBC gives accurate flow prediction. In this section, we will combine TOF-based two-phase upscaling with other two-phase upscaling approaches and show that TOF-based two-phase upscaling is adaptable to different upscaling method. The flow upscaling considered here are standard local upscaling method (local), which set constant pressure boundary conditions; local-global upscaling method (global), which applies global single-phase flux into local pressure boundary condition.

The first case is log-normal permeability distribution with correlation lengths $l_x = 0.4$ and $l_y = 0.01$, and $\sigma_{\log k} = 2$. The permeability field (displayed in Fig. 3.4a) was considered earlier to demonstrate the performance of existing two-phase upscaling methods (shown in Fig. 3.5). For this permeability field with short correlation length, a_1 is chosen as 0.1. We show the results of TOF with standard local two-phase upscaling Fig. 3.18 and TOF with global flux two-phase upscaling Fig. 3.19. As we see in the results, the standard local two-phase upscaling gives a big overestimation of total flow rate and very late breakthrough in the oil fractional flow; the local-global two-phase upscaling corrects some of the gaps but still has overestimation of total flow rate and a biased oil fractional flow with early breakthrough. But if we combine these two upscaling with TOF-based accurate saturation boundary condition (the dashed curves in Figs. 3.18, . 3.19), the fine-scale solution is approximated very well for both the total flow rate and oil fractional flow predictions.

The second case is log-normal permeability distribution with longer correlation lengths $l_x = 0.5$ and $l_y = 0.1$, and $\sigma_{\log k} = 2$ (displayed in Fig. 3.4a) Here we let $a_1 = 0.5$. We also show the results of TOF with standard local two-phase upscaling Fig. 3.20 and TOF with local-global two-phase upscaling Fig. 3.21. We have the same

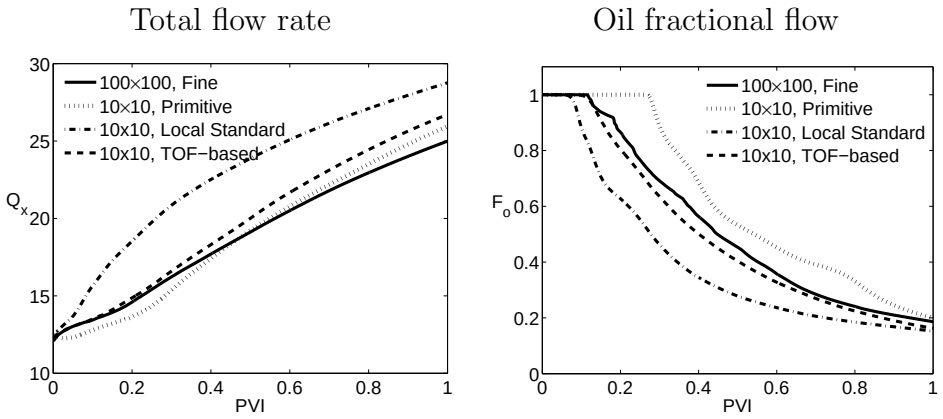

Fig. 3.18. Flow results of TOF-based two-phase upscaling (with Standard) for a log normal permeability field ($l_x = 0.4$, $l_y = 0.01$, and $\sigma = 2.0$), with $a_1 = 0.1$.

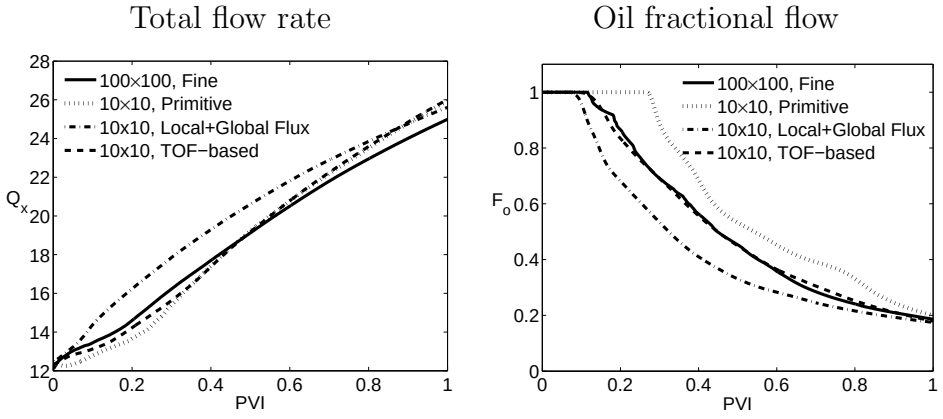

Fig. 3.19. Flow results of TOF-based two-phase upscaling (with Global) for a log normal permeability field ($l_x = 0.4$, $l_y = 0.01$, and $\sigma = 2.0$), with $a_1 = 0.1$.

observation that the standard local two-phase upscaling and local-global two-phase upscaling give overestimation of total flow rate and breakthrough in the oil fractional flow. These bias are corrected with application of TOF-based accurate saturation boundary condition in local flow simulation, (the dashed curves in Figs. 3.20, . 3.21).

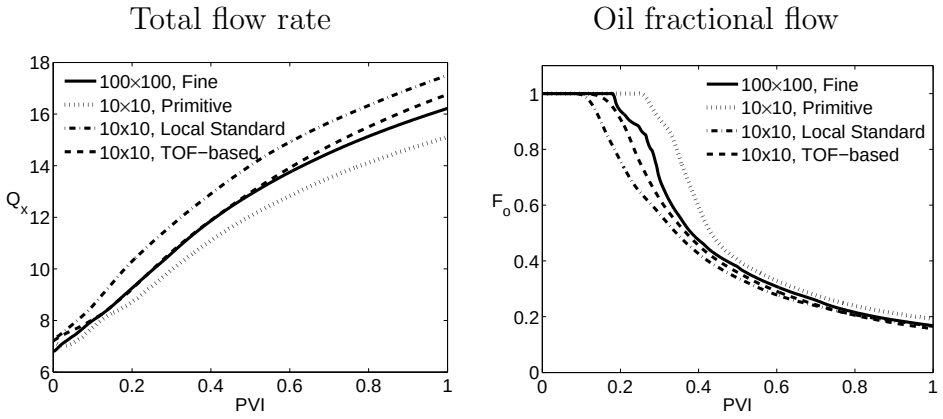

Fig. 3.20. Flow results of TOF-based two-phase upscaling (with Standard) for a log normal permeability field ($l_x = 0.5$, $l_y = 0.1$, and $\sigma = 2.0$), with $a_1 = 0.5$.

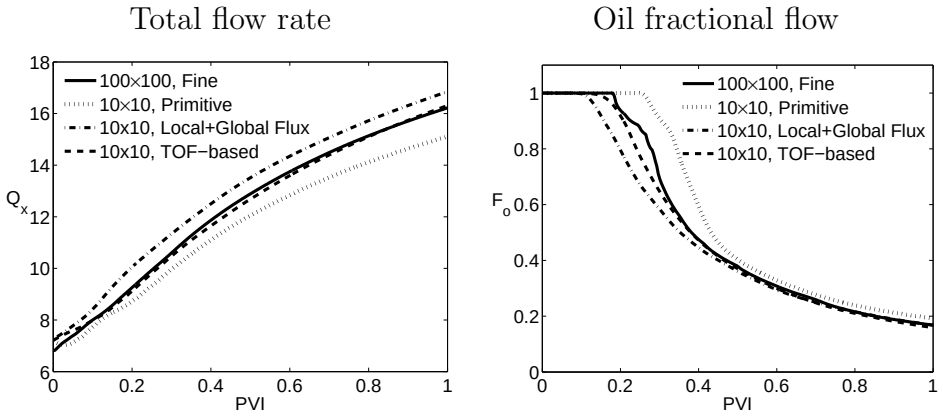

Fig. 3.21. Flow results of TOF-based two-phase upscaling (with Global) for a log normal permeability field ($l_x = 0.5$, $l_y = 0.1$, and $\sigma = 2.0$), with $a_1 = 0.5$.

3.2.5. Multiscale discontinuous galerkin method for saturation equation

In this section, we will discuss a multiscale discontinuous Galerkin method for transport equation using single-phase global information such as time-of-flight. The motivation is from the asymptotic analysis presented in Section 3.2.1. As we noted that the saturation can be expressed as a function of time t and *time-of-flight* $\tau(x)$. Here, we propose a multiscale discontinuous Galerkin method. The fine-scale time-of-flight is used as a basis function and we solve the saturation equation on a coarse grid. The saturation is approximated by a linear function of $\tau(x)$ and a 2nd-order Runge-Kutta is used for solving saturation.

Discontinuous Galerkin method is a useful tool to solve the transport problem in reservoir simulation. In [10], the authors introduced the Runge-Kutta discontinuous Galerkin methods for hyperbolic conservation laws and convection-dominated problems. This method is based on a piecewise polynomial space discretization, combined with a total variation diminishing (TVD) explicit time-stepping algorithms. A remarkable advantage of DG method is that the approximate solutions can be computed element-by-element when the elements are suitably ordered along the characteristic directions of the transport field. We will use piecewise linear polynomial to solve for the saturation by 2nd order Runge-Kutta DG method.

We use fine-scale single-phase time-of-flight $\tau(x)$ and 1 as basis functions. The saturation is approximated in each coarse grid by a piecewise linear function of $\tau(x)$. Denote the two scales as the follows, the fine scale grid is $\mathcal{T}$ and the coarse scale grid $\mathcal{T}^c$. We construct a piecewise polynomial approximation for saturation as follows,

$$S(x,t) = A^c(x,t)\tau(x) + B^c(x,t). \tag{3.15}$$

Here the coefficients $A^c(x,t)$ and $B^c(x,t)$ are coarse-scale functions, $\tau(x)$ is a fine-scale

function. We will solve the problem (3.15) on a coarse-scale grid $\mathcal{T}^c$ to compute the upscaled coefficients $A^c(x,t)$ and $B^c(x,t)$. Using (3.15), the saturation will be solved on a coarse grid. Since $\tau(x)$ is defined on the fine grid, the fine-scale heterogeneities are included in the basis functions. In this way, we will get a coarse solution that can be downscales using multiscale basis functions.

Assume the coarse-scale decomposition of domain is $\Omega = \cup_{i,j=1}^{N}\{\mathcal{T}_{ij}^c\}$. On a coarse-scale block $\mathcal{T}_{ij}^c$, the saturation S is in the form of $S_{ij}(x,t) = A_{ij}(t)\tau(x)+B_{ij}(t)$. For a fixed t, the coefficients $A_{ij}(t)$ and $B_{ij}(t)$ are constant on each coarse-scale block. Multiplying the saturation equation by 1 and $\tau(x)$ respectively, we obtain the following system

$$
\begin{cases}
\sum_{ij}[\int_{\mathcal{T}_{ij}^c}\frac{\partial(A_{ij}\tau(x)+B_{ij})}{\partial t}dx + \int_{\mathcal{T}_{ij}^c} v^n(x)\cdot\nabla f(S^n(x))dx] = 0, \\
\sum_{ij}[\int_{\mathcal{T}_{ij}^c}\frac{\partial(A_{ij}\tau(x)+B_{ij})}{\partial t}\tau(x)dx + \int_{\mathcal{T}_{ij}^c} v^n(x)\cdot\nabla f(S^n(x))\tau(x)dx] = 0.
\end{cases} \tag{3.16}
$$

Taking an average of $\tau(x)$ on $\mathcal{T}_{ij}^c$, we have

$$
\begin{cases}
\sum_{ij}[(A_{ij}^{n+1}\overline{\tau(x)}+B_{ij}^{n+1}) - (A_{ij}^{n}\overline{\tau(x)}+B_{ij}^{n})] \\
= -\sum_{ij}\frac{\Delta t}{|\mathcal{T}_{ij}^c|}\int_{\partial\mathcal{T}_{ij}^c} v^n(x)\cdot n f(A_{ij}^n\tau(x)+B_{ij}^n)dl, \\
\sum_{ij}[(A_{ij}^{n+1}\overline{\tau^2(x)}+B_{ij}^{n+1}\overline{\tau(x)}) - (A_{ij}^{n}\overline{\tau^2(x)}+B_{ij}^{n}\overline{\tau(x)})] \\
= \sum_{ij}[-\frac{\Delta t}{|\mathcal{T}_{ij}^c|}\int_{\partial\mathcal{T}_{ij}^c} v^n\cdot n f(A_{ij}^n\tau(x)+B_{ij}^n)\tau(x)dl \\
+\frac{\Delta t}{|\mathcal{T}_{ij}^c|}\int_{\mathcal{T}_{ij}^c} v^n(x)\cdot\nabla\tau(x) f(A_{ij}^n\tau(x)+B_{ij}^n)dx].
\end{cases} \tag{3.17}
$$

Denote $X = [(A_{ij});\ (B_{ij})]'$. We use $2nd$ order Runge-Kutta method in the

following way.

$$
\begin{aligned}
X^{(1)} &= X^n + \Delta t L(X^n), \\
X^{n+1} &= X^n + \frac{1}{2}\Delta t(L(X^n) + L(X^{(1)})).
\end{aligned} \tag{3.18}
$$

In the above equations, L is the discrete operator at each time step defined as in (3.17).

The algorithm of multiscale discontinuous Galerkin method is described as follows.

Algorithm 3.2.2. *Assume on the domain Ω, the coarse scale grid is $\mathcal{T}^c$, the fine grid is $\mathcal{T}$. We solve two-phase flow problem in the following way.*

- *Step 1. At $t = 0$, solve single-phase flow problem on the fine grid $\mathcal{T}$ and compute the time-of-flight $\tau(x)$.*
- *Step 2. At time step $t = t^m$, compute fine-scale velocity $v^m(x)$ on $\mathcal{T}$ by*
$$
\begin{cases}
v^m(x) = -k(x)\lambda(S^{m-1})\nabla p(x)) \\
\nabla \cdot (v^m(x)) = 0
\end{cases}.
$$
- *Step 3. At time step $t = t^n$, we solve the saturation equation on the coarse grid $\mathcal{T}^c$ by the 2nd-order Runge-Kutta system.* (3.18).
- *Step 4. Repeat Step 2 and Step 3 until $t = T$.*

Remark 3.2.1. *In Algorithm 3.2.2, $m = c_1 n + c_2$, where c_1 and c_2 are positive integers. Typically, the flow equations are solved with larger time step m.*

For the numerical result, we consider a simple permeability field that only depends on y, i.e., $k(x_1, y) \equiv k(x_2, y), \forall x_1, x_2 \in \Omega$. The permeability field is depicted in Figure 3.22 For the permeability in Figure 3.22, we assume a constant pressure drop in the horizontal direction and no flow boundary condition in the vertical direction, i.e., $p(0, y) = 1$, $p(1, y) = 0$, $v(x, 0) \cdot n(x, 0) = 0$, and $v(x, 1) \cdot n(x, 1) = 0$. We choose

the fine grid $\mathcal{T} = 100 \times 100$ and the coarse grid $\mathcal{T}^c = 20 \times 20$, we compare the fine-scale and the coarse-scale saturation distributions in Figure 3.23. The fine-scale saturation is computed by the traditional IMPES scheme and the coarse-scale saturation is computed by the TOF-based multiscale discontinuous Galerkin method, as discussed above. We observe a good agreement between fine- and coarse-scale solutions.

We can use two time-of-flight functions $\tau_x(x)$, $\tau_y(x)$ and 1 as basis functions. $\tau_x(x)$ and $\tau_y(x)$ are obtained by single-phase problems, but with different boundary conditions. For $\tau_x(x$, we put constant pressure in x direction and no-flow in y direction; for $\tau_y(x$, we put constant pressure in y direction, no flow in x direction. Including two time-of-flight functions allows to avoid specific flow direction. The saturation on each coarse block $\mathcal{T}_{ij}^c$ has the form of

$$S_{ij}(x,t) = A_{ij}(t)\tau_x(x) + B_{ij}(t)\tau_y(x) + C_{ij}(t). \tag{3.19}$$

To solve this, we can generate a similar system with (3.16) but with 3 equations, i.e., the test functions are chosen to be $\tau_x(x)$, $\tau_y(x)$ and 1. The obtained linear system can be solved either explcitly or implicitly. This is under our investigation.

3.2.6. Concluding remarks

The TOF-based two-phase upscaling focuses on more accurate representations of saturation boundary conditions in local two-phase upscaling calculations. The method uses global single-phase time-of-flight to construct the local saturation boundary conditions. Both the spatial and temporal global flow dependency of the saturation incorporated into the local calculations. It successfully corrects the bias in the existing two-phase upscaling methods.

Compared to global two-phase upscaling methods, the TOF-based two-phase upscaling has the advantage in terms of efficiency. It avoids solving global fine-scale

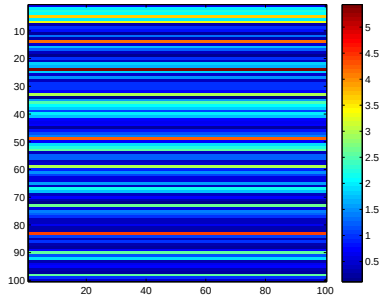

Fig. 3.22. A layered permeability field.

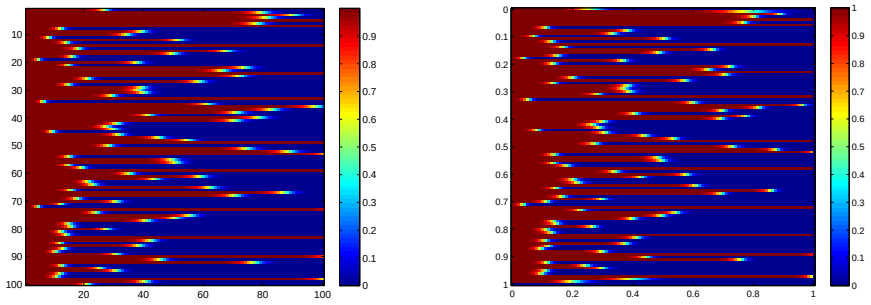

Fig. 3.23. The saturation distribution: the left figure shows the fine-scale saturation; the right figure shows the coarse-scale saturation.

two-phase flow, but can effectively account for the effects of global flow. The TOF-based two-phase upscaling does not require significant extra computation compared with the existing two-phase upscaling method. The single-phase time-of-flight is computed once at the initial time and from the single-phase pressure solution.

The coefficient a_1, which accounts for the temporal trend of saturation in the local saturation boundary conditions needs to be predetermined. We note that it may be difficult to determine a prior this time-dependent coefficient from only single-phase flow information. It is also found that the value of this coefficient (in order to obtain satisfactory coarse-scale predictions) depends strongly on the spatial correlation structure of fine-scale permeability. Therefore it is possible to tune this parameter based on underlying reservoir heterogeneities, which can then be applied to a variety of permeability distributions with similar reservoir characterizations.

Another approach is to use global coarse-scale two-phase solutions (as in the recently developed local-global two-phase upscaling approach [8]) in the local calculations for the determination of a1. This will be discussed in the next section.

3.3. Local-Global Two-Phase Upscaling

In the local-global two-phase (LG2P) upscaling approach, the local boundary conditions are directly determined from global coarse-scale solutions. In so doing, the local-global approach avoids solving global fine-scale two-phase flow (as required in the global methods), and effectively incorporates the global flow effects in the local calculations. This procedure can be viewed as an extension of the coupled local-global single-phase upscaling approach developed by Chen et al. (2003) [6]. However, in the two-phase upscaling, both global coarse and local fine-scale simulations are time-dependent, which poses more challenges.

Fig. 3.24 schematically illustrates the local-global two-phase upscaling procedure. A global coarse-scale flow is shown in Fig. 3.24a, and the shaded region represents a local region embedded in the global domain. Local fine-scale flow solved on the local region is presented in Fig. 3.24b. The global coarse and local fine-scale flow simulations are coupled through the local boundary conditions. Similar to the single-phase upscaling approach, the global coarse-scale solutions need to be interpolated onto the local fine-scale boundaries. In addition, the local fine-scale boundary conditions need to be updated according to the time-dependent coarse-scale solutions. We now describe in detail the interpolation and updating of the local boundary conditions.

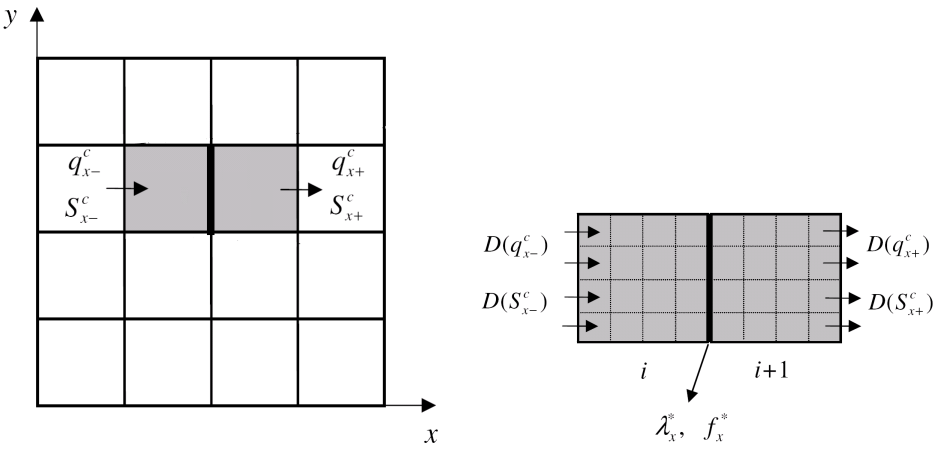

Fig. 3.24. Schematic showing local-global two-phase upscaling. The local boundary conditions of local fine-scale flow are determined from global coarse-scale solutions. Both the global coarse solutions and local boundary conditions are time-dependent.

3.3.1. Interpolation of coarse-scale solutions

The arrows in Fig. 3.24a designate coarse-scale fluxes (q^c) and saturations (S^c) obtained from the global coarse-scale simulation. They are defined at the inlet (x_-) and

outlet (x_+) edges of the local domain. These coarse-scale quantities are distributed onto the local fine-scale boundaries based on fine-scale permeability heterogeneities. There are different treatments, as presented in the previous single-phase upscaling approach [6]. In this work, the interpolation is based on time of flight (TOF) from fine-scale single-phase streamline calculations.

For the local fine-scale region shown in Fig. 3.24b, assume that it contains $n_x \times n_y$ fine-scale cells and is indexed by (i, j). At the inlet edge (x^-), the coarse-scale fluxes and saturations ($q^c_{x^-}$ and $S^c_{x^-}$) are apportioned to the local fine-scale boundaries via

$$\begin{aligned} \left(q^f_j\right)_{x^-} &= \frac{\tau_{max} - \tau_j}{\tau_{max} - \tau_{min}}|_{x^-} q^c_{x^-},\ 1 \le j \le n_y, \\ \left(S^f_j\right)_{x^-} &= \frac{\tau_{max} - \tau_j}{\tau_{max} - \tau_{min}}|_{x^-} S^c_{x^-},\ 1 \le j \le n_y, \end{aligned} \tag{3.20}$$

where the superscript c and f designate coarse and fine-scale quantities, τ_{max} and τ_{min} represent the maximum and minimum values of τ along the fine-scale boundary x^-, refers to (3.12), and j is the fine-scale index along the local boundary. Analogously, the fine-scale fluxes and saturations at the outlet boundary x^+ are obtained from q^c, S^c, and the fine-scale single-phase τ at the local boundary x^+. For the two boundaries that are parallel to the flow direction, no-flow boundary conditions are imposed.

TOF itself actually carries global transport information (for single-phase tracer flow). We note that the normalization in Eq. 3.20 localizes the values of TOF. Thus the distribution of q^c and S^c (as shown in Eq. 3.20) only depends on the local fine-scale heterogeneity. However, it should be kept in mind that the global dependency is in fact already incorporated through the direct use of global coarse solutions q^c and S^c, which vary spatially. We also note that other quantities, such as fine-scale single-phase velocities, permeabilities and inter-block transmissibilities, can also be applied to interpolate the coarse-scale fluxes and saturations, though they are not

considered here. As will be shown in Section 3.3.4, the use of TOF does provide satisfactory results.

3.3.2. Update of local boundary conditions

The global flow dependency in the two-phase upscaling exists both temporally and spatially. How to use the time-dependent global coarse solutions q^c and S^c is a challenge that was not encountered in single-phase flow upscaling calculations. To incorporate the temporal global flow information, we need to update the local boundary conditions in accordance with the coarse solutions during the course of local fine-scale simulation. A key issue lies in that the time scales involved in the global coarse and local fine-scale simulations are different. In this work, introduce a criterion, which attempts to keep the change of local fine-scale saturation (in an average sense) approximately same as that of the global coarse solution.

For a local domain, we denote the saturation on the inlet boundary as S_{bc}, and the saturation in the interior domain S_{in}. Then S_{bc} and S_{in} represent those values from the global coarse solution, and S^f_{bc} and S^f_{in} designate the integrated fine-scale saturation on the boundary and the averaged saturation in the interior region. Note that here for simplicity, we do not use $\langle\cdot\rangle$ to represent the integrated/averaged quantities. Assume that the boundary saturation is a function of the interior saturation, i.e., $S_{bc}(S_{in})$. In the local-global two-phase upscaling, the local fine-scale saturation boundary conditions are obtained from the global coarse-scale solution, which yields

$$S^f_{bc}(S^f_{in}) = S^c_{bc}(S^c_{in}) \tag{3.21}$$

Fig. 3.25 schematically displays a functional relationship between the saturation at the inlet boundary and that in the interior domain. In this work, the time-dependent global coarse saturation is represented by a series of solutions. As shown in

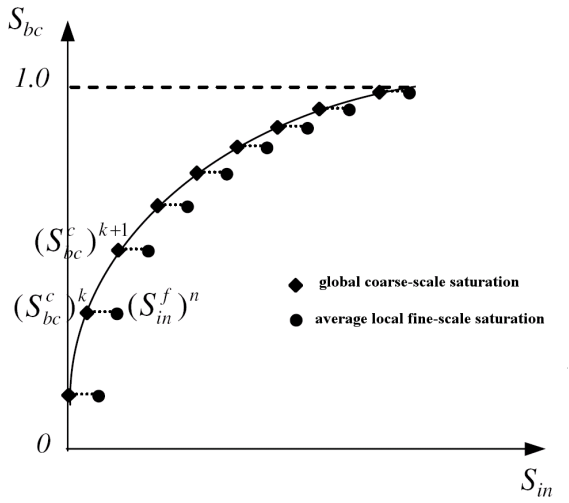

Fig. 3.25. Schematic showing the update of local boundary conditions.

Fig. 3.25, the boundary saturation from coarse-scale solution is designated as $(S_{bc}^c)^k$, where k designates a time step in the global coarse simulation, at which the coarse solution is output. The (averaged) fine-scale saturation (over a coarse block) from the local fine-scale simulation is denoted as $(S_{in}^f)^n$, where n is the time step in the local fine-scale simulation.

In the local fine-scale simulation, for a given boundary saturation $(S_{bc}^c)^k$, the interior saturation $(S_{in}^f)^n$ will increase with the advances of time step n. This is schematically illustrated by the dotted horizontal lines in Fig. 3.25. When $(S_{in}^f)^n$ reaches the value of its corresponding coarse-scale saturation at the next step $(S_{in}^c)^{k+1}$ (for the given coarse block), the boundary saturation at $k+1$, $(S_{bc}^c)^{k+1}$, will be used to determine the local fine-scale boundary conditions. Thus the criterion to update the boundary conditions can be expressed as

$$(S_{in}^f)^n \geq (S_{in}^c)^{k+1} \tag{3.22}$$

That is, when the averaged local fine-scale saturation equals the coarse-scale saturation for a given coarse block, the local boundary conditions determined by q^c and S^c (at time step k, via Eq.(3.20)) will be updated by q^c and S^c at time step $k+1$.

We note that here the global transient solution is approximated by a series of steady state solutions. Therefore, the smaller the time interval, the better the approximation is. We point out that standard local saturation boundary conditions, by contrast, considers only $S_{bc} = 1.0$. Therefore, the local fine-scale saturation $(S^f_{in})^n$ increases only along the dashed horizontal line of $S_{bc} = 1.0$. It is also found that the time interval, on which the local boundary conditions are updated, does considerably affect the flow results. In this dissertation, we consider a time interval of 0.05 PVI (on the time scale of global coarse simulation), which gives satisfactory results. In fact, it can be shown that if the time interval is small enough, this treatment implies that the change of the averaged local fine-scale saturation approximately equals to that of the global coarse saturation. From Eq. (3.21), we take derivative with respect to time t, which gives

$$\frac{dS^f_{bc}}{dS^f_{in}}\frac{dS^f_{in}}{dt} = \frac{dS^c_{bc}}{dS^c_{in}}\frac{dS^c_{in}}{dt} \tag{3.23}$$

In Fig. 3.25, we see that if the time interval is very small, we have

$$\frac{dS^f_{bc}}{dS^f_{in}} \approx \frac{dS^c_{bc}}{dS^c_{in}}, \tag{3.24}$$

then it follows that

$$\frac{dS^f_{in}}{dt} \approx \frac{dS^c_{in}}{dt} \tag{3.25}$$

This means that the change of the averaged local fine-scale saturation is approximately same as that of the coarse saturation. The updating of local boundary conditions ensures that the temporal dependency of global flow is also taken into account in the

local upscaling calculations.

3.3.3. Algorithm of local-global two-phase upscaling

The overall local-global two-phase (LG2P) upscaling algorithm can be summarized as follows. We describe the algorithm with reference to Fig. 3.24:

Algorithm 1. *Local-global two-phase (LG2P) upscaling.*

1. *Solve global coarse-scale flow with generic boundary conditions (i.e., flow in the x or y direction) to obtain time-dependent coarse-scale solutions $(q^c)^k$ and $(S^c)^k$, $k = 0, \ldots, K$, where k represents a time step on the global coarse scale, and K the end of global coarse simulation. For the initial global solution, primitive coarse models (with fine-scale λ and f) are applied.*
2. *For a time step k, distribute the global coarse-scale solution $(q^c)^k$ and $(S^c)^k$ onto the local fine-scale boundaries using Eq. 3.20 to obtain local fine-scale boundary conditions.*
3. *Solve local fine-scale flow problem subject to the local boundary conditions determined in step 2, and advance the solution with local fine-scale time step n.*
4. *For a prescribed saturation (computed by averaging the local fine-scale solution), compute the upscaled two-phase functions λ^* and f^* via Eqs. 2.21 and 2.24, and output the saturation and upscaled functions.*
5. *Compute averaged fine-scale saturation over coarse block i ($\langle S_i^f \rangle^n$) and compare it with the corresponding global coarse-scale saturation at block i ($(S_i^c)^{k+1}$).*
6. *If $\langle S_i^f \rangle^n < (S_i^c)^{k+1}$, continue on step 3.*
7. *If $\langle S_i^f \rangle^n \geq (S_i^c)^{k+1}$ (and $k < K$), update the coarse-scale solution (q^c and S^c) in step 2 with q^c and S^c from time step $k+1$, and continue with step 2.*

8. *If needed, iterate on step 1 by solving the global coarse-scale flow with the newly computed coarse-scale two-phase functions λ^* and f^*.*

The LG2P upscaling approach uses generic flows in both the x and y directions to compute the x and y components of λ^* and f^*. For the initial global coarse-scale solution, since the upscaled two-phase functions are not yet computed, we consider the primitive coarse-scale model. The coarse-scale solutions computed from the primitive model may not be the best to estimate the local boundary conditions. Therefore, after the upscaled λ^* and f^* are computed, the global coarse-scale flow can be solved again to obtain a new set of q^c and S^c, which can be expected to be more accurate than those from the primitive model. In fact, the entire procedure can be iterated on the global coarse and local fine-scale solutions, similar to the local-global single-phase upscaling approach [6]. For all the LG2P results presented in this dissertation, we applied one iteration to compute the λ^* and f^*, and observed evident improvement of the flow results compared to the case without iteration.

In the current implementation, the global coarse-scale solutions were computed prior to the local fine-scale simulations. Existing local two-phase upscaling code can be readily applied in that only the local boundary conditions need to be modified. We note that the LG2P upscaling algorithm can be implemented in a way such that the global coarse and local-fine scale simulations are performed simultaneously, though the discrepancy of time scales (described in Section 3.3.2) still needs to be resolved.

3.3.4. Numerical result

In this section, we present the numerical results of the local-global two-phase upscaling for different cases. We first consider permeability distributions with different correlation lengths, and cases with high fluid-mobility ratios and different flow bound-

ary conditions. Then the method is applied to multiple permeability realizations and the statistics of flow results are compared. The permeability distributions and flow problems considered here are as described in Section 3.1.2. For all the cases, two-dimensional systems are considered, and an upscaling ratio of 10 is applied in each dimension.

3.3.4.1. Results for different correlation lengths

The first case is a log-normal permeability distribution with correlation lengths $l_x = 0.4$ and $l_y = 0.01$, and $\sigma_{\log k} = 2$, as shown in Fig. 3.4a. In the Section 3.2.4.1, we showed the results of TOF-base two-phase upscaling, with a_1 predetermined. Here, using LG2P upscaling we get an accurate approximation without predetermined a_1, refer to Fig. 3.26. The LG2P upscaling (the dashed curves in Fig. 3.26) captures the fine-scale solutions very well for both the total flow rate and oil fractional flow predictions. Here, we don't want to compare TOF-based upscaling and LG2P upscaling. We want to show both of these methods give accurate prediction of total flow rate and oil fractional flow. Here, we still compare LG2P upscaling with primitive coarse model and local EFBC upscaling. As in Fig. 3.26, LG2P shows comparable accuracy to the global two-phase upscaling (as shown in Fig. 3.5), but with significant computational savings, as the LG2P upscaling avoids solving any global fine-scale two-phase flow. This example demonstrates the efficacy of the proposed local-global two-phase upscaling approach.

Next we consider a permeability field characterized by relatively long correlation lengths. The permeability distribution with $l_x = 0.5$ and $l_y = 0.1$ is shown in Fig. 3.4b, and the results are shown in Fig. 3.27. For this longer correlation lengths, the EFBC local upscaling (the dot-dash curve) provides a solution close to the fine-scale results (the solid curve) and primitive coarse model also gives a reasonable solution with small

error. But the LG2P upscaling further improves the results, showing very accurate predictions (the dashed curves) in Fig. 3.27. So by the results Fig. 3.26 and Fig. 3.27, we can see the local-global two-phase upscaling capture the fine-scale solutions for general cases in different parameter ranges. It is a general approach to incorporate the global dependency of both pressure and saturation.

The following cases are permeability fields characterized by very short correlation lengths in the vertical direction ($l_y = 0.02$ and $l_y = 0.01$, respectively), and the horizontal correlation lengths are also shorter than the previous two examples ($l_x = 0.2$ and $l_x = 0.25$, respectively), displayed in Fig. 3.4c and 3.4d. As we have mentioned in the Section 3.2.4.1, EFBC local two-phase upscaling lost accuracy for these two cases (and for cases with shorter correlation lengths in one direction in general, e.g., see Figs. 12 and 14 in [5]). Here the results of LG2P upscaling corrects the overestimation of total flow rate and earlier breakthrough of oil fractional flow in EFBCs, as shown in Figs. 3.28 and 3.29.

In our previous work [5], for these two cases, we applied a generalized convection-diffusion (GCD) model to improve the coarse-scale accuracy. As discussed in Chapter II, the upscaled parameters in the GCD model also requires numerical computation of local flow problems. Therefore the issue of global flow dependency also exists in the GCD model, and the local-global two-phase upscaling approach presented here will also benefit the local computations of the GCD parameters.

3.3.4.2. Results for high mobility ratio

For the results we presented so far, we considered a moderate fluid-mobility ratio ($M = 5$), which is typical in oil-water flow. The LG2P upscaling approach was also applied to cases with high mobility ratios (e.g., $M = 50$ and $M = 100$), as may be encountered in gas injections for hydrocarbon recoveries from petroleum reservoirs.

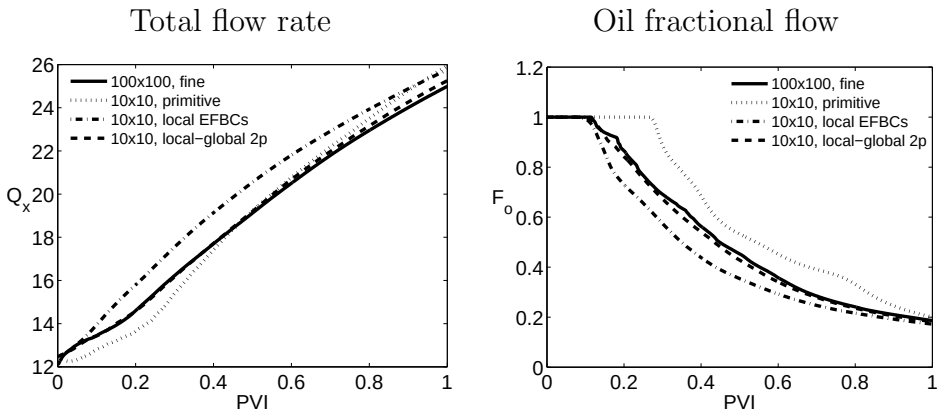

Fig. 3.26. Flow results of local-global two-phase upscaling for a log normal permeability field ($l_x = 0.4$, $l_y = 0.01$, and $\sigma = 2.0$).

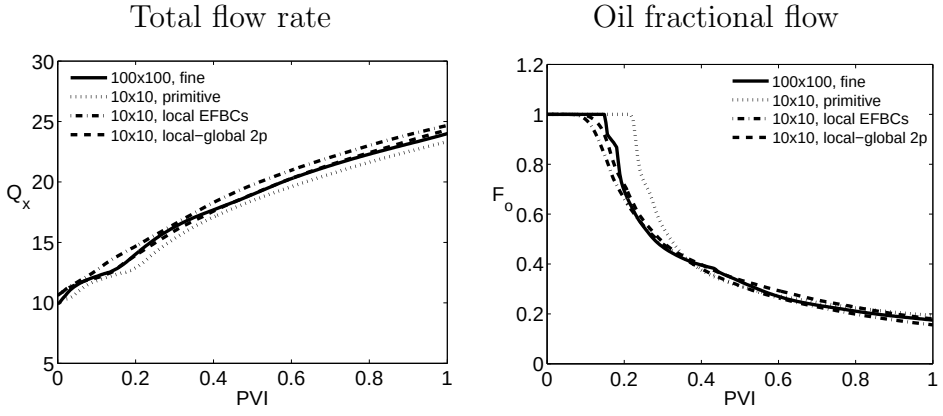

Fig. 3.27. Flow results of local-global two-phase upscaling for a log normal permeability field ($l_x = 0.5$, $l_y = 0.1$, and $\sigma = 2.0$).

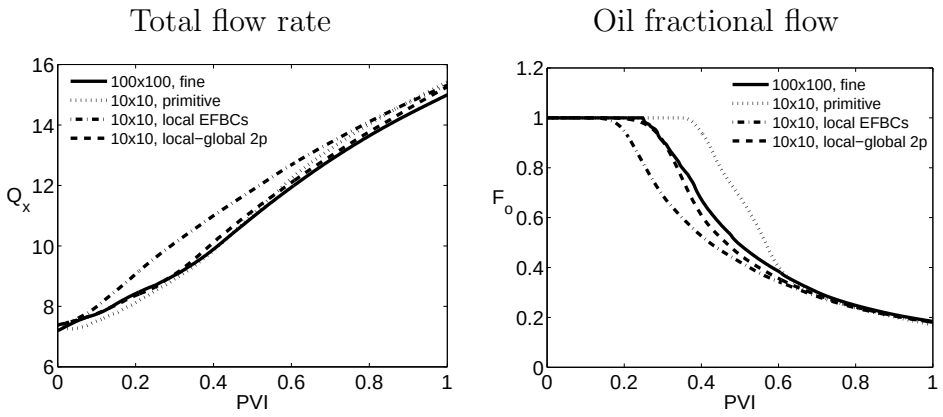

Fig. 3.28. Flow results of local-global two-phase upscaling for a log normal permeability field ($l_x = 0.2$, $l_y = 0.02$, and $\sigma = 2.0$).

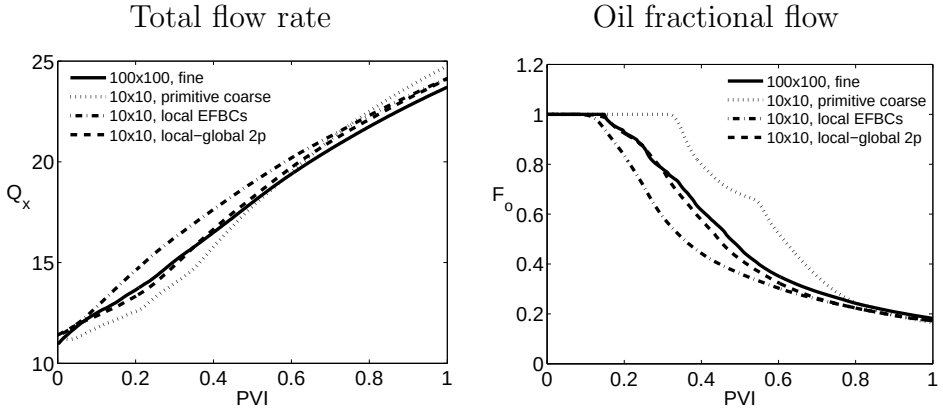

Fig. 3.29. Flow results of local-global two-phase upscaling for a log normal permeability field ($l_x = 0.25$, $l_y = 0.01$, and $\sigma = 2.0$).

We note that for the previous cases ($M = 5$), the errors associated with the primitive model mainly exist in the oil fractional flow predictions. The errors in the total flow rate are relatively small (e.g., Figs. 3.27 and 3.28). This is due to the fact that for all the cases in this work, we apply the most accurate single-phase (global transmissibility) upscaling method. And for cases with moderate mobility ratios, the accuracy of the upscaled single-phase flow parameters has a dominant impact on the accuracy of the two-phase flow results.

However, for cases with high-mobility ratios, the upscaled two-phase functions also affect considerably the results of total flow rate. In Fig. 3.30, we present the results for $M = 50$ (for the permeability field with $l_x = 0.25$, $l_y = 0.01$, shown in Fig. 3.4d). And in Fig. 3.31, the results for $M = 100$ (for $l_x = 0.4$ and $l_y = 0.01$, as shown in Fig. 3.4a) are displayed. For both cases (Figs. 3.30a and 3.31a), the accuracy of the total flow rate at PVI=0 (when the system is still of single-phase flow) is determined by the upscaled single-phase flow parameters. Then the upscaled two-phase functions act to account for the multiphase flow effects. We see that the primitive coarse model (the dotted curves in Figs. 3.30a and 3.31a) shows evident errors during the course of simulation (except for PVI=0). The LG2P upscaling (the dashed curves) consistently corrects the errors as the simulation time evolves, and shows very close predictions to the fine-scale model. It again improves the results of local EFBC two-phase upscaling (the dot-dash curves in Figs. 3.30a and 3.31a), which overestimates the total flow rate, as shown in the previous cases.

Shown in Figs. 3.30b and 3.31b are the results for oil fractional flow for the cases with $M = 50$ and $M = 100$. Compared to the previous cases, the injected fluid (water) breaks through very fast (as illustrated in the fine-scale solutions) due to the very high-mobility ratios. The primitive coarse model again shows biased predictions towards late breakthrough, though the errors are not as large as the previous cases. Both

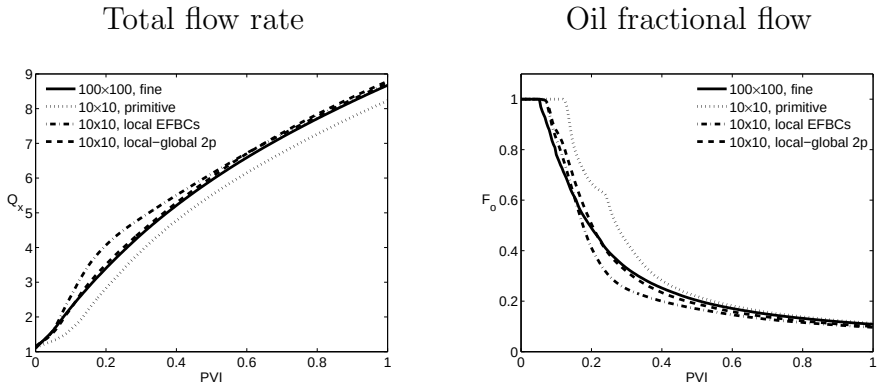

Fig. 3.30. Flow results of local-global two-phase upscaling for a log normal permeability field ($l_x = 0.25$, $l_y = 0.01$, and $\sigma = 2.0$), and $M = 50$.

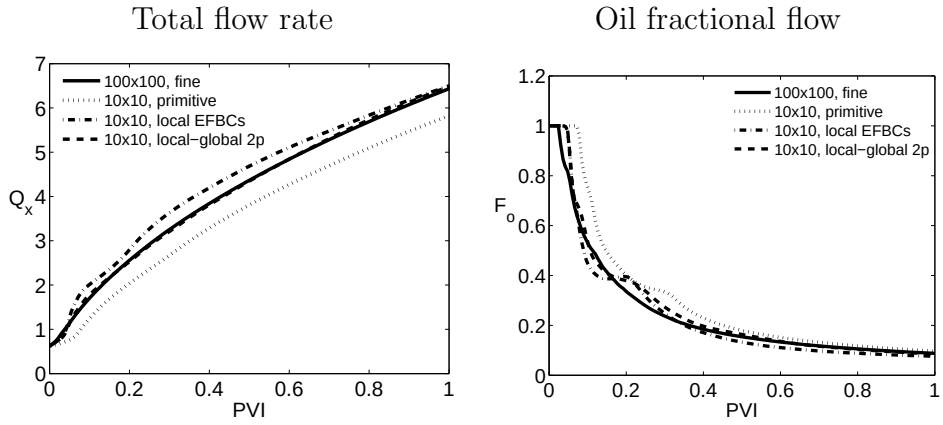

Fig. 3.31. Flow results of local-global two-phase upscaling for a log normal permeability field ($l_x = 0.4$, $l_y = 0.01$, and $\sigma = 2.0$), and $M = 100$.

EFBC local two-phase upscaling and the local-global two-phase upscaling correct the errors in the primitive model, especially capture the breakthrough time. We see that for these cases ($M = 50$ and $M = 100$), the errors associated with EFBC local upscaling are much smaller than the cases with $M = 5$. The LG2P upscaling again outperforms the EFBC local upscaling, consistently showing improvements over local methods.

3.3.4.3. Results for low mobility ratio

In this section, we present numerical results for low mobility ratio cases, i.e., M is less than 1. We limit ourselves to one representative numerical result. In Figure 3.32, we present the result for $M = 0.1$. In Figure 3.32, the local EFBC two-phase upscaling (the dot-dash curve in Figure 3.32a) shows errors during the course of the simulation. We notice that for low mobility ratio, the error of primitive coarse model is small compared to that with higher mobility ratio. In fact, the primitive coarse-scale result is close to the fine-scale simulation result. If we use local-global two-phase upscaling, it still improves the result of the primitive coarse model (the dotted curve in Figure 3.32a) as well as the local EFBC two-phase upscaling (the dash-dot curve in Figure 3.32a). The local-global two-phase upscaling (the dashed curves) consistently corrects the errors as the simulation time evolves, and shows very close predictions to the fine-scale model.

3.3.4.4. Results for changing flow conditions

We next present numerical results for different flow boundary conditions. In the reservoir simulation, if the flow boundary condition changes, the total flow and fractional flow curves will change dramatically. In this section, we will show that LG2P upscaling gives accurate prediction of total flow rate and fraction flow during the whole

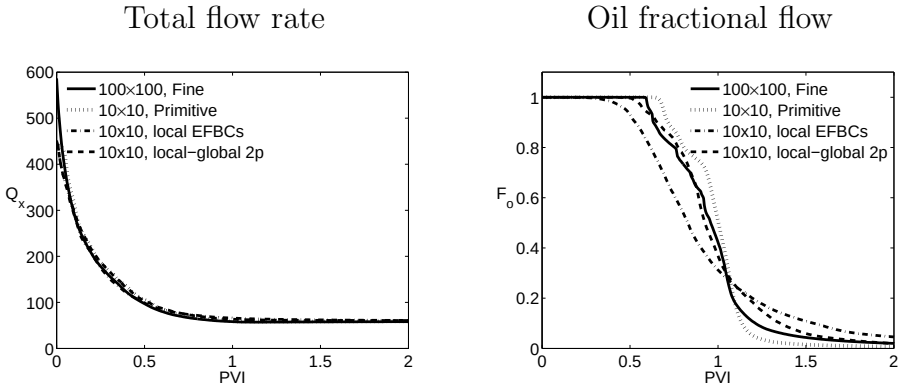

Fig. 3.32. Flow results of local-global two-phase upscaling for a log normal permeability field ($l_x = 0.4$, $l_y = 0.01$, and $\sigma = 2.0$), $M = 0.1$.

process while flow condition changes.

We consider the permeability field characterized by $l_x = 0.4$ and $l_y = 0.01$, change flow condition at PVI= 0.6. Two different flow conditions are applied, refer to Fig. 3.33. When PVI$\leq$ 0.6, the boundary condition is constant pressure-no flow condition, after that the boundary condition is changed to corner-to-corner as shown in Fig. 3.33 (a) and (b). We compared the primitive coarse model, local EFBCs with local-global two-phase upscaling. As the results shown in Fig. 3.34 and 3.34, LG2P gives the most accurate prediction of total flow rate and fractional flow. After the boundary condition changes, the error of LG2P upscaling is a little bit large. The reason is that the pseudo functions are generated by initial boundary condition and are used through out the whole process. If we generate use different pseudo functions corresponding with different boundary conditions, we might be able to get a better result. This is under investigation.

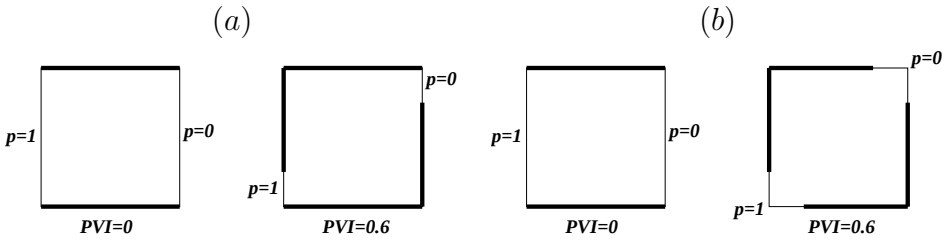

Fig. 3.33. Schematically showing different flow conditions. Flow condition is constant pressure and no flow condition from PVI=0.0 to PVI = 0.6. For PVI$\geq$ 0.6, flow condition is changed to corner-to-corner flow.

3.3.4.5. Results for multiple realizations

Our final example involves flow simulation over multiple permeability realizations, which are often required for uncertainty quantification in subsurface modeling. We consider the permeability field characterized by $l_x = 0.4$ and $l_y = 0.01$, and generate 100 realizations of the fine-scale model (unconditional to any data). The various coarse-scale models are then applied to each realization. As often applied in uncertainty quantification, the flow results are represented by ensemble statistics (i.e., P50 and P10-P90 confidence interval) of the flow predictions over 100 realizations. Here we compare the fine and coarse-scale ensemble statistics to assess the overall accuracy of a particular coarse model.

Shown in Fig. 3.36 are the fine and coarse-scale results for oil fractional flow for the 100 realizations (represented by gray curves). Fig. 3.36a shows the fine-scale predictions, while Fig. 3.36b is for the primitive coarse-scale model. We see the variations among different realizations. Of greater interest is some key statistics of the flow responses, such as the P50 and P10-P90 confidence interval. In Fig. 3.36, the solid black curves represent the P50 flow predictions, while the dashed black curves represent the P10 (lower curves) and P90 (upper curves) responses. Next we compare

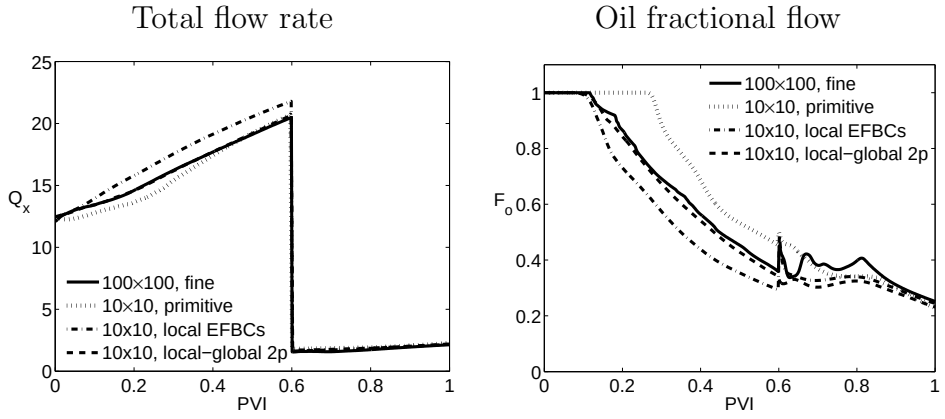

Fig. 3.34. Flow results of local-global two-phase upscaling with a changed flow condition at PVI=0.6, as (a) in Fig. 3.33. Permeability is a log normal permeability field $l_x = 0.4$, $l_y = 0.01$, and $\sigma = 2.0$, and $M = 5$.

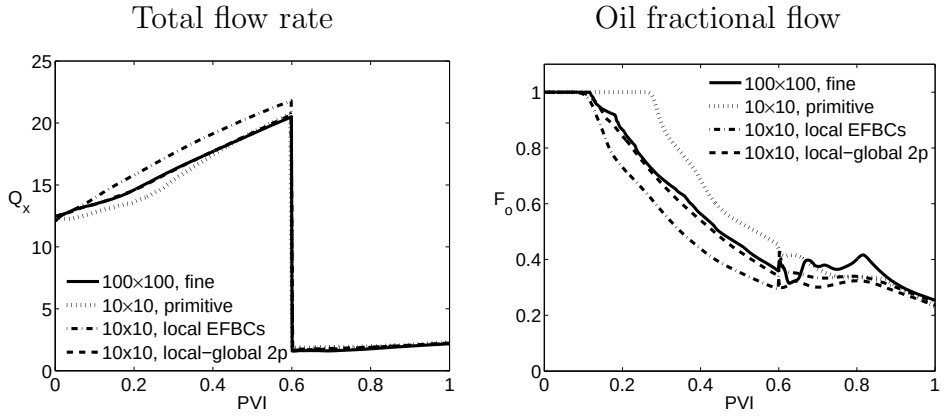

Fig. 3.35. Flow results of local-global two-phase upscaling with a changed flow condition at PVI=0.6, as (b) in Fig. 3.33. Permeability is a log normal permeability field $l_x = 0.4$, $l_y = 0.01$, and $\sigma = 2.0$, and $M = 5$.

the P50, P10 and P90 flow predictions of the fine and different coarse-scale models.

The comparisons are shown in Fig. 3.37, in which the solid curves correspond to the fine-scale results, the dot-dash curves to the coarse-scale models; and the thick curves represent P50 and the thin curves the P10 (lower curves) and P90 (upper curves) flow responses. Shown in Fig. 3.37a is the comparison between the fine and primitive coarse-scale models. It is evident that the primitive coarse model shows large errors — the P10-P90 intervals predicted by the fine and coarse models do not overlap in Fig. 3.37a.

The results for the EFBC local upscaling are shown in Fig. 3.37b. Although it considerably improves the primitive model by correcting the bias towards a late breakthrough, it is also apparent that there is a bias towards an early breakthrough and the predicted uncertainty range is much narrower than that in the fine-scale model. Here the biased results in the P50 and P10-P90 interval illustrate the biased prediction in each realization using EFBC local upscaling. The results for LG2P upscaling are shown in Fig. 3.37c. We see that it captures the fine-scale P50 and P10-P90 predictions very well. The coarse models reproduce the P50 of fine-scale solution, and capture the P10-P90 uncertainty range. This example demonstrates again the superior performance of the local-global two-phase upscaling.

Note that in other work [7], an ensemble-level upscaling approach was developed to efficiently generate the upscaled two-phase functions for multiple reservoir models. In that approach, statistical methods can be combined with any flow-based two-phase upscaling, which in fact serves as a base method. The accuracy of the underlying flow-based method will determine the accuracy of the ensemble-level upscaling. Therefore, the LG2P upscaling developed here can be applied in the context of ensemble-level upscaling to efficiently and accurately model multiple reservoir realizations.

3.3.5. Concluding remarks

A new local-global two-phase upscaling approach was developed to upscale two-phase transport functions. The method uses global coarse-scale flow solutions to determine the local boundary conditions (for both pressure and saturation equations) in the local two-phase upscaling calculations. The local boundary conditions are updated with the time-dependent coarse solutions, therefore capturing the global flow effects both spatially and temporally. Unlike global two-phase upscaling, the LG2P upscaling avoids solving any global fine-scale two-phase flow, which makes the method much more efficient. This new approach can be viewed as an extension of the previous work on a coupled local-global upscaling for single-phase flow parameters, though the issue of global dependency of saturation was not encountered in the single-phase upscaling approach.

In addition to the accuracy, another important aspect in upscaling is the computational cost associated with the upscaling computations. The computational cost of LG2P upscaling is essentially the number of iterations multiplies the cost of local two-phase upscaling. For all the results presented in this work, only one iteration is considered. That means the computational cost is doubled compared to the local two-phase upscaling. This cost is still often small compared to the full fine-scale multiphase flow simulation. The computational savings will be even more significant when flow simulations for different flow scenarios are preformed, and when the LG2P upscaling is applied in conjunction with ensemble-level upscaling approaches ([7]) to cases with multiple permeability realizations.

An important issue with any upscaling technique is the robustness of the method with respect to changing flow conditions. It is important to note that in any global upscaling methods (or local methods with global flow information incorporated), there

are two types of global flow information. The local-global procedure presented here considers generic global flow boundary conditions, i.e., global flow in the x and y directions (for a 2D system). The resultant coarse-scale properties are expected to provide reasonable accuracy for different flow scenarios, though it may not yield the most accurate coarse model for a particular flow condition. The second type of global flow addresses this issue through the use of a specific set of global boundary conditions. They can be expected to provide the best accuracy for a specific flow problem, though the upscaled properties may need to be updated when the flow conditions change dramatically.

From our limited tests, it was shown that the LG2P upscaling associated with generic global flows provides reasonable accuracy when the flow conditions change. In the context of single-phase flow upscaling, the coupled local-global ([6]) and adaptive local-global ([4]) approaches represent the use of the two different types of global flows. We note that similar to the single-phase upscaling methods, the LG2P upscaling can be extended to adjust the upscaled two-phase functions based on the actual global boundary conditions (including well-driven flows). Extensions along this line will be studied in our future work.

The current implementation of the LG2P upscaling could be modified by using different treatments to determine the local boundary conditions. In this work, only the inlet and outlet boundary conditions (for fluxes and saturations) are determined from the global coarse-scale flow based on single-phase time of flight. For the boundaries that are parallel to the flow directions, we simply impose no-flow conditions. It is possible that other procedures (e.g., the use of pressures and the interpolation of coarse solutions on all the local boundaries) as well as other interpolation schemes might provide even further improved accuracy.

3.4. Conclusion

The following main conclusions can be drawn from this chapter:

- In this chapter, we investigated the global flow dependency of upscaled two-phase functions in the coarse-scale modeling of subsurface flow and transport. We demonstrated that the global dependency of saturation has a strong impact on the upscaled transport functions. This effect is unique in the upscaling of multiphase flow, and was not effectively accounted for in existing local two-phase upscaling methods.

- A TOF (time-of-flight)-based two-phase upscaling approach was developed and implemented. In this approach, local saturation boundary conditions are time-dependent, which is constructed as a function of time and single-phase time-of-flight. The single-phase TOF can represent local saturation variations (due to permeability heterogeneity), as well as the spatial trend of global flow. A pre-determined parameter associated with time is used to represent the temporal effects of global flow. The value of this parameter depends strongly on the spatial correlation structure of fine-scale permeability. So it is possible to tune this parameter based on underlying reservoir heterogeneities, which can then be applied to a variety of permeability distributions with similar reservoir characterizations.

- We apply the TOF-based two-phase upscaling to permeability fields with various correlation lengths and fluid mobility ratios. It is shown that the use of the TOF-based two-phase upscaling can considerably improve upon existing two-phase upscaling methods (e.g., standard local boundary conditions, global flux boundary conditions, and effective flux boundary conditions), and provide

accurate coarse-scale predictions for both flow and transport. The TOF-base two-phase upscaling does not require significant extra computation compared with existing two-phase upscaling methods. It avoids solving global fine-scale two-phase flow, but effectively account for the effects of global flow.

- A new local-global two-phase upscaling approach was developed and implemented. The method uses global coarse-scale two-phase flow solutions to determine the local boundary conditions (both for pressure and saturation equations) in the local upscaling calculations. Different than the upscaling of single-phase flow parameters, the local boundary conditions need to be updated with the time-dependent coarse-scale solutions, so the global dependency in both space and time can be taken into account. The LG2P upscaling accounts for the global effects in both pressure and saturation, and avoids solving global fine-scale two-phase flow, which is required in global two-phase upscaling.

- The local-global two-phase upscaling was systematically applied to permeability fields with various correlation lengths, and its results were compared with an improved local two-phase upscaling - EFBC local two-phase upscaling. It was shown that the LG2P upscaling consistently outperforms the local methods. It corrects the bias in the local methods (i.e., overestimated total flow rate and a bias towards early breakthrough), and provides accurate coarse-scale solutions with reference to the fine-scale solution. The LG2P upscaling shows comparable accuracy to the global two-phase upscaling, but with much reduced computational cost.

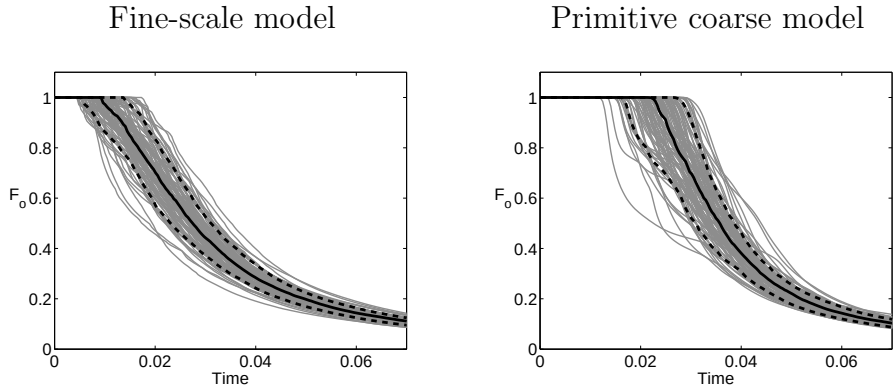

Fig. 3.36. Oil fractional flow for 100 realizations for a log normal permeability field ($l_x = 0.4$, $l_y = 0.01$, and $\sigma = 2.0$) and $M = 5$. Black curves represent P50 (solid curve) and P10-P90 interval (dashed curve).

Primitive coarse models

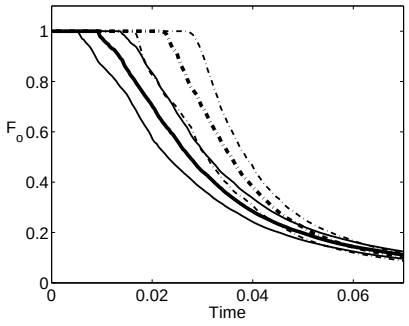

Local two-phase upscaling (EFBCs)

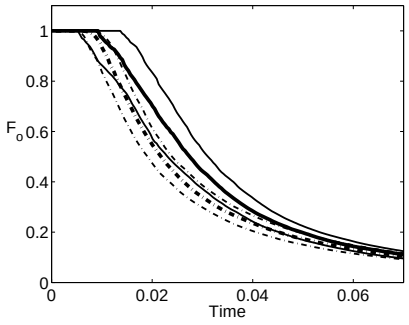

Local-global two-phase upscaling

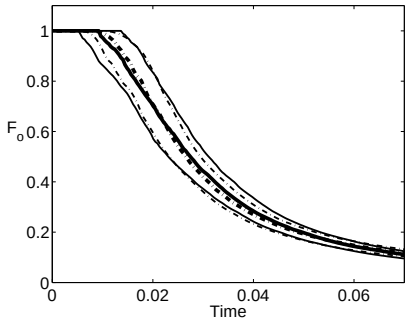

Fig. 3.37. Comparison of P50 (thick curves) and P10-P90 interval (thin curves) for oil cut between fine-scale (solid curves) and coarse-scale (dot-dash curves) models a log normal permeability field ($l_x = 0.4$, $l_y = 0.01$, and $\sigma = 2.0$) and $M = 5$.

CHAPTER IV

UPSCALING METHOD FOR TIME DEPENDENT PARABOLIC EQUATIONS

In this chapter, we present a simplified analysis for single-phase upscaling where the permeability is a time-dependent function that has both spatial and temporal scales. In particular, we choose the time scale such that the local flow problem in homogenization is time-dependent, i.e., time scales are important in upscaling. Our aim is to mimic a scenario when the mobility changes in time for pressure equation or velocity changes in time for the saturation is important.

We consider a linear parabolic equation

$$D_t w^\epsilon - div(k^\epsilon(t,x)\nabla w^\epsilon) = f(t,x) \text{ in } [0,T)\times\Omega \tag{4.1}$$

$$w^\epsilon = 0 \text{ in } [0,T)\times\partial\Omega \tag{4.2}$$

$$w^\epsilon(0,x) = g(x) \text{ in } \{0\}\times\Omega, \tag{4.3}$$

where w^ϵ is a quantity of interest (e.g. pressure of saturation). Here $k^\epsilon(t,x) = k(\frac{t}{\epsilon^2}, \frac{x}{\epsilon})$ is a symmetric positive and definite matrix in $[0,T)\times\Omega$ and $f \in L^2(0,T;H^{-1}(\Omega))$. We also assume that $\lambda|\xi|^2 \leq \xi^T k^\epsilon \xi \leq \Lambda|\xi|^2$ for all $\xi \in \mathbb{R}^d$. Let Γ be the periodicity of time variable t and Y be the periodicity of space variable x. Setting $\tau = \frac{t}{\epsilon^2}$ and $y = \frac{x}{\epsilon}$, we define N^j to be $\Gamma\times Y$ periodic solution of the following equation:

$$D_\tau N^j - div_y((k(\tau,y)\nabla_y(N^j - y_j))) = 0 \tag{4.4}$$

Using the formal asymptotic expansion, we have the corresponding homogeniza-

tion equation:

$$D_t w_0 - div(k^* \nabla w_0) = f(t,x) \text{ in } [0,T) \times \Omega \tag{4.5}$$

$$w_0 = 0 \text{ in } [0,T) \times \partial\Omega \tag{4.6}$$

$$w_0(0,x) = g(x) \text{ in } \{0\} \times \Omega \tag{4.7}$$

where $k^* = \langle k(I - \nabla_y N) \rangle_{\Gamma \times Y}$ and it is a symmetric positive definite constant matrix. Let w^ϵ have the expansion like

$$w^\epsilon = w_0(t,x) + \epsilon w_1(t,x,\tau,y) + \epsilon\theta_\epsilon + O(\epsilon^2),$$

where $w_1 = -N^j(\tau,y)\frac{\partial w_0}{\partial x_j}$. If we ignore the term $O(\epsilon^2)$, then the boundary corrector θ_ϵ satisfies the equation

$$D_t\theta_\epsilon - div(k^\epsilon \nabla\theta_\epsilon) = \frac{1}{\epsilon}[D_t(w^\epsilon - w_0 - \epsilon w_1) - div(k^\epsilon(w^\epsilon - w_0 - \epsilon w_1))] \text{ in } [0,T) \times \Omega \tag{4.8}$$

$$\theta_\epsilon = -N^j \frac{\partial w_0}{\partial x_j} \text{ in } [0,T) \times \partial\Omega \tag{4.9}$$

$$\theta_\epsilon(0,x) = -N^j(0,y)\frac{\partial w_0}{\partial x_j} \text{ in } \{0\} \times \Omega \tag{4.10}$$

It is known that: (1) $w_\epsilon \rightharpoonup w_0$ weakly in $L^2(0,T;H_0^1(\Omega))$; (2) $k^\epsilon \nabla w_\epsilon \rightharpoonup k^* \nabla w_0$ weakly in $[L^2(\Omega)]^d$.

4.1. Time-Space Upscaling Procedure

In this section we are going to study single-phase upscaling for permeability with spatial and time variables. To get the effective permeability matrix $\tilde{k}$, we need to

solve the local problems in each coarse block V.

$$D_t\phi_i^\epsilon - div(k^\epsilon \nabla \phi_i^\epsilon) = 0 \text{ in } [0,T) \times V \tag{4.11}$$

$$\phi_i^\epsilon = x_i \text{ on } [0,T) \times \partial V \tag{4.12}$$

$$\phi_i^\epsilon = x_i \text{ in } \{0\} \times V, \tag{4.13}$$

where $i = 1, 2, ..., d$. The associated homogenized equation is

$$D_t\phi_i - div(k^* \nabla \phi_i) = 0 \text{ in } [0,T) \times V \tag{4.14}$$

$$\phi_i = x_i \text{ on } [0,T) \times \partial V \tag{4.15}$$

$$\phi_i = x_i \text{ in } \{0\} \times V. \tag{4.16}$$

From the above equations, we know that $\phi_i = \phi_i(x)$ is a linear function only depending on x not on t. As for the boundary corrector θ_i^ϵ, a direct calculation gives rise to

$$\begin{aligned}
D_t\theta_i^\epsilon - div(k^\epsilon \nabla \theta_i^\epsilon) &= \frac{1}{\epsilon}[D_t(\phi_i^\epsilon - \phi_i + \epsilon N^j \frac{\partial \phi_i}{\partial x_j}) - div(k^\epsilon \nabla(\phi_i^\epsilon - \phi_i + \epsilon N^j \frac{\partial \phi_i}{\partial x_j}))] \\
&= -\frac{1}{\epsilon}[-div(k^\epsilon \nabla \phi_i) + \epsilon \nabla \phi_i \cdot D_t N + \epsilon(div(k^\epsilon \nabla N)) \cdot \nabla \phi_i] \\
&- div(k^\epsilon N(\nabla : \nabla \phi_i)) \\
&= -\frac{1}{\epsilon}[D_t N - div(k^\epsilon (I - \epsilon \nabla N))] \nabla \phi_i \\
&= -\frac{1}{\epsilon^2}[D_\tau N - div_y(k(I - \nabla_y N))] \nabla \phi_i \\
&= 0.
\end{aligned}$$

Therefore, the boundary corrector θ_i^ϵ in each coarse block satisfies the following equation

$$D_t\theta_i^\epsilon - div(k^\epsilon \nabla \theta_i^\epsilon) = 0 \text{ in } [0,T)\times V \tag{4.17}$$

$$\theta_i^\epsilon = -N(t,\frac{x}{\epsilon})e_i \text{ on } [0,T)\times \partial V \tag{4.18}$$

$$\theta_i^\epsilon = -N(0,\frac{x}{\epsilon})e_i \text{ in } \{0\}\times V. \tag{4.19}$$

Now we want to estimate θ_i^ϵ. Applying the regularity estimation of parabolic equation, we have

$$\|\theta_i^\epsilon\|_{L^2(0,T;H^1(\Omega)} \leq C(\|N(0,\frac{x}{\epsilon})e_i\|_0 + \|N(\frac{t}{\epsilon^2},\frac{x}{\epsilon})\|_{H^{0,\frac{1}{2}}(\Sigma)}). \tag{4.20}$$

We assume that $diam(V) = h$, $T = \Delta t$. One can show that

$$\begin{aligned}\|N(\frac{t}{\epsilon^2},\frac{x}{\epsilon})\|_{H^{0,\frac{1}{2}}(\Sigma)} &\leq C\|N(\frac{t}{\epsilon^2},\frac{x}{\epsilon})\|^{\frac{1}{2}}_{H^{0,0}(\Sigma)}\|N(\frac{t}{\epsilon^2},\frac{x}{\epsilon})\|^{\frac{1}{2}}_{H^{0,1}(\Sigma)}\\ &\leq C(\Delta t)^{\frac{1}{2}}h^{\frac{d-1}{2}}\epsilon^{-\frac{1}{2}},\end{aligned}$$

where Σ is the boundary of the set $[0,T)\times V$. Also we have

$$\|N(0,\frac{x}{\epsilon})\|_0 \leq Ch^{\frac{d}{2}}. \tag{4.21}$$

Noticing that $h \gg \epsilon$ and $\Delta t \gg \epsilon$, we obtain

$$\|\theta_i^\epsilon\|_{L^2(0,T;H^1(\Omega)} \leq C(\Delta t)^{\frac{1}{2}}h^{\frac{d-1}{2}}\epsilon^{-\frac{1}{2}}. \tag{4.22}$$

Let $I_t = [t_i, t_e)$ be the coarse time-interval with $diam(I_t) = \Delta t$. In this dissertation, we define the upscaled effective permeability matrix $\tilde{k}$ satisfying $\langle\nabla\phi_i^\epsilon\rangle_{I_t\times V}\tilde{k}\langle\nabla\phi_j^\epsilon\rangle_{I_t\times V} = \langle\nabla\phi_i^\epsilon k^\epsilon\nabla\phi_j^\epsilon\rangle_{I_t\times V}$ in each coarse block $I_t\times V$. A direct calculation gives $\langle\nabla\phi_i^\epsilon\rangle_{I_t\times V} = e_i$ for any $i = 1\cdots d$. Consequently we have

$$\tilde{k}_{ij} = \langle\nabla\phi_i^\epsilon k^\epsilon\nabla\phi_j^\epsilon\rangle_{I_t\times V}. \tag{4.23}$$

One of the main problem in the upscaling is to estimate the difference $|\tilde{k}_{ij} - k^*_{ij}|$. In the following we focus on this estimate.

Let $E(\tau, y) = I - \nabla_y N(\tau, y)$, where $N = (N^1, N^2, \cdots, N^d)$ satisfying the following equation

$$D_\tau N + div(k^\epsilon E) = 0. \tag{4.24}$$

We obtain $k^* =< E^T k E >_{\Gamma \times Y}$ and $\nabla \phi_i^\epsilon = E \nabla \phi_i + \epsilon \nabla \theta_i^\epsilon$. Therefore, using the above equations, we get

$$\begin{aligned}
\tilde{k}_{ij} &= \langle (E\nabla\phi_i + \epsilon\nabla\theta_i^\epsilon) \cdot k^\epsilon (E\nabla\phi_j + \epsilon\nabla\theta_j^\epsilon) \rangle_{\Delta t \times V} \\
&= \langle (E\nabla\phi_i) \cdot k^\epsilon (E\nabla\phi_j) \rangle_{\Delta t \times V} + 2\epsilon \langle \nabla\theta_i^\epsilon \cdot k^\epsilon (E\nabla\phi_j) \rangle_{\Delta t \times V} + \epsilon^2 \langle \nabla\theta_i^\epsilon \cdot k^\epsilon \nabla\theta_j^\epsilon \rangle_{\Delta t \times V} \\
&= I + II + III.
\end{aligned}$$

Since k^ϵ is bounded, using (4.22) one can easily obtain that

$$III = O(\frac{\epsilon}{h}). \tag{4.25}$$

Applying Cauchy-Schwartz inequality to the term II and using (4.22) we obtain

$$II = O(\sqrt{\frac{\epsilon}{h}}). \tag{4.26}$$

Hence we have $|\tilde{k}_{ij} - \langle (E\nabla\phi_i) \cdot k^\epsilon (E\nabla\phi_j) \rangle_{\Delta t \times V}| = O(\sqrt{\frac{\epsilon}{h}})$. To finish the estimation $|\tilde{k}_{ij} - k^*_{ij}|$, we need the following lemma:

Lemma 4.1.1. *Let $I \times D$ be a unit cylinder in $\mathbb{R} \times \mathbb{R}^d$ and $G(\tau, y)$ be $I \times D$-periodic function. Suppose that $I_t \times V \in R \times R^d$ and $diam(I_t) = \Delta t$ and $diam(V) = h$. Then for all $f(t, x) \in L^\infty(I_t \times V)$, we have*

$$|\int_{I_t \times V} f(t,x) G(\frac{t}{\epsilon^2}, \frac{x}{\epsilon}) dt dx - \int_{I_t \times V} f(t,x) \langle G \rangle_{I \times D}| = O(\epsilon^2 h^d + \epsilon h^{d-1} \Delta t).$$

Proof. Let $I_i \times Y_i$ be the periodic cell of G and $I_i \times Y_i \subset I_t \times V$. Assuming $\langle G \rangle_{I \times D} = 0$, we have

$$\begin{aligned} |\int_{I_t \times V} f(t,x) G(\frac{t}{\epsilon^2}, \frac{x}{\epsilon}) dt dx| &\leq C \|f\|_{L^\infty(I_t \times V)} | \int_{\cup(I_i \times Y_i))} G dx + \int_{I_t \times V - \cup(I_i \times Y_i)} G dt dx| \\ &\leq C\epsilon^2 h^d + \epsilon h^{d-1} \Delta t. \end{aligned}$$

□

We return to the estimation $|\tilde{k}_{ij} - k^*_{ij}|$. Applying Lemma 4.1.1, we have

$$\begin{aligned} < (E\nabla\phi_i) \cdot k^\epsilon (E\nabla\phi_j) >_{\Delta t \times V} &=< \nabla\phi_i \cdot (E^T k^\epsilon E) \nabla\phi_j >_{\Delta t \times V} \\ &=< \nabla\phi_i \cdot k^* \nabla\phi_j >_{\Delta t \times V} + O(\frac{\epsilon^2}{\Delta t} + \frac{\epsilon}{h}) \\ &= k^*_{ij} + O(\frac{\epsilon^2}{\Delta t} + \frac{\epsilon}{h}). \end{aligned}$$

So we get the following theorem.

Theorem 4.1.2. *Let $\tilde{k}$ and k^* be the up-scaling matrix and homogenized matrix respectively, then*

$$|\tilde{k}_{ij} - k^*_{ij}| = O(\sqrt{\frac{\epsilon}{h}} + \frac{\epsilon^2}{\Delta t}).$$

CHAPTER V

ENSEMBLE LEVEL FLOW UPSCALING

Ensemble level upscaling is the upscaling for multiple realizations. In this chapter we propose a perturbation approach to compute the upscaled absolute permeability. In this approach, the solution of a local flow simulation is represented by a product of Green's function and a source term. In the stochastic space, the collocation technique is used to generate Green's function for a random realization. Combining the perturbation approach and collocation technique, we can compute the upscaled permeabilities rapidly for all the realizations.

5.1. Stochastic Subsurface Properties

The media properties often contain uncertainties. These uncertainties are usually parameterized and one has to deal with a large set of permeability fields(realizations). This brings an additional challenge to the fine-scale simulation and necessitates the use of of coarse-scale upscaling models. Assume that the media properties are random and denoted by $k(x, \omega)$, where ω refers to a realization. The solution of flow equation is given by $p(x, \omega)$ for each realization ω.

One of the commonly used stochastic descriptions of spatial fields is based on two-point correlation function of log-permeability. To describe it, we denote by $Y(x, \omega) = \log[k(x, \omega)]$. For permeability fields described with two-point correlation function, it is assumed that covariance function $R(x, y) = E[Y(x, \omega)Y(y, \omega)]$ is known, where $E[\cdot]$ refers to the expectation (i.e., average over all realizations) and x, y are points in the spatial domain.

For permeability fields described by two-point correlation function, one can use the Karhunen-Loève expansion (KLE) [27, 36] to obtain permeability field description

with possibly fewer degrees of freedom. This is done by representing the permeability field in terms of an optimal L^2 basis. By truncating the expansion, we can represent the permeability matrix by a small number of random parameters.

We briefly recall some properties of the KLE. For simplicity, for simplicity, we assume that $E[Y(x,\omega)] = 0$. Suppose $Y(x,\omega)$ is a second order stochastic process with $E\int_\Omega Y^2(x,\omega)dx < \infty$. Given an orthonormal basis $\{\Phi_i\}$ in $L^2(\Omega)$, we can expand $Y(x,\omega)$ as a general Fourier series

$$Y(x,\omega) = \sum_{i=1}^{\infty} Y_i(\omega)\Phi_i(x), \qquad Y_i(\omega) = \int_\Omega Y(x,\omega)\Phi_i(x)dx.$$

We are interested in the special L^2 basis $\{\Phi_i\}$ which makes the random variables Y_i uncorrelated. That is, $E(Y_iY_j) = 0$ for all $i \neq j$. The basis functions $\{\Phi_i\}$ satisfy

$$E[Y_iY_j] = \int_\Omega \Phi_i(x)dx \int_\Omega R(x,y)\Phi_j(y)dy = 0, \qquad i \neq j.$$

Since $\{\Phi_i\}$ is a complete basis in $L^2(\Omega)$, it follows that $\Phi_i(x)$ are eigenfunctions of $R(x,y)$:

$$\int_\Omega R(x,y)\Phi_i(y)dy = \lambda_i\Phi_i(x), \qquad i = 1, 2, \ldots, \tag{5.1}$$

where $\lambda_i = E[Y_i^2] > 0$. Furthermore, we have

$$R(x,y) = \sum_{i=1}^{\infty} \lambda_i\Phi_i(x)\Phi_i(y). \tag{5.2}$$

Denote $\theta_i = Y_i/\sqrt{\lambda_i}$, then θ_i satisfy $E(\theta_i) = 0$ and $E(\theta_i\theta_j) = \delta_{ij}$. It follows that

$$Y(x,\omega) = \sum_{i=1}^{\infty} \sqrt{\lambda_i}\theta_i(\omega)\Phi_i(x), \tag{5.3}$$

where Φ_i and λ_i satisfy (5.1). We assume that the eigenvalues λ_i are ordered as $\lambda_1 \geq \lambda_2 \geq \ldots$. The expansion (5.3) is called the Karhunen-Loève expansion.

In the KLE (5.3), the L^2 basis functions $\Phi_i(x)$ are deterministic and resolve the spatial dependence of the permeability field. The randomness is represented by the scalar random variables θ_i. After we discretize the domain Ω by a rectangular mesh, the continuous KLE (5.3) is reduced to finite terms and $\Phi_i(x)$ are discrete fields. Generally, we only need to keep the leading order terms (quantified by the magnitude of λ_i) and still capture most of the energy of the stochastic process $Y(x,\omega)$. For an m-term KLE approximation $Y_m = \sum_{i=1}^{m} \sqrt{\lambda_i}\theta_i\Phi_i$, define the energy ratio of the approximation as

$$e(m) := \frac{E\|Y_m\|^2}{E\|Y\|^2} = \frac{\sum_{i=1}^{m}\lambda_i}{\sum_{i=1}^{\infty}\lambda_i}. \tag{5.4}$$

If $\lambda_i, i = 1, 2, \ldots$ decay very fast, then the truncated KLE would be a good approximation of the stochastic process in the L^2 sense.

Suppose the permeability field $k(x,\omega)$ is a log-normal homogeneous stochastic process, then $Y(x,\omega) = \log(k(x,\omega))$ is a Gaussian process, and θ_i are independent standard Gaussian random variables. In this case, the covariance function of $Y(x,\omega)$ has the form

$$R(x,y) = \sigma^2 \exp\Big(-\frac{|x_1 - y_1|^2}{2l_1^2} - \frac{|x_2 - y_2|^2}{2l_2^2}\Big). \tag{5.5}$$

In the above formula, l_1 and l_2 are the correlation lengths in each dimension, and $\sigma^2 = E(Y^2)$ is the variance. We first solve the eigenvalue problem (5.1) numerically on the rectangular mesh and obtain the eigenpairs $\{\lambda_i, \Phi_i\}$. We put 4 points per correlation length in our numerical simulations. Since the eigenvalues decay fast, in this case the truncated KLE approximates the stochastic process $Y(x,\omega)$ fairly well in the L^2 sense. Therefore, we can sample $Y(x,\omega)$ from the truncated KLE (5.3) by generating Gaussian random variables θ_i.

If the permeability field $k(x,\omega)$ is a log-exponential homogeneous stochastic process,

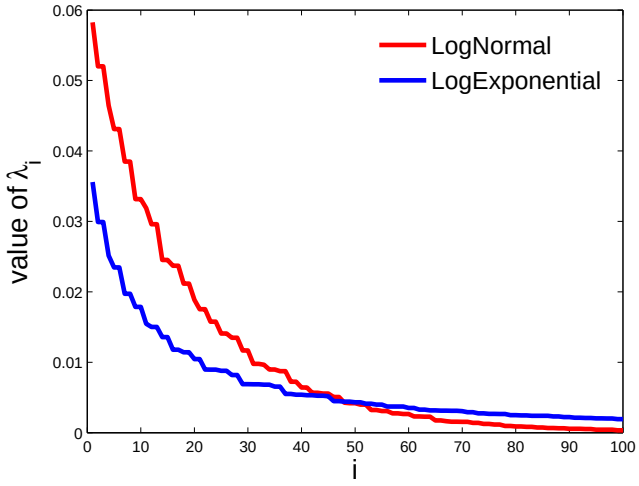

Fig. 5.1. An illustration of eigenvalues Distribution.

then the covariance function of $Y(x,\omega)$ has the form

$$R(x,y) = \sigma^2 \exp\left(-\frac{|x_1 - y_1|}{l_1} - \frac{|x_2 - y_2|}{l_2}\right). \tag{5.6}$$

In this work, we will mainly consider the above two types of permeability fields. Now we show the eigenvalues and eigenvectors for log-normal permeability field described by (5.5), with $l_1 = 0.1$, $l_2 = 0.1$, $N_{fine} = 50$. In Fig. 5.2, we plot 4 eigenvectors corresponding to eigenvalues 1, 10, 50 and 100. In Fig. 5.1, we plot eigenvalues for log-normal permeability field described by (5.5) as well as log-exponential permeability (5.6). As we see from these figures that the eigenvalues decay fast for log-normal permeability fields compared to log-exponential permeability fields. The eigenvectors corresponding to smaller (in value) eigenvalues contain finer scale features of the media. Moreover, if we denote the amplitute of eigenvector as $A_i := \max_x\{\Phi_i(x)\}$, then we can observe that A_i decreases as eigenvalue λ_i decreases as in Fig. 5.3. This is because $\|\Phi\|_{L^2} = 1$ and Φs become more ossilative as i increases.

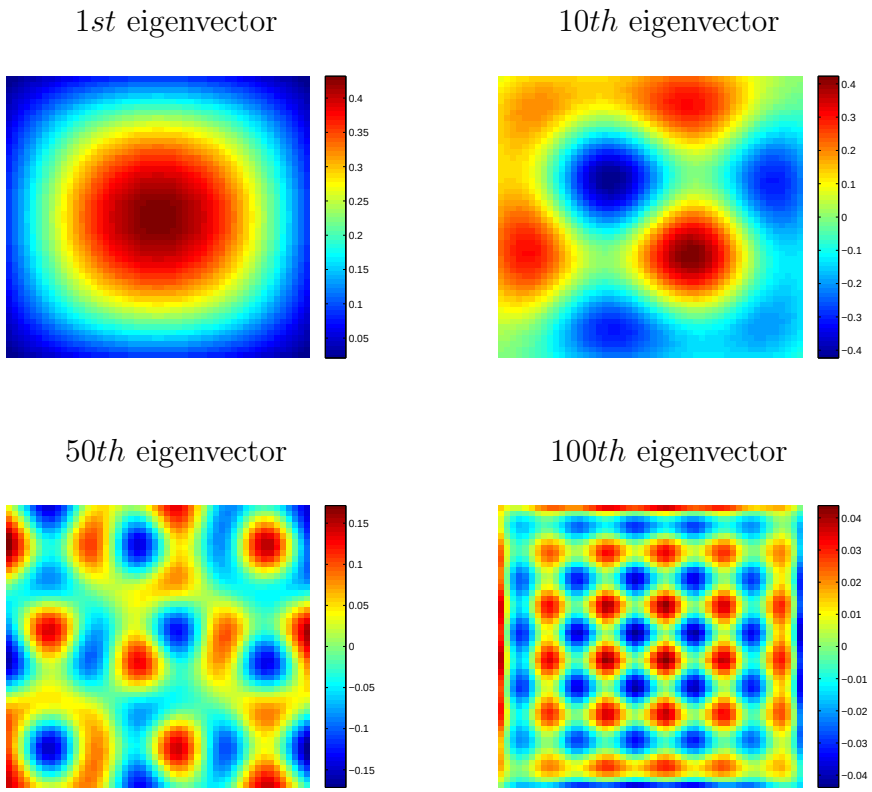

Fig. 5.2. Schematic showing the eigenvectors of a log-normal permeability field, with $l_x = 0.1$, $l_y = 0.1$, and $\sigma = 2.0$.

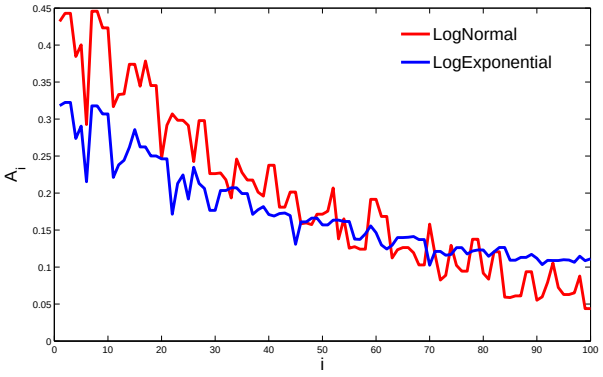

Fig. 5.3. An illustration of amplitudes distribution.

5.2. A Perturbation Approach

5.2.1. Truncated permeability

As we know permeability $k(x)$ is given by KLE of θ (5.3). In applications, the permeability fields are defined on a discrete grid. In this case, the continuous KLE (5.3) is reduced to finite N terms, N is the total number of grid blocks in the domain, and the stochastic variable θ is in $N-$dimensional uncertainty space, $\theta = (\theta_1, \theta_2, ..., \theta_N) \in \mathbb{R}^N$, the permeability $k(x)$ is

$$k(x) = \exp(Y_N) = \exp(\sum_{i=1}^{N} \sqrt{\lambda_i}\theta_i\Phi_i(x)). \tag{5.7}$$

Now we introduce a truncated KLE, which approximates permeability k with fewer terms in (5.7). The eigenvalues $\lambda_i,\ i = 1, 2, \cdots, N$ decay to zero rapidly (as in Fig. 5.1), so we use the first m largest eigenvalues in the truncated KLE. Take a $m \leq N$, let $\theta_0 = (\theta_1, \theta_2, ..., \theta_m, 0, 0, ...0) \in \mathbb{R}^N$, the truncated permeability $k_0(x)$ is given by KLE of θ_0

$$k_0(x) = \exp(Y_m) = \exp(\sum_{i=1}^{m} \sqrt{\lambda_i}\theta_i\Phi_i(x)). \tag{5.8}$$

It follows that k_0 is an approximation of k.

Now we study the upscaled truncated permeability $k_0^*(x)$. We solve a single-phase flow problem with truncated permeability k_0 on the local domain Ω,

$$div(k_0\nabla\phi_e^0) = 0 \text{ in } \Omega. \tag{5.9}$$

Boundary condition is $\phi_e^0(x) = x \cdot e$ on $\partial\Omega$, where e is a unit vector, Ω is a coarse grid block. The truncated upscaled effective permeability on Ω is computed as

$$k_0^* e = \frac{1}{|\Omega|}\int_\Omega k\nabla\phi_e^0 dx. \tag{5.10}$$

Table 5.1. Error of $\frac{\|k^*-k_0^*\|}{\|k^*\|}$ base on 100 realizations of log-exponential permeability fields, with correlation lengths $l_x = 0.1$, $l_y = 0.1$ and variance $\sigma = 2.0$.

m	e(m)	$\frac{\|k^*-k_0^*\|}{\|k^*\|}$
10	23%	0.180007
50	54%	0.084668
100	68%	0.051392
300	86%	0.016983
600	95%	0.005556

k_0^* is an approximation to k^*.

In Table 5.1, we show results of upscaled truncated permeabilities for 100 realizations. On domain $\Omega = [0,1] \times [0,1]$, we consider a log-exponential permeability field k with the correlation lengths $l_x = 0.1$, $l_y = 0.1$, the covariance $\sigma = 2.0$. Taking fine grid as $N_x^f = N_y^f = 41$ and coarse grid as $N_x^c = N_y^c = 1$, then the total number of fine grid blocks is $N = 1681$. For 100 realizations, we compute the upscaled truncated permeability k_0^*. In Table 5.1, the number of truncated terms, the corresponding energy ratio and the mean value of relative error $\frac{\|k^*-k_0^*\|}{\|k^*\|}$ based on 100 realizations is illustrated. When energy ratio is large, the upscaled truncated permeability is accurate. For example, when the energy ratio $e(m) = 95\%$, the error is $\frac{\|k^*-k_0^*\|}{\|k^*\|} = 0.5\%$; for $e(m) = 68\%$, the error is $\frac{\|k^*-k_0^*\|}{\|k^*\|} = 5\%$. But if $m \leq 50$ or less, the error becomes large $\geq 10\%$. It might be asked that if it is possible to make a correction on the truncated upscaled permeability such that for smaller m, the error is small, e.g. $\leq 5\%$. In the following parts, we will introduce a correction scheme, which gives an accurate upscaled permeability in lower dimensional space, e.g. $m \leq 50$.

5.2.2. Correction scheme

For $m \leq N$, the permeability k and the solution ϕ_e can be written into two parts, the lower order part and the perturbation part:

$$k = k_0 + k', \qquad \phi_e = \phi_e^0 + \phi_e', \tag{5.11}$$

where, the lower order part of permeability is k_0,

$$k_0(x) = \exp(\sum_{i=1}^{m} \sqrt{\lambda_i}\theta_i\Phi_i(x)), \tag{5.12}$$

and the perturbation part is $k' = k - k_0 = k_0(\exp(\log k - \log k_0) - 1)$, i.e.,

$$k' = k_0[\exp(\sum_{i=m+1}^{N} \sqrt{\lambda_i}\theta_i\phi_i) - 1] \ . \tag{5.13}$$

For $\phi_e(x)$, the lower order part is $\phi_e^0(x)$, that is the solution of (5.9). The perturbation part is $\phi_e'(x) = \phi_e(x) - \phi_e^0(x)$.

With the above notation, the single-phase flow equation can be written as

$$div((k_0 + k')\nabla(\phi_e^0 + \phi_e')) = 0 \text{ in } \Omega \ . \tag{5.14}$$

It follows that

$$\begin{aligned} div((k_0 + k')\nabla(\phi_e^0 + \phi_e')) &= div(k_0\nabla\phi_e^0) + div(k_0\nabla\phi_e') \\ &+ div(k'\nabla\phi_e^0) + div(k'\nabla\phi_e') \ . \end{aligned}$$

Neglecting the higher order term $k'\nabla\phi_e'$, then we obtain

$$div(k_0\nabla\phi_e^0) + div(k_0\nabla\phi_e') + div(k'\nabla\phi_e^0) \approx 0 \ . \tag{5.15}$$

m	e(m)	$\frac{\|k^*-k_0^*\|}{\|k^*\|}$	$\frac{\|k^*-\tilde{k}^*\|}{\|k^*\|}$
2	11%	0.283463	0.188595
5	24%	0.236421	0.119825
10	42%	0.180092	0.077604
30	79%	0.055768	0.013354
60	95%	0.012932	0.002109

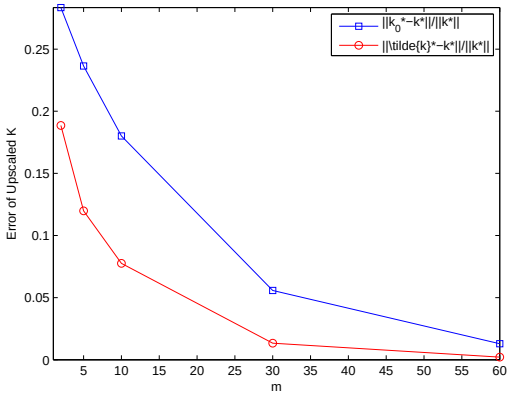

Fig. 5.4. Errors of $\frac{\|k^*-k_0^*\|}{\|k^*\|}$ and $\frac{\|k^*-\tilde{k}^*\|}{\|k^*\|}$ based on 100 realizations of log-normal permeability fields, with correlation lengths $l_x = 0.1$, $l_y = 0.1$ and the variance $\sigma = 2.0$.

Denote the corrected solution as $\tilde{\phi}_e$, the corrected single-phase flow system is

$$div(k_0\nabla\tilde{\phi}_e) = -div(k'\nabla\phi_e^0) \quad x \in \ \Omega\ . \tag{5.16}$$

Here, $\tilde{\phi}_e(x)$ satisfies same boundary condition as $\phi_e(x)$. We call $\tilde{\phi}_e(x)$ the corrected single-phase flow solution, and define the corrected upscaled effective permeability as

$$\tilde{k}^*e = \frac{1}{|\Omega|}\int_\Omega k\nabla\tilde{\phi}_e dx. \tag{5.17}$$

Comparing (5.9) and (5.15), we observe that in (5.9) there are two terms missing, $div(k_0\nabla\phi_e')$ and $div(k'\nabla\phi_e^0)$, so $\tilde{k}^*$ is a correction of k_0^*.

For the same 100 realizations in Section 5.2.1, we compare the upscaled corrected permeability $\tilde{k}^*$ and upscaled truncated permeability k_0^* in Figure 5.4. The error of the corrected upscaled permeability $\dfrac{\|k^*-\tilde{k}^*\|}{\|k^*\|}$ is much smaller than the error of truncated upscaled permeability $\dfrac{\|k^*-k_0^*\|}{\|k^*\|}$. The same trend is shown in Figure 5.5, where the permeability fields are generated by an exponential covariance function (5.6) but with the same coefficients as in Figure 5.4.

m	e(m)	$\frac{\|k^*-k_0^*\|}{\|k^*\|}$	$\frac{\|k^*-\tilde{k}^*\|}{\|k^*\|}$
10	23%	0.180007	0.087122
50	54%	0.084668	0.022694
100	68%	0.051392	0.010665
300	86%	0.016983	0.001884
600	95%	0.005556	4.7369e-04

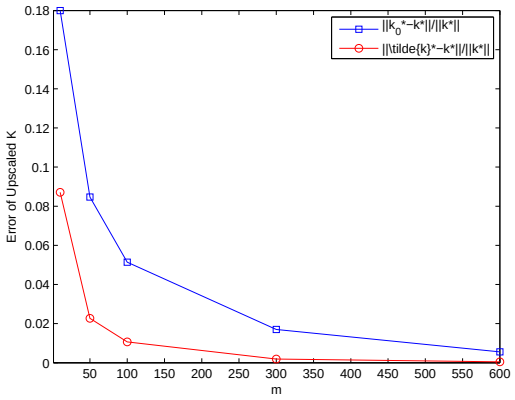

Fig. 5.5. Errors of $\frac{\|k^*-k_0^*\|}{\|k^*\|}$ and $\frac{\|k^*-\tilde{k}^*\|}{\|k^*\|}$ based on 100 realizations of log-exponential permeability fields, with the correlation lengths $l_x = 0.1$, $l_y = 0.1$ and the variance $\sigma = 2.0$.

We observe that the corrected upscaled permeability $\tilde{k}^*$ corrects the error in truncated upscaled permeability. For larger m, with $e(m) \geq 95\%$, the error is about 10^{-4}. For smaller m, with $e(m) \approx 50\%$, the error is about 5%. We will use the corrected scheme (5.15) and (5.16) to compute the corrected upscaled permeability $\tilde{k}^*$.

5.2.3. Error analysis

In this section, we estimate the error of the corrected upscaled permeability $\tilde{k}^*$. Writing the corrected solution $\tilde{\varphi}$ as $\tilde{\varphi} = \varphi_0 + \tilde{\varphi}'$, where φ_0 is the solution of (5.9), then φ' and $\tilde{\varphi}'$ satisfy the following equations respectively:

$$\begin{cases} \nabla \cdot (k\nabla\varphi') = -\nabla \cdot (k'\nabla\varphi_0) \\ \varphi' = 0 \end{cases} \tag{5.18}$$

$$\begin{cases} \nabla \cdot (k_0\nabla\tilde{\varphi}') = -\nabla \cdot (k'\nabla\varphi_0) \\ \tilde{\varphi}' = 0. \end{cases} \tag{5.19}$$

On one coarse grid block Ω, the error of corrected upscaled permeability is

$$\begin{aligned} |k^* - \tilde{k}^*| \quad &= |\langle k\nabla\varphi\rangle_\Omega - \langle k\nabla\tilde{\varphi}\rangle_\Omega| = |\langle k\nabla(\varphi' - \tilde{\varphi}')\rangle_\Omega| \\ &\leq |\Omega|^{\frac{1}{2}}\|k\nabla(\varphi' - \tilde{\varphi}')\|_{L^2}. \end{aligned} \tag{5.20}$$

Substracting (5.19) from (5.18), we obtain

$$\nabla \cdot (k\nabla(\varphi' - \tilde{\varphi}')) = -\nabla \cdot (k'\nabla\tilde{\varphi}'). \tag{5.21}$$

Multiplying the above equation by $\varphi' - \tilde{\varphi}'$ and intergrating by parts on Ω (using $\varphi' - \tilde{\varphi}' = 0$ on $\partial\Omega$), we obtain

$$\int_\Omega k\nabla(\varphi' - \tilde{\varphi}') \cdot \nabla(\varphi' - \tilde{\varphi}')dx = -\int_\Omega k'\nabla\tilde{\varphi}' \cdot \nabla(\varphi' - \tilde{\varphi}')dx. \tag{5.22}$$

Equivalently,

$$\int_\Omega \frac{1}{k}k\nabla(\varphi' - \tilde{\varphi}') \cdot k\nabla(\varphi' - \tilde{\varphi}')dx = -\int_\Omega \frac{1}{k}\frac{k'}{k_0}k_0\nabla\tilde{\varphi}' \cdot k\nabla(\varphi' - \tilde{\varphi}')dx. \tag{5.23}$$

Then we get

$$\begin{aligned} \frac{1}{k_{max}}\|k\nabla(\varphi' - \tilde{\varphi}')\|_{L^2}. \quad &\leq \frac{1}{k_{min}}|\frac{k'}{k_0}|_{max}\|k_0\nabla\tilde{\varphi}'\|_{L^2} \\ &\leq \frac{1}{k_{min}}|\frac{k'}{k_0}|_{max}(k_{0,max}|\frac{k'}{k_0}|_{max}\|\nabla\varphi_0\|_{L^2}). \end{aligned}$$

We substitute the above equation into (5.20), it follows that

$$|k^* - \tilde{k}^*| \leq |\Omega|^{\frac{1}{2}}|\frac{k'}{k_0}|^2_{max}\ k_{0,max}\frac{k_{max}}{k_{min}}\|\nabla\varphi_0\|_{L^2} \tag{5.24}$$

By KLE expansion, we have

$$|\frac{k'}{k_0}(x)|_{max} = |\exp(\sum_{i=m+1}^{N}\sqrt{\lambda_i}\Phi_i(x)\theta_i) - 1|_{max}. \tag{5.25}$$

Denote $V(x)$ as a vector with the product of square root of eigenvalues and eigenvec-

tors,

$$V(x) = (\sqrt{\lambda_1}\Phi_1(x), ..., \sqrt{\lambda_m}\Phi_m(x), ..., \sqrt{\lambda_N}\Phi_N(x)), \tag{5.26}$$

we can write $V(x)$ into two parts

$$V(x) = V_0(x) + V'(x), \tag{5.27}$$

where,

$$V_0(x) = (\sqrt{\lambda_1}\Phi_1(x), ..., \sqrt{\lambda_m}\Phi_m(x), 0, ..., 0),$$
$$V'(x) = (0, ..., 0, \sqrt{\lambda_{m+1}}\Phi_{m+1}(x), ..., \sqrt{\lambda_N}\Phi_N(x)).$$

For $\theta = (\theta_1, ..., \theta_m, ..., \theta_N)$, let $\theta = \theta_0 + \theta'$, where $\theta_0 = (\theta_1, ..., \theta_m, 0, ..., 0)$, $\theta' = (0, ..., 0, \theta_{m+1}, ...\theta_N)$, then we have

$$|\frac{k'}{k_0}| = |\exp(V' \cdot \theta') - 1|. \tag{5.28}$$

For $0 \leq m \leq N$, the energy ratio $e(m) = \frac{\sum_{i=1}^{m}\lambda_i}{\sum_{i=1}^{N}\lambda_i}$. Notice λ_i is decreasing, then $\lambda_j \leq \frac{(1-e(m))}{N-m}\sum_{i=1}^{N}\lambda_i$, $\forall j = m+1, ..., N$. $\sum_{i=1}^{N}\lambda_i = |\Omega|\sigma^2$, so $\lambda_j \leq \frac{(1-e(m))}{N-m}(|\Omega|\sigma^2)$, $\forall j = m+1, ..., N$. By Taylor expansion

$$\begin{aligned}
|\exp(V' \cdot \theta') - 1| &= |1 + (V' \cdot \theta') + \frac{(V' \cdot \theta')^2}{2!} + \frac{(V' \cdot \theta')^3}{3!} + ... - 1| \\
&= |(V' \cdot \theta') + O((V' \cdot \theta')^2)| \\
&\leq C\|V'\|_2\|\theta'\|_2 \\
&= \{\sum_{i=m+1}^{N}\lambda_i\phi_i^2(x)\}^{\frac{1}{2}}\ \|\theta'\|_2.
\end{aligned}$$

So we have

$$\begin{aligned}
|\frac{k'}{k_0}(x)|_{max} &= |\{\sum_{i=m+1}^{N}\lambda_i\phi_i^2(x)\}^{\frac{1}{2}}|_{max}\ \|\theta'\|_2 \\
&\leq \{\sum_{i=m+1}^{N}\lambda_i A_i^2\}^{\frac{1}{2}}\ \|\theta'\|_2 \\
&\leq \max_{m+1\leq i\leq N}\{A_i\}\{\sum_{i=m+1}^{M}\lambda_i\}^{\frac{1}{2}}\ \|\theta'\|_2 \\
&\leq A_m(1-e(m))^{\frac{1}{2}}|\Omega|^{\frac{1}{2}}\sigma\|\theta'\|_2 \\
&= |\Omega|^{\frac{1}{2}}\sigma A_m(1-e(m))^{\frac{1}{2}}\|\theta'\|_2.
\end{aligned}$$

Substituting the above result into (5.24), we have the following lemma.

Lemma 5.2.1. *Assume* $\frac{k_{\max}}{k_{\min}} \leq C$ *and* $k_{0,\max} \leq C_0$, C *and* C_0 *is independ of* θ, *then we get the following error estimation,*

$$|k^* - \tilde{k}^*| \leq C' A_m^2(1-e(m))\|\theta'\|_2^2\|\nabla\varphi_0\|_{L^2}, \tag{5.29}$$

where, $C' = |\Omega|^{\frac{3}{2}}\ \sigma^2\ C\ C_0$.

By Lemma 5.2.1, for each fixed θ_0, the error $|k^* - \tilde{k}^*|$ depends on $e(m)$ and the perturbation part of realization $\|\theta'\|_2$.

5.3. Fast Computation of $\tilde{k}^*$ on Hyperplane

In this section, we will discuss about the computation of the corrected upscaled permeability $\tilde{k}^*$ on a hyperplane. The hyperplane is defined based on a fixed realization θ_0. On a hyperplane, the Green's functions are same, so we can rapidly compute the upscaled permeability.

5.3.1. Green's function

Green's function is a type of function used to solve inhomogeneous differential equations subject to boundary conditions [17]. In the corrected single-phase flow system (5.16), Green's function $G(x, y)$ satisfies the following equation

$$div(k_0 \nabla G(x, y)) = \delta(x - y) \ . \tag{5.30}$$

In (5.16), the right hand side is

$$f(x) = -div(k' \nabla \phi_e^0) \ . \tag{5.31}$$

Then, the solution of (5.16) is:

$$\tilde{\phi}(x) = \int_\Omega G(x, y) f(y) dy \ , \tag{5.32}$$

where $G(x, y)$ and $f(x)$ satisfy (5.30) and (5.31), respectively.

Remark 5.3.1. *In the numerical discrete form, the equation* (5.30) *will be implemented as* $\mathbf{AU} = \mathbf{b}$*, so the solution is* $\mathbf{U} = \mathbf{A}^{-1}\mathbf{b}$*. In this discrete form, the Green's function is the inverse of the stiff matrix* $\mathbf{A}$*.*

5.3.2. Fast computation via hyperplane projection

Firstly, we introduce the definition of hyperplane. For any $\theta = (\theta_1, \theta_2, ..., \theta_m, \theta_{m+1}, ..., \theta_N) \in \mathbb{R}^N$, it can be written into two parts $\theta = \theta^0 + \theta'$, where $\theta^0 = (\theta_1, \theta_2, ..., \theta_m, 0, ..., 0)$ and $\theta' = (0, 0, ..., 0, \theta_{m+1}, ..., \theta_N)$. We define hyperplane $\mathbf{H}_{\theta^0}$ as the following,

$$\mathbf{H}_{\theta^0} := \{\omega \in \mathbb{R}^N | \omega = (\theta_1, \theta_2, ..., \theta_m, \omega_{m+1}, ..., \omega_N)\}, \tag{5.33}$$

where $\omega_i (m \leq i \leq N) \in \mathbb{R}$. $\mathbf{H}_{\theta^0}$ is shown in Figure 5.6.

On the hyperplane, Green's function $G(x, y)$ is uniquely determined by θ^0 (see

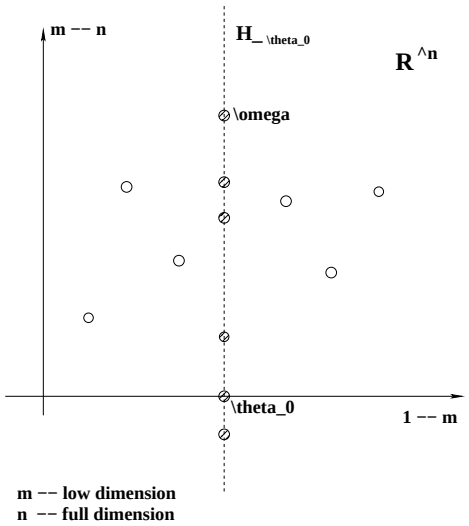

Fig. 5.6. Illustration of a hyperplane $\mathbf{H}_{\theta^0}$ in $\mathbb{R}^N$.

(5.30)) . And we observe that the source term $f(y)$ is determined by k' and ϕ_e^0. On the hyperplane $\mathbf{H}_{\theta^0}$ defined by θ^0, $G(x,y)$ and ϕ_e^0 are same for a relization $\theta \in \mathbf{H}_{\theta^0}$. For different realizations on this hyperplane, we only need to change θ' in the calculation of upscaled permeability. Green's function $G(x,y)$ and local solution ϕ_e^0 only need to be computed once, so we get the upscaled permeability rapidly on the whole hyperplane.

Now we compute the corrected upscaled permeability on one hyperplane. We consider an exponential permeability field k with correlation lengths $l_x = 0.3$, $l_y = 0.06$ and variance $\sigma = 2.0$. The fine grid is $N_x^f = N_y^f = 84$ and coarse grid is $N_x^c = N_y^c = 1$. Since the energy ratio $e(600) = 0.9760$, we take the solution for $m = 600$ as the reference solution. The result of the corrected upscaled permeability is shown in Table 5.2. In Table 5.2, we present errors between the truncated upscaled permeability k_0^* and k^* and the corrected upscaled permeability $\tilde{k}^*$ and k^*. As we mentioned earlier, the error of $\tilde{k}^*$ is smaller than error of k_0^*. We observe this here. We would like to point out that on a hyperplane , the computational costs for $\tilde{k}^*$ and k_0^* are same.

Another case we studied is an exponential permeability k with $l_x = 0.4$, $l_y = 0.05$, $\sigma = 2.0$. The fine grid is $N_x^f = N_y^f = 81$ and coarse grid as $N_x^c = N_y^c = 1$. We take the solution with $m = 400$ as the reference solution. Numerical results are shown in Table 5.3. In this table we present errors for the truncated upscaled permeability k_0^* and the corrected upscaled permeability $\tilde{k}^*$. The corrected upscaled permeability is more accurate.

Table 5.2. On a hyperplane, we compare the errors of $\frac{\|k^*-k_0^*\|}{\|k^*\|}$ and $\frac{\|k^*-\tilde{k}^*\|}{\|k^*\|}$ for an exponential permeability field, with the correlation lengths $l_x = 0.3$, $l_y = 0.06$ and the variance $\sigma = 2.0$.

m	$\frac{\|k_x^*-k_{x,0}^*\|}{\|k_x^*\|}$	$\frac{\|k_x^*-\tilde{k_x}^*\|}{\|k_x^*\|}$		$\frac{\|k_y^*-k_{y,0}^*\|}{\|k_y^*\|}$	$\frac{\|k_y^*-\tilde{k_y}^*\|}{\|k_y^*\|}$
3	0.101942	0.047174		0.350483	0.203149
5	0.097316	0.038822		0.301587	0.174062
10	0.073517	0.022492		0.244898	0.112901
15	0.070854	0.018579		0.193204	0.076596

Table 5.3. On one hyperplane, we compare the error of $\frac{\|k^*-k_0^*\|}{\|k^*\|}$ and $\frac{\|k^*-\tilde{k}^*\|}{\|k^*\|}$ for an exponential permeability field, with correlation lengths $l_x = 0.4$, $l_y = 0.05$ and the variance $\sigma = 2.0$.

m	$\frac{\|k_x^*-k_{x,0}^*\|}{\|k_x^*\|}$	$\frac{\|k_x^*-\tilde{k_x}^*\|}{\|k_x^*\|}$		$\frac{\|k_y^*-k_{y,0}^*\|}{\|k_y^*\|}$	$\frac{\|k_y^*-\tilde{k_y}^*\|}{\|k_y^*\|}$
3	0.079778	0.029701		0.384073	0.228551
5	0.076143	0.027384		0.336654	0.216180
10	0.060936	0.017679		0.271402	0.118205
15	0.053693	0.012607		0.216085	0.091798

5.4. Collocation Technique in Stochastic Space

In this section, we will introduce a collocation technique, which will be used to compute Green's function $G(x, y)$ and the source term $f(y)$. The collocation method has been used for the uncertainty problem [13] , where the author computes a set of upscaled permeabilities at reference nodes $\tilde{\theta}_i \in \mathbb{R}^N$. Each time for a new permeability k, the upscaled permeability k^* is interpolated by the reference upscaled permeabilities

$$k^*(x, \theta) = \sum_i k^*(x, \tilde{\theta}_i)\beta_i(\theta). \tag{5.34}$$

The weights $\beta_i(\theta)$ are computed priori and they depend on the interpolation method. Here in this dissertation, we propose a different approach. As in (5.32), the local solution can be computed by Green's function and the source term. We use collocation method for Green's function $G(x, y)$ and the local solution ϕ_e^0. Given collocation points $\{\theta_i\}_{i=1}^{M_c} \in \mathbb{R}^N$, for any $\theta_0 \in \mathbb{R}^N$, the interpolated Green function $\mathcal{I}(G)(x, y, \theta_0)$ and the truncated local solution $\mathcal{I}(\phi_e^0)(x, \theta_0)$ can be computed by

$$\mathcal{I}(G)(x, y, \theta_0) = \sum_{i=1}^{M_c} G(x, y, \theta^i)\alpha_i(\theta_0), \tag{5.35}$$

$$\mathcal{I}(\phi_e^0)(x, \theta_0) = \sum_{i=1}^{M_c} \phi_e^0(x, \theta^i)\beta_i(\theta_0). \tag{5.36}$$

Here, M_c is the total number of collocation points, α_i and β_i are computed priori.

Then, we use $\mathcal{I}(G)(x, y, \theta_0)$ and $\mathcal{I}(f)(y, \theta_0)$ to get the interpolated corrected solution:

$$\mathcal{I}(\tilde{\phi_e}) = \int_\Omega \mathcal{I}(G)(x, y, \theta_0)\mathcal{I}(f)(y)dy \tag{5.37}$$

At last, we can get the interpolated corrected upscaled permeability,

$$\mathcal{I}(\tilde{k^*})e = \frac{1}{|\Omega|}\int_\Omega k\nabla\mathcal{I}(\tilde{\phi}_e)dx. \tag{5.38}$$

The algorithm of of collocation method in $\mathbb{R}^N$ is given as following:

Algorithm 5.4.1. *For any* $\theta_0 = (\theta_1, \theta_2, ..., \theta_m, \theta_{m+1}, ..., \theta_{N-1}, \theta_N) \in \mathbb{R}^N$,

1. *Choose a set of collocation nodes* $\{\theta^i\}_{i=1}^{M_c} \in \mathbb{R}^N$. *Compute* $G(x, y, \theta^i)$, $\phi_e^0(x, \theta^i)$ *and interpolation weights* $\alpha_i(\theta^0)$, $\beta_i(\theta^0)$.
2. *Get the interpolated Green's function* $\mathcal{I}(G)(x, y, \theta^0)$ *and interpolated local solution* $\mathcal{I}(\phi_e^0)(y, \theta^0)$ *by* (5.35) *and* (5.36). *Then, compute the interpolated corrected solution by* (5.37).
3. *Compute the interpolated corrected upscaled permeability by* (5.38).

Remark 5.4.1. Step 1 *is a one-time computation. Since the collocation nodes* $\{\theta^i\}_{i=1}^{M_c} \in \mathbb{V}$ *are chosen, the interpolation values* $G(x, y, \theta^i)$ *and* $\phi_0(\theta^i)$ *are computed only once. For any* $\theta \in \mathbb{R}^N$, *we only need to do* Step 2 *and* Step 3.

In the following two sections, we will discuss the collocation method in different spaces, a lower dimensional space and the full dimensional space.

5.4.1. Collocation technique in lower dimensional space

In this section, we consider collocation method in a lower dimensional space $\mathbb{V}$. If the stochastic space is $\mathbb{R}^N$, then for $m \leq N$, we define the lower dimensional manifold $\mathbb{V}$ as follows

$$\mathbb{V} = \{\omega \in \mathbb{R}^N | \omega = (\omega_1, \omega_2, ..., \omega_m, 0, ..., 0)\} \subset \mathbb{R}^N \ . \tag{5.39}$$

Figure 5.7 illustrates the low dimensional manifold $\mathbb{V}$ in $\mathbb{R}^N$. For any $\theta \in \mathbb{R}^N$, let $\theta = \theta_0 + \theta'$ such that $\theta_0 = \{\theta_1, \theta_2, \cdots, \theta_m, 0, \cdots, 0\}$, $\theta' = \{0, 0, \cdots, 0, \theta_{m+1}, \cdots, \theta_N\}$. Then, $\theta_0 \in \mathbb{V}$.

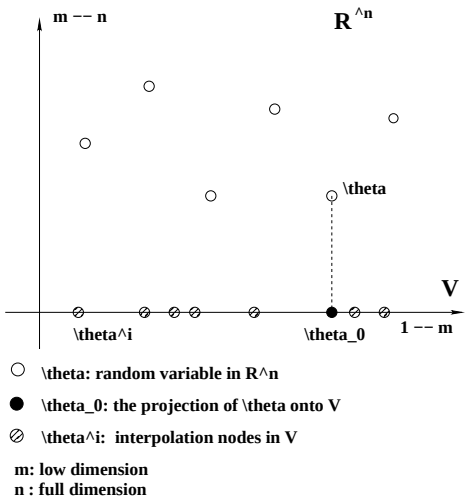

Fig. 5.7. An illustration of the projection from $\mathbb{R}^N$ onto $\mathbb{V}$.

5.4.1.1. General interpolation in $\mathbb{V}$

In a lower dimensional space, the general interpolation is commonly used. We briefly present some results in a unit cube. On a unit cube $[-1.0, 1.0]^2$, we consider a linear interpolation. Let mesh step size $h = \frac{1.0-(-1.0)}{M}$, and we choose the interpolation nodes as $\{\theta\} = \{(i_1h, i_2h, 0, 0, ..., 0)\}_{i1,i2=1}^{M}$. In each direction there are M interpolation nodes, so totally there are $M_c = M^2$ interpolation nodes. If $m = 3$, on $[-1.0, 1.0]^3$, the interpolation nodes are: $\{\theta\} = \{(i_1h, i_2h, i_3h, 0, ..., 0)\}_{i_1,i_2,i_3=1}^{M}$. So totally we need $M_c = M^3$ interpolation nodes. Similarly, on a m dimensional unit cube $[-1.0, 1.0]^m$, there will be M^m collocation nodes, $\{\theta\} = \{(i_1h, i_2h, , , , i_mh, 0, ..., 0)\}_{i_1,i_2,,,i_m=1}^{M}$.

We consider 20 realizations of log-normal permeability fields, with $l_x = 0.3$, $l_y = 0.5$, and $\sigma = 2.0$. We take mesh grid to be $N_x^f = N^f y = 17$, $N_x^c = N_y^c = 1$, and the total number of eigenvalues is $N = 187$. We compare the error of truncated upscaled permeability, corrected upscaled permeability and the interpolated corrected upscaled permeability. Numerical result is shown in Figure 5.8 and Table 5.4. In Figure 5.8, we plot the error of three types of upscaled permeability in 2-dimensional

and 3-dimensional space. The circle dash line is the error of $\frac{\|k_0^*-k^*\|}{\|k^*\|}$, the square dash line is the error of $\frac{\|\tilde{k}^*-k^*\|}{\|k^*\|}$, and the diamond dash line is the error $\frac{\|\mathcal{I}^m(\tilde{k}^*)-k^*\|}{\|k^*\|}$. By the plot, we can see the error of $\frac{\|k_0^*-k^*\|}{\|k^*\|}$ is much larger than the other two. The mean value of errors are shown in Table 5.4.

$m = 2, M_c = 11^2$ $\qquad$ $m = 3, M_c = 11^3$

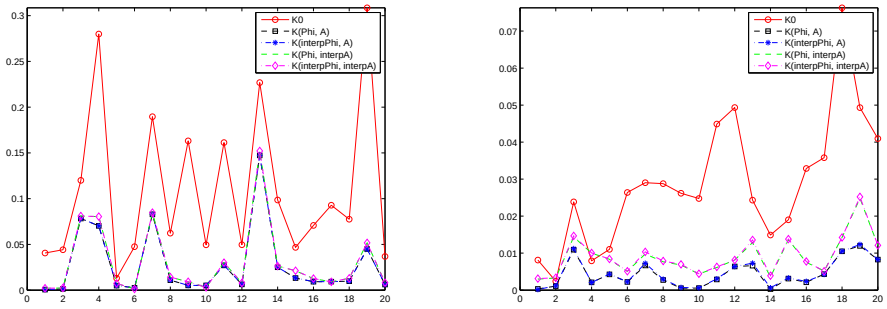

Fig. 5.8. Error of corrected upscaled permeability using linear interpolation for a normal permeability field with the correlation lengths $l_x = 0.3$, $l_y = 0.5$ and the variance $\sigma = 2.0$.

In Table 5.4, TE denotes the truncation error $\frac{\|k_0^*-k^*\|}{\|k^*\|}$, PE denotes the perturbation error $\frac{\|\tilde{k}^*-k^*\|}{\|k^*\|}(PE)$, and I^mE denotes the interpolation error where $\mathcal{I}^m$ is the interpolation in m-dimensional space. We observe that the error of $\frac{\|\mathcal{I}^m(\tilde{k}^*)-k^*\|}{\|k^*\|}$ is very close to the error of $\frac{\|\tilde{k}^*-k^*\|}{\|k^*\|}(PE)$. This means the interpolation error (I^mE) is very small. Thus the upscaled permeability $\mathcal{I}(\tilde{k}^*)$, which is from the interpolated Green's function $\mathcal{I}^m(G)$ and the interpolated solution $\mathcal{I}^m(\phi_e^0)$, is a very good approximation. We observe that the errors have the following relation,

$$PE \ll TE, \ PE + I^mE \ll TE. \tag{5.40}$$

Note that the interpolation error is small, so using perturbation approach with collocation technique, we can obtain an accurate upscaled permeability. But we notice that the choice the interpolation method is essential in this method. In practice,

Table 5.4. Error of $\frac{\|k_0^*-k^*\|}{\|k^*\|}$ (truncated upscaled permeability), $\frac{\|\tilde{k}^*-k^*\|}{\|k^*\|}(PE)$ (corrected upscaled permeability) and $\frac{\|\mathcal{I}^m(\tilde{k}^*)-k^*\|}{\|k^*\|}$ (interpolated corrected upscaled permeability using linear interpolation) for a log-normal permeability field with correlation lengths $l_x = 0.3$, $l_y = 0.5$ and covariance $\sigma = 2.0$.

Dimension	Interp Nodes	$\frac{\|k_0^*-k^*\|}{\|k^*\|}(TE)$	$\frac{\|\tilde{k}^*-k^*\|}{\|k^*\|}(PE)$	$\frac{\|\mathcal{I}^m(\tilde{k}^*)-k^*\|}{\|k^*\|}(PE+I^mE)$
$m=2$	$M_c = 11^2$	0.108946	0.028012	0.030891
$m=2$	$M_c = 21^2$	0.108946	0.028012	0.028568
$m=2$	$M_c = 31^2$	0.108946	0.028012	0.028345
$m=3$	$M_c = 11^3$	0.028805	0.004391	0.009220

the general interpolation methods only can be applied for low dimensional case, e.g. $m = 2, 3$. For example, if $m = 4$ and $M = 10$, then we have $M_c = 10^4$ values needed for the interpolation. This requires intense computing for the one-time computation of interpolation value. Furthermore, it requires many interpolation. We would like an interpolation method which can significantly reduce the computation. Sparse grid collocation methods will be used to alleviate this problem.

5.4.1.2. Sparse grid interpolation in $\mathbb{V}$

Now we discuss the sparse grid collocation method with Smolyak Algorithm in the lower dimensional space $\mathbb{V}$. In $\mathbb{V}$, using the 1st-level Smolyak Algorithm, we only need $2m + 1$ collocation nodes. Similar to Algorithm 5.4.1, we apply Smolyak algorithm and Lagrange interpolation introduced in [13, 28]. For m dimensional case, if we use the lowest interpolation level $N_l = 1$, then there are $M_c = 2m + 1$ reference nodes are needed for a linear interpolation. We try the same permeability field as the permeability in Table 5.4, the results with Smolyak algorithm are shown in Table 5.5.

Table 5.5. Error of $\frac{\|k_0^*-k^*\|}{\|k^*\|}$ (truncated upscaled permeability), $\frac{\|\tilde{k}^*-k^*\|}{\|k^*\|}(PE)$ (corrected upscaled permeability) and $\frac{\|\mathcal{I}^m(\tilde{k}^*)-k^*\|}{\|k^*\|}$ (interpolated corrected upscaled permeability using Smolyak Algorithm in $\mathbb{V}$) for a log-normal permeability field with correlation lengths $l_x = 0.3$, $l_y = 0.5$ and the variance $\sigma = 2.0$.

Dim	Interp Nodes	$\frac{\|k_0^*-k^*\|}{\|k^*\|}(TE)$	$\frac{\|\tilde{k}^*-k^*\|}{\|k^*\|}(PE)$	$\frac{\|I^m(\tilde{k}^*)-k^*\|}{\|k^*\|}(PE+I^mE)$
$m=2$	$M_c = 5(N_l = 1)$	0.108946	0.028012	0.067856
$m=2$	$M_c = 13(N_l = 2)$	0.108946	0.028012	0.034330
$m=2$	$M_c = 29(N_l = 3)$	0.108946	0.028012	0.029884

Comparing Table 5.4 and Table 5.5, we can see both the general interpolation and Smolyak algorithm give accurate results. But Smolyak interpolation uses much fewer nodes. If the interpolation level $N_l = 1$, only $2m+1$ reference nodes are needed. This interpolation is very efficient for a higher dimensional space, since $2m+1 \ll M^m$ (if m is large). We will discuss more of this sparse interpolation later.

5.4.2. Sparse grid interpolation in $\mathbb{R}^N$

In this section, we use Smolyak interpolation nodes in the full dimensional space $\mathbb{R}^N$. We notice that the first level Smolyak nodes has a very special distribution. For $m < N$, there are $2m + 1$ Smolyak nodes in $\mathbb{V}$ and $2N - 2m$ nodes in Hyperplane $\mathbb{H}_0 = (0, 0, ..., 0, \theta_{m+1}, ..., \theta_N)$, see Fig. 5.9.

In $\mathbb{V}$, we need solve $2m+1$ local problems to get the interpolated values $\{\mathcal{I}^N(G)(x, y, \theta^i)\}_{i=1}^{2m+1}$ and $\{\mathcal{I}^N(\phi_e^0)(x, \theta^i)\}_{i=1}^{2m+1}$. In $\mathbb{H}_0$ Green's function and local flow simulation only need to be computed once, so the $2N - 2m$ interpolation values can be rapidly computed by the method introduced in Section 5.3.2. By these two steps, we only solve $2m + 1$ local problems to get total $2N + 1$ interpolation values in $\mathbb{R}^N$.

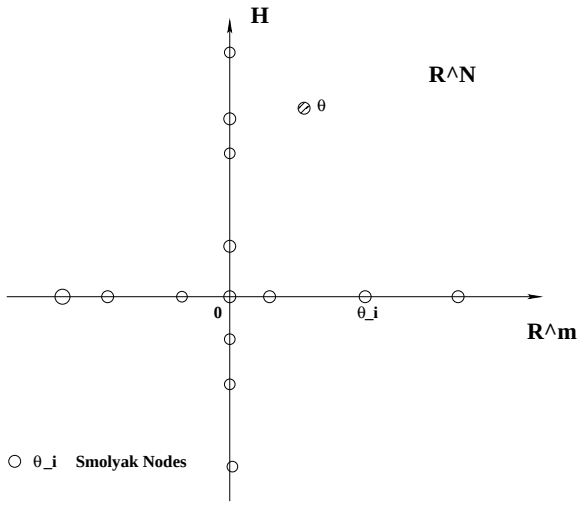

Fig. 5.9. Illustration of the first level Smolyak nodes in $\mathbb{R}^N$.

In Table 5.6, we show the results for a log-normal permeability field with correlation lengths $l_x = 0.1$, $l_y = 0.1$, and variance $\sigma = 2.0$. In Table 5.6, we compare the error of corrected upscaled permeability, interpolated upscaled permeablity $\mathcal{I}^m(\tilde{k}^*)$ in $\mathbb{V}$ and the interpolated $\mathcal{I}^N(\tilde{k}^*)$ in $\mathbb{R}^N$. We can see that using collocation technique, the error of upscaled permeability is significantly reduced. Comparing with $I^m E$ and $I^N E$, the error $I^N E$ (interpolation in R^N) is much smaller. That is because we apply the collocation in the full dimensional space $\mathbb{R}^N$. For the $2N+1$ interpolation nodes, $2N - 2m + 1$ are in one hyperplane, where we solve local flow problem once.

In Table 5.7, we show the results for a log-exponential permeability field with correlation lengths $l_x = 0.3$, $l_y = 0.5$, and variance $\sigma = 2.0$. Particularly, we compare the error of interpolated corrected upscaled permeablity $\mathcal{I}^m(\tilde{k}^*)$ in $\mathbb{V}$ and the error of interpolated corrected upscaled permeablity $\mathcal{I}^N(\tilde{k}^*)$ in $\mathbb{R}^N$. It shows us that $\mathcal{I}^N(\tilde{k}^*)$ is more accurate. We also notice these two interpolations have similar computation costs, i.e., $2m + 1$ local problems need to be computed.

Table 5.6. Error of $\frac{\|\tilde{k}^*-k^*\|}{\|k^*\|}(PE)$ (corrected upscaled permeability), $\frac{\|I^m(\tilde{k}^*)-k^*\|}{\|k^*\|}$ (interpolated corrected upscaled permeability using Smolyak Algorithm in $\mathbb{V}$), and $\frac{\|I^N(\tilde{k}^*)-k^*\|}{\|k^*\|}$ (interpolated corrected upscaled permeability using Smolyak Algorithm in $\mathbb{R}^N$) for a log-normal permeability field with $l_x = 0.1$, $l_y = 0.1$ and $\sigma = 2.0$.

Dim	$\frac{\|\tilde{k}^*_m-k^*\|}{\|k^*\|}(PE)$	$\frac{\|I^m(\tilde{k}^*)-k^*\|}{\|k^*\|}(PE+I^mE)$	$\frac{\|I^N(\tilde{k}^*)-k^*\|}{\|k^*\|}(PE+I^NE)$
$m=2$	0.22808043	0.04126556	0.00067630
$m=3$	0.19795747	0.04176262	0.00062872
$m=5$	0.15711911	0.04193267	0.00054790
$m=10$	0.08905113	0.04177832	0.00037403

5.5. Adaptive Clustering

In this section, we discuss an adaptive clustering technique with a particular type of interpolation method, piecewise constant interpolation. The main idea of the proposed adaptive clustering technique is to group the realizations into groups with similar properties. These properties are typically described by a particular norm.

5.5.1. Region partition in lower dimensional space

We introduce a partitioning technique and a projection to lower dimensions to compute the Green's function without using an expensive interpolation over the whole uncertainty space. First, we introduce the partitioning technique. Assume we have a partition

$$\mathbb{R}^N = \mathbb{W}_1 \cup \mathbb{W}_2 \cup \cdots \cup \mathbb{W}_{N_s}. \tag{5.41}$$

Table 5.7. Error of $\frac{\|I^m(\tilde{k}^*)-k^*\|}{\|k^*\|}$ (interpolated corrected upscaled permeability using Smolyak Algorithm in $\mathbb{V}$), and $\frac{\|I^N(\tilde{k}^*)-k^*\|}{\|k^*\|}$ (interpolated corrected upscaled permeability using Smolyak Algorithm in $\mathbb{R}^N$) for a log-exponential permeability field with $l_x = 0.3$, $l_y = 0.5$ and $\sigma = 2.0$.

Dim	$\frac{\|I^m(\tilde{k}^*)-k^*\|}{\|k^*\|}$	$\frac{\|I^N(\tilde{k}^*)-k^*\|}{\|k^*\|}$
$m = 2$	0.108425	0.022237
$m = 3$	0.090201	0.022351
$m = 5$	0.038620	0.020419
$m = 10$	0.014419	0.019867

For any $\theta \in \mathbb{R}^N$, we would like to find a region $\mathbb{W}_i$ that contains θ, i.e., $\theta \in \mathbb{W}_i$. Then, using the piecewise constant interpolation, we can obtain the Green's function and the truncated solution at a selected point θ

$$G(x,y,\theta) = \sum_{i=1}^{N_s} \delta_{\mathbb{W}_i}(\theta) G(x,y,\theta_i), \qquad \phi_e^0(y,\theta) = \sum_{i=1}^{N_s} \delta_{\mathbb{W}_i}(\theta)\phi_e^0(y,\theta_i), \tag{5.42}$$

where $\theta_i \in \mathbb{W}_i$, $\delta_{\mathbb{W}_i}(\theta) = \begin{cases} 1 & \theta \in \mathbb{W}_i \\ 0 & \theta \in \mathbb{R}^N/\mathbb{W}_i \end{cases}$, $1 \le i \le N_s$.

In (5.42), for $\theta \in \mathbb{W}_i$, we use the Green's function at θ_i to approximate the Green's function at θ. Similarly, we can approximate the Green's function for all the $\theta \in \mathbb{W}_i$. For example, the region's partition (5.41) can be a Voronoi decomposition. Each Voronoi cell $\mathbb{W}_i$ consists of all points closer to θ_i than to any other θ_j's for a given set of points $\{\theta_i\}_{i=1}^{N_s} \in \mathbb{R}^N$. In Figure 5.10, we show 2D clustering results. 100 independent realizations are clustered into 5 different clusters based on Euclidean distance. One can use different distance functions, e.g., based on flow measurements.

Figure 5.11 shows a clustering result on domain $\Omega = [-20, 20]^2$. We consider

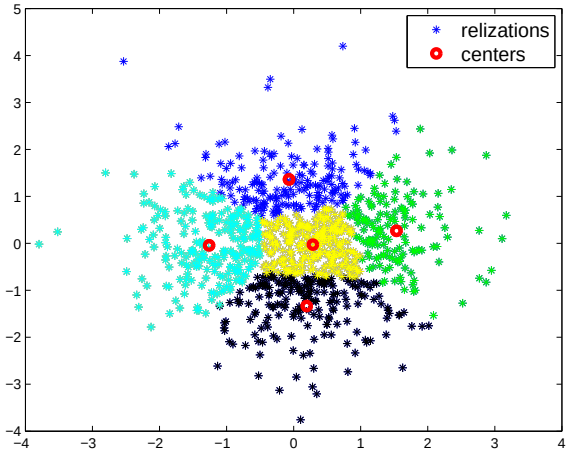

Fig. 5.10. Schematic showing the clustering for random realizations, the center of each cluster is the representative point.

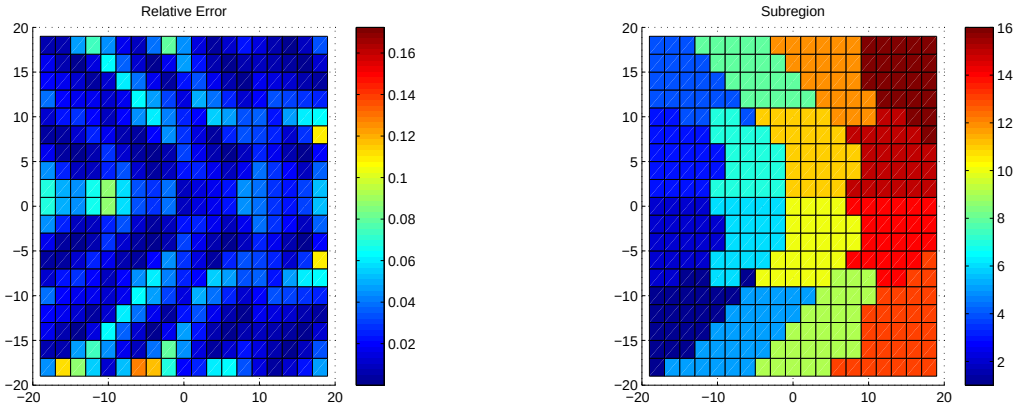

Fig. 5.11. Schematic illustration of the distribution of error $\frac{\|k^*-\tilde{k}^*\|}{\|k^*\|}$ on $\Omega = [-20, 20]^2$ and 16 clusters grouped by this error.

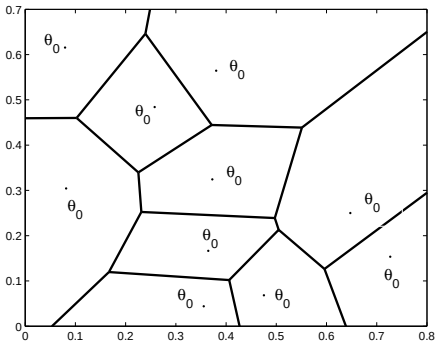

Fig. 5.12. Schematic showing the clusters and the representative points θ_0. In each cluster, the center point is chosen as the representative point.

400 realizations uniformly distributed in Ω. First, we group these realizations by Euclidean distance and get the centers of clusters. We call these centers as representative points since each of them represents a cluster. Then, for each realization we find the representative point that has the smallest error $\frac{\|k^*-\tilde{k}^*\|}{\|k^*\|}$. This way, the points are, in some sense, re-clustered based on flow measurements. The groups of realizations are shown in Figure 5.11 (right), where different colors are used for different clusters.

In this dissertation, we will use an error indicator based on inexpensive computations to cluster the selected realizations. The error indicator will be used to control the error in the cluster. In each cluster we would like the error of corrected upscaled permeability $\tilde{k}^*$ controlled within 5% accuracy. Moreover, we will show that the error indicator is inexpensive to compute and linearly proportional to real error.

5.5.2. Adaptive clustering with error indicator

Now, we will introduce the error indicator that will be used to group the realizations into clusters. In each cluster $\mathcal{C}$, assume the representative realization is θ_0 and the corresponding permeability is k_0, as in Figure 5.12.

First, we estimate the error of upscaled permeability $\tilde{k}^*$. For any realization $\theta \in \mathcal{C}$

with permeability k, we denote $k' = k - k0$ as the perturbation of the permeability. The corrected upscaled permeability is computed by (5.16) and (5.17). Here, we notice that this is a general correction scheme. Compared with the correction scheme in Section 5.2.2, we use the permeability at a representative point as k_0, see Figure 5.12. The error of $\frac{\|k^* - \tilde{k}\|}{\|k^*\|}$ is computed in a similar way as the error analysis in Section 5.2.3. We obtain the error indicator as follows.

$$EE = |\frac{k'}{k_0}|_{\max} \frac{k_{\max}}{k_{\min}} k_{0,max} \tag{5.43}$$

In $\Omega = [-20, 20]^2$, we consider a log-exponential permeability field with $l_x = 0.1$, $l_y = 0.1$, $\sigma = 2.0$. The fine grid is $N_x^f = N_y^f = 20$ and the coarse grid is $N_x^c = N_y^c = 2$. In Figure 5.13, we showed the distribution of $Log(Er)$ and $Log(EE)$. We observe that the true error and the error indicator have similar statistical distribution. Moreover, in Figure 5.14, we present the cross plot of $Log(Er)$ and $Log(EE)$. An approximate linear relation is observed. Next, we will choose some Er and EE to linearly interpolate the error at random realizations. Since the error indicator EE can be rapidly generated using the interpolation, we can get the interpolated error for all the realizations efficiently.

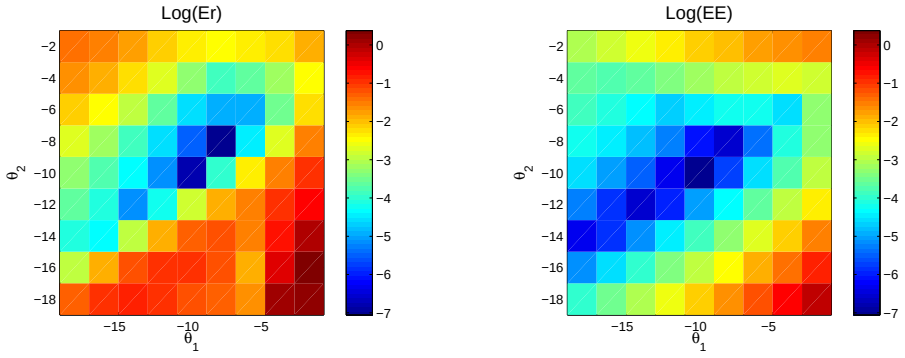

Fig. 5.13. Distribution of logarithm of the true error, $Log(Er)$ and logarithm of the error indicator, $Log(EE)$ for a log-exponential permeability field with $l_x = 0.1$, $l_y = 0.1$, $\sigma = 2.0$.

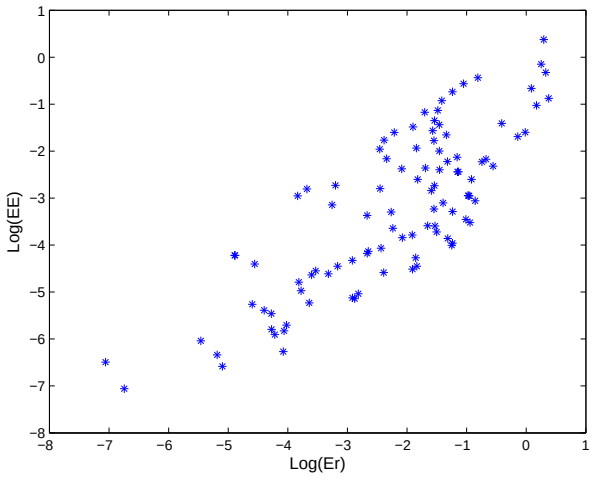

Fig. 5.14. Cross plot of natural logarithm of the true error, $Log(Er)$ and natural logarithm of the error indicator, $Log(EE)$ for a log-exponential permeability field with $l_x = 0.1$, $l_y = 0.1$, $\sigma = 2.0$.

Using 5.43, we cluster the realizations in a lower dimensional space. The algorithm is as follows.

Algorithm 5.5.1.

- *Step 1. For N_r realizations $\theta^{i}{}_{i=1}^{N_0} \in \mathbb{R}^m \subset \mathbb{R}^N$, we use Euclidean distance to cluster the N_r realizations into N_c clusters, denoted as $C_i, 1 \leq i \leq N_c$. In each C_i there are N_i realizations.*

- *Step 2. For $1 \leq i \leq N_c$, we choose some, e.g., five, realizations to compute the error indicator $\{EE_j\}_{j=1}^{5}$ and error $\{Er_j\}_{j=1}^{5}$.*

  - *For other realizations, $\{theta_j\}_{j=6}^{N_i} \in C_i$, we rapidly compute the error indicators $\{EE_j\}_{j=6}^{N_i}$.*

  - *Using $\{EE_j\}_{j=1}^{5}$,$\{Er_j\}_{j=1}^{5}$, and $\{EE_j\}_{j=6}^{N_i}$, we compute the interpolated error $\mathcal{I}Er_j$ at θ_j, for $6 \leq j \leq N_i$.*

  - *For $6 \leq j \leq N_i$, if $\mathcal{I}Er_j > 0.05$, we move θ_j into an auxiliary set C_a.*

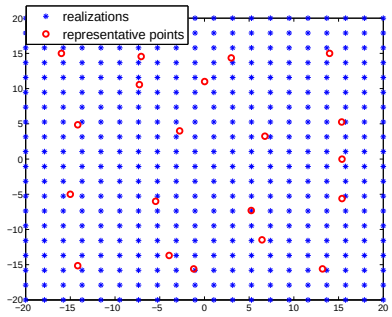

Fig. 5.15. 400 realizations and 20 representative points for a log-exponential permeability field with $l_x = 0.1$, $l_y = 0.1$, $\sigma = 2.0$.

- *Step 3. We repeat Step 1 and Step 2 for the auxiliary set C_a until C_a becomes an or nearly empty set (i.e., contains less than 5% of the total points). The auxiliary set is divided into N_a clusters.*

- *Step 4. Let $N_c = N_c + N_{c_a}$, then for any realization $\theta \in \mathbb{R}^m$, we find the closest representative point θ_i^0 using the (5.17) to rapidly compute the upscaled permeability. Here, the representative point, as discussed above, is the center of the cluster defined using Euclidean distance.*

5.5.3. Numerical results in lower dimensional space

In this section, we will show some numerical results of adaptive clustering in low dimensional space.

In $\Omega = [-20, 20]^2$, we consider a log-exponential permeability field with $l_x = 0.1$, $l_y = 0.1$, $\sigma = 2.0$. The fine grid is $N_x^f = N_y^f = 50$ and the coarse grid is $N_x^c = N_y^c = 5$. Using Algorithm 5.5.1, we use 400 realizations to generate 20 clusters as shown in Figure 5.15.

On Ω, we randomly select 100 realizations. For each realization, we find the closest representative point, i.e., find the cluster it belongs to. Then we can immediately

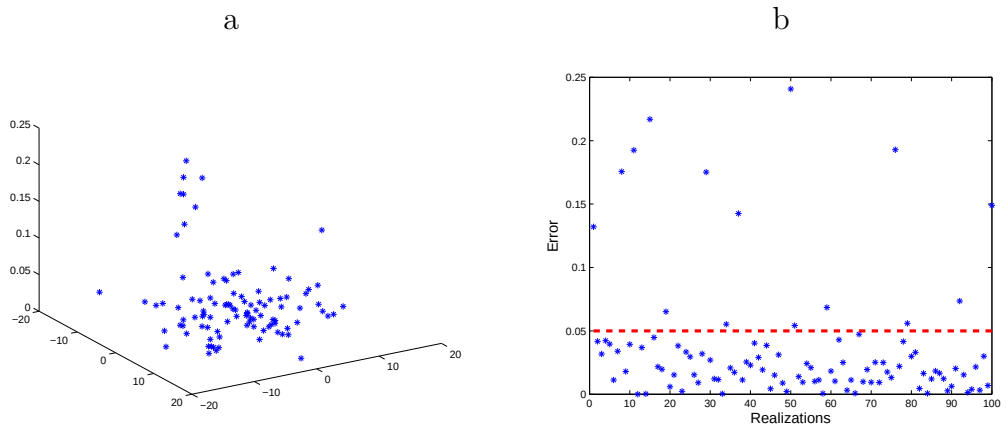

Fig. 5.16. Errors of $\frac{\tilde{k}^*-k^*}{k^*}$ based on 100 realizations for a log-exponential permeability field with $l_x = 0.1$, $l_y = 0.1$, $\sigma = 2.0$.

get the upscaled permeability. For these 100 realizations, we compare the corrected upscaled permeability (using the representative point) and the real upscaled permeability, see Figure 5.16. Figure 5.16 *a* shows the distribution of the errors. Note that most of the errors are small. In Figure 5.16 *b*, we plot the values of errors against realizations. The red line designates 0.05 error. We can see that for 85 realizations, the error $\frac{\tilde{k}^*-k^*}{k^*}$ is less than 5%.

5.6. Concluding Remarks

In this chapter, we studied ensemble-level upscaling.

- We proposed a correction scheme to compute the single-phase upscaled permeability for the ensemble of realizations. In the correction scheme, the solution of a local flow problem is represented by a product of Green's function and a source term. This allows us to get the local solution rapidly on hyper-planes.

- To avoid solving local flow problem for all realizations, we use collocation techniques in a lower dimensional space $\mathbb{V}$ and full dimensional space $\mathbb{R}^N$. The first

order Smolyak sparse grid is used in a collocation method. Green's function and local flow solution is calculated at the Smolyak nodes. Using these values, we can rapidly interpolate Green's function and local solution at any random realization.

- Another approach for rapid calculation of upscaled permeability is to use adaptive clustering techniques. We propose an error indicator to adaptively group the realizations into a number of clusters, then solve local flow problem on each reduced set. In each cluster, we choose only one representative realization and compute Green's function at this point. For other realizations in this cluster, we use Green's function at the representative point and the correction scheme to get the approximated upscaled permeabilities.

- The adaptive clustering can also be applied in higher dimensional space. This is still under investigation.

CHAPTER VI

SUMMARY

In the dissertation, we have studied efficient upscaling methods for flow and transport in heterogeneous porous media. Our studies focus on realization-based two-phase flow and transport upscaling as well as ensemble-level flow upscaling in the dissertation.

In two-phase flow and transport upscaling, we proposed TOF-based upscaling techniques and local-global two-phase upscaling techniques. The common feature of these methods is that both of these techniques use some type of limited global information. TOF-based methods aim to capture the spatial variations of the solution of transport equations that have hyperbolic nature and difficult to upscale. These methods use the solutions of time-of-flight equation and use this information to represent the local heterogeneities in the solution. Local-global two-phase upscaling techniques attempt to approximate the non-local behavior of the solution due to time. In particular, one of the difficulties in the upscaling of hyperbolic equation is to represent the time variation of the solution. These two methods capture global flow effects both spatially and temporally and correct a bias in existing two-phase upscaling methods. We have studied these methods for permeability fields with different correlation lengths, different mobility ratios, different flow conditions and multiple realizations. The numerical results showed that the proposed methods consistently improve the existing two-phase upscaling methods and provide accurate coarse-scale solutions for both flow and transport. We also proposed discontinuous Galerkin methods for the transport equation using multiple limited global information. Some analysis for time-dependent flow equations based on homogenization is presented.

In the dissertation, we studied an efficient approach for ensemble-level flow upscaling. The objective is to rapidly upscale a large ensemble of permeability fields. We use perturbation techniques as well as collocation methods for this purpose. A perturbation approach is proposed and the error of the corrected upscaled permeability is analyzed. Combining the perturbation approach with sparse grid collocation techniques and adaptive clustering techniques allows us to compute the upscaled permeability rapidly for all realizations in stochastic space. We found that the interpolation error in the sparse grid collocation is small and independent of the dimension of the uncertainty space. Using sparse grid collocation techniques with a perturbation approach gives an accurate upscaled permeability. Collocation technique can also be applied in conjunction with finite element methods. For multiple realizations, we can use a collocation technique to get basis functions for a random realization. The adaptive clustering technique has been studied in the dissertation. The main idea is to cluster permeability realizations such that one can use a few representative realizations per cluster and compute the upscaled permeabilities rapidly. We present some numerical examples to demonstrate the efficiency of the proposed adaptive clustering techniques.

REFERENCES

[1] J. W. Barker, and P. Dupouy, *An analysis of dynamic pseudo-relative permeability methods for oil-water flows*, Petroleum Geoscience, 5 (1999), pp. 385–394.

[2] V. Barthelmann, E. Novak, and K. Ritter, *High dimensional polynomial interpolation on sparse grid*, Advances in Computational Mathematics, 12 (2000), pp. 273–288.

[3] Y. Chen, *Upscaling and subgrid modeling of flow and transport in heterogeneous reservoirs*, Ph.D. thesis, Stanford University, California, 2005.

[4] Y. Chen, and L. J. Durlofsky, *Adaptive local-global upscaling for general flow scenarios in heterogeneous formations*, Transport in Porous Media, 62 (2006), pp. 157–185.

[5] Y. Chen, and L. J. Durlofsky, *Efficient incorporation of global effects in upscaled models of two-phase flow and transport in heterogeneous formations*, Multiscale Modeling and Simulation, 5 (2006), pp. 445–475.

[6] Y. Chen, L. J. Durlofsky, M. Gerristen, and X. H. Wen, *A coupled local-global upscaling approach for simulationg flow in highly heterogeneous formations*, Advances in Water Resources, 26 (2003), pp. 1041–1060.

[7] Y. Chen, and L. J. Durlofsky, *Ensemble-level upscaling for efficient estimation of fine-scale production statistics*, SPE Journal, 13 (2008), pp. 400–411.

[8] Y.Chen, and Y. Li, *Local-global two-phase upscaling of flow and transport in heterogeneous formations*, Multiscale Modeling and Simulation, accepted, 2009.

[9] M. A. Christie, *Flow in porous media–scale up of multiphase flow*, Current Opinion in Colloid & Interface Science, 6 (2001), pp. 236–241.

[10] B. Cockburn, and C. Shu, *Runge-Kutta discontinuous Galerkin methods for convection-dominated problems*, Journal of Scientific Computing, 16 (2001), pp. 173–261.

[11] C. V. Deutsch, and A. G. Journel, *GSLIB: Geostatistical Software Library and User's Guide, 2nd edition*, Oxford University Press, New York, 1998.

[12] A. Datta-Gupta, and M.J. King, *Streamline Simulation: Theory and Practice*, Society of Petroleum Engineers, Richardson, Texas, 2007.

[13] P. Dostert, *Uncertainty quantification using multiscale methods for porous media flows*, Ph.D. dissertation, Texas A&M University, College Station, TX, 2007.

[14] L. J. Durlofsky, *Numerical calculation of equivalent grid block permeability tensors for heterogeneous porous media*, Water Resources Research, 27 (1991), pp. 699–708.

[15] Y. R. Efendiev, and L. J. Durlofsky, *A generalized convection-diffusion model for subgrid transport in porous media*, Multiscale Modeling and Simulation, 1 (2003), pp. 504–526.

[16] Y. Efendiev, V. Ginting, T. Hou, and R. Ewing, *Accurate multiscale finite element methods for two-phase flow simulations*, Journal of Computational Physics, 220 (2006), pp. 155–174.

[17] L. C. Evans, *Partial Differential Equations*, American Mathematical Society, Providence, Rhode Island, 1998.

[18] C. L. Farmer, *Upscaling: a review*, International Journal for Numerical Methods in Fluids, 40 (2002), pp. 63–78.

[19] M. G. Gerritsen, and L. J. Durlofsky, *Modeling fluid flow in oil reservoirs*, Annual Review of Fluid Mechanics, 37 (2005), pp. 211–238.

[20] R. E. Greene, and S. G. Krantz, *Function Theory of One Complex Variable*, John Wiley and Sons, New York, 1997.

[21] T. A. Hewett, K. Suzuki, and M. A. Christie, *Analytical calculation of coarse-grid corrections for use in pseudofunctions*, SPE Journal, 3 (1998), pp. 293–305.

[22] T. A. Hewett, and T. Yamada, *Theory for the semi-analytical calculation of oil recovery and effective relative permeabilities using streamtubes*, Advances in Water Resources, 20 (1997), pp. 279–292.

[23] T. Y. Hou, and X. H. Wu, *A multiscale finite element method for elliptic problems in composite materials and porous media*, Journal of Computational Physics, 134 (1997), pp. 169-189.

[24] L. Holden, and B.F. Nielsen, *Global upscaling of permeability in heterogeneous reservoirs: the output least squares (OSL) method*, Transport in Porous Media, 40 (2000), pp. 115–143.

[25] Y. Li, Y. Chen, and Y. Efendiev, *Efficient incorporation of time-dependent global effects in two-phase upscaling of flow and transport in heterogeneous formations*, in Proceedings of the 2009 International Association for Mathematical Geosciences (IAMG) Annual Conference, Standford, CA, 2009.

[26] Y. Li, Y. Efendiev, R. E. Ewing, G. Qin, and X. H. Wu, *An accurate multiphase upscaling for flow and transport in heterogeneous porous media*, in Proceedings of the 15th Middle East Oil&Gas Show and Conference, Bahrain, 2007, paper SPE105377-PP.

[27] M. Loève, *Probability Theory*, 4th Edition, Springer, Berlin, 1977.

[28] F. Nobile, R. Tempone, and C.G. Webster, *A sparse grid stochastic collocation method for partial differential equations with random input data*, SIAM Journal on Numerical Analysis, 46 (2008), pp. 2309–2345.

[29] D. W. Pollock, *Semianalytical computation of pathlines for finite-difference models*, Groundwater, 26 (1998), pp. 743–750.

[30] M. H. Protter, and H. F. Weinberger, *Maximum Principles in Differential Equations*, Springer-Verlag, Inc., New York, 1984.

[31] K. Suzuki, and T. A. Hewett, *Sequential upscaling method*, Transport in Porous Media, 46 (2002), pp. 179–212.

[32] Ph. Renard, G. de Marsily, *Calculating effective permeability: a review*, Advances in Water Resources, 20 (1997), pp. 253–278.

[33] T. C. Wallstrom, M. A. Christie, L. J. Durlofsky, and D. H. Sharp, *Effective flux boundary conditions for upscaling porous media equations*, Transport in Porous Media, 46 (2002), pp. 139–153.

[34] T. C. Wallstrom, S. Hou, M. A. Christie, L. J. Durlofsky, D. H. Sharp, and Q. Zou, *Application of effective flux boundary conditions to two-phase upscaling in porous meida*, Transport in Porous Media, 46 (2002), pp. 158–178.

[35] X.H. Wu, Y. Efendiev, and T. Hou, *Analysis of upscaling absolute permeability*, Discrete and Continuous Dynamical Systems - Series B, 2 (2002), pp. 185–204

[36] E. Wong, *Stochastic Process in Information and Dynamic Systems*, McGraw-Hill, New York, 1971.

[37] X.-H. Wu, R. R. Parashkevov, M. T. Stone, and S. L. Lyons, *Global scale-up on reservoir models with piecewise constant permeability field*, Journal of Algorithms & Computational Technology, 2 (2008), pp. 223–247.

[38] P. Zhang, G. E. Pickup, and M. A. Chrisite, *A new practical method for upscaling in highly heterogeneous reservoir models*, SPE Journal, (2008), pp. 68–76.

APPENDIX A

SMOLYAK ALGORITHM

In this part, we introduce a sparse grid collocation method, Smolyak algorithm. Since $\theta \in \mathbb{R}^N$, if N is large, the computational cost of interpolation in $\mathbb{R}^N$ will be extremely high. Instead of using full grids, we use sparse grids in high dimensional space. By [2, 28], we use the Smolyak with the extrema of the Chebyshev polynomials.

The Smolyak formula $A(q, N)$ is a linear combination of product formulas such that an interpolation property for $N = 1$ is preserved for $N > 1$. Let $|\mathbf{i}| = i_1 + \cdots + i_N$ for $\mathbf{i} \in \mathbb{N}^N$, then the smolyak algorithm is given by [2, 13]

$$A(q,N) = \sum_{q-n+1 \le |\mathbf{i}| \le q} (-1)^{q-|\mathbf{i}|} \cdot \begin{pmatrix} N-1 \\ q-|\mathbf{i}| \end{pmatrix} \cdot U^{i_1} \otimes \cdots \otimes U^{i_N}. \tag{A.1}$$

To compute $A(q, N)(f)$, one only needs to know function values at the sparse grid:

$$H(q,N) = \bigcup_{q-N+1 \le |\mathbf{i}| \le q} (-1)^{q-|\mathbf{i}|} (\Theta^{i_1} \times \cdots \times \Theta^{i_N}). \tag{A.2}$$

where $\Theta^i = \{\theta_1^i, \cdots \theta_{M_i}^i\} \subset [-1, 1]$ denotes the set of points used by U^i. This leads us to $(k + N, N) \approx \frac{2^k}{k!} \cdot N^k$ nodes used by $A(q, N)$. Here k determines how many nodes will be used. For a fixed N, we define $A(N+k, N)$ as k^{th} order Smolyak interpolation. The smallest order is $k = 1$, in which case we only have $2N + 1$ interpolation nodes.

Here, we consider Smolyak formulas that are based on the exterma of Chebyshev polynomials. We choose

$$\theta_j^i = -\cos \frac{\pi \cdot (j-1)}{M_i - 1}, \qquad j = 1, \cdots, M_i. \tag{A.3}$$

and define $\theta_i = 0$ for $M_i = 1$. We also choose $M_1 = 1$ and $M_i = 2^{i-1} + 1$ for $i > 1$. This has the benefit of making our nodal sets nested, thus $H(q, N) \subset H(q + 1, N)$.

By [2], we have that $A(N+k, N)$ is exact for all polynomials of degree k.

VITA

Yan Li was born in Yishui, Shandong Province, China. She received her Bachelor of Science and Master of Science, respectively, in mathematics from Shandong University in June 2000 and June 2003. Then she began studies at Texas A&M University where she received her Ph.D. from the Department of Mathematics in December 2009. Yan Li can be contacted by writing to: Institute for Mathematics and Its Applications, University of Minnesota, 114 Lind Hall, 207 Church St., Minneapolis, MN, 55455-0134 or to the email address sdyanli@gmail.com.